國立臺灣師範大學理學院地球科學系

碩士論文

Department of Earth Sciences

National Taiwan Normal University

Master's Thesis

應力場變化對於三維裂隙系統演化的影響：以台灣東北部為例

Influences of stress variation on the evolution of 3D fracture system: An example in NE Taiwan

Pham Thi Huong

指導教授：葉恩肇 博士

Advisor: En-Chao Yeh, Ph.D.

中華民國 109 年 9 月

September 2020

ACKNOWLEDGEMENTS

First of all, I would like to express my thank to my patient and supportive supervisor, Prof. En-Chao Yeh. Prof. En-Chao continuously provided encouragement and was always willing and enthusiastic to assist in any way he could throughout my research project. I am extremely grateful for our friendly chats and your support in my academic and my daily life in Taiwan.

I am incredibly grateful for following people at Structural Geomechanics Laboratory of Dept. Earth Sciences of National Taiwan Normal University, without whom I would not have been able to complete this research. Special thanks for the helpful contribution from my friendly lab-mate Ping-Chuan Chen, Shin-Kuan Yang, Guan-Hao Chen, Sing-Jhih Liu, Wei-Lun Tsai, and Yung-An Liao and valuable suggestion from lab assistants Yung-Tien Chiu and Xiao-Jun Peng.

My sincere thanks also go to all Professors and staff of the Department of Earth Sciences of National Taiwan Normal University. My completion of this project could not have been accomplished without their support. I would also like to extend my special thanks to Dr. Chih-Hsiang Yeh and my friend Kelly from National Chiao Tung University for their useful guidance in my methodology to carry out my research.

Finally, I would like to express deep and sincere gratitude to my parents for their love, caring, and sacrifices for educating and preparing me for my future. I am very thankful to all my Vietnamese and Taiwanese classmates for their love, understanding, and support.

ABSTRACT

When nucleation of fractures and reactivation of pre-existing fractures was supposedly triggered by earthquake events, the stress state characterized by the focal mechanism of earthquake events can manipulate the 3D fracture patterns. That 3D fracture pattern might present the distribution, density variation, and connectivity of the fracture system in spatial always received special attention from geologists for the considerations regarding the mining and exploration development, disaster forecasting, and even the evolution of mountain building processes.

Northeast Taiwan provided a special opportunity to understand the evolution of stress state from compressive subduction at the south to back-arc extension at north in the northeastern part of this active orogenic belt. The stress state in cross-section generated by inverted the focal mechanism data, which was collected from 1991 to 2016. The certain stress regime of Northeast Taiwan primarily changes from reverse faulting at the south to strike-slip faulting at the north, which approximately conducts the transformation of the orientation of the nucleated fractures network system. Even the presence of different in-situ stress regimes can cause reactivation of pre-existing in later. This region basically provides to the important situation to evaluate the evolution of fracture patterns with the stress field, contemporaneously. Therefore, our study aims to seeking, identifying, investigating the geometric characteristics of fracture planes of NE Taiwan by analyzing Digital Elevation Models (DEM). From DEM, the recent development of GIS and remote sensing technology can support to access and collect data of the fracture system in the inaccessible region.

Our results show that in three domains, we recognized 187 surface fractures by applied the cross-cutting relationship between foliation and fracture planes and also calculated the fracture attitudes. In general, the spatial distribution of mean striking of fracture plane changed from N-S in the Domain III via NE-SW in the Domain II to ENE-WSW orientation in the Domain I. However, to get better results, only 120 fractures planes with $R^2 \geq 0.85$ and length $\geq$ 1000 meters are compatible to predicted fractures generated from focal mechanism analysis. After evaluating the fracture instabilities, we realized that nucleated surface fractures in DEM could be correlated with the applied stress field in the evolution of the tectonic setting from the south to the north along the coastline area at NE Taiwan. The number of nucleated surface fractures of Domain I is highest (64%) in comparison with other domains. Additionally, we examine the slip tendency analysis to measure the reactivation of nucleated surface fracture. The results confirmed the important roles of the extensional force of back-arc Okinawa Trough opening to the reactivated fracture in NE Taiwan. The examination result of slip tendency presented 54% nucleated fracture planes of Domain I could be reactivated under the stress state. Therefore, mapping and classifying fracture planes provided valuable information to the 3D fracture map, which should be able to further implication in terms of the landslide, groundwater, and scientific research issues.

Keywords: Fractures Instability Analysis, 3D Fracture Mapping, Stress Inversion Analysis.

CONTENT

LIST OF TABLES

LIST OF ABBREVIATIONS

CeR	Central Range
DEM	Digital Elevation Model
EP	Eurasian Plate
GPS	Global Positioning System
LVF	Longitudinal Valley Fault
LZV	Luzon Volcanic Arc
NE	Northeast
NF	Normal Fault
PSP	Philippine Sea Plate
RF	Reverse Fault
RRIM	Red Relief Image Model
SS	Strike-slip Fault

LIST OF FIGURES

CHAPTER 1: INTRODUCTION

1.1 Motivation

1.1.1 Tectonics of NE Taiwan

Stress state derived from the focal mechanism of earthquake events might govern the attitude distribution of surface fractures. The focal mechanism solution was on analyzed the first motion of seismic faults in the slip plane (Morris et al., 1996). Each fault type is developed in a distinctive stress state. For example, the reverse fault is commonly correlated with the compressional stress regime, whereas the normal fault is primarily indicated the extensional stress regime. The evolution of the stress state highly manipulated in the connection and distribution of fracture system, even might be useful to identify the fracture generation. Therefore, the stress field played important roles in constructing the formation of nucleated surface fracture and sparking the reactivation process of fractures.

We realized that Taiwan orogen provides us an unique opportunity to study the evolution of structural characteristics at the transition area between of Philippine Sea Plate (PSP) and Eurasian Plate (EP). NW-SE collision at east Taiwan and N-S subduction at NE Taiwan between two plates implied the change of different environments from the collision, post-collision collapse at east Taiwan, and subduction to back-arc extension at NE Taiwan (Teng, 1990; Shyu et al., 2005). In eastern Taiwan, PSP collides with EP since about 5 Ma (Ho, 1986; Teng, 1990). Conversely, the topography dramatically dropped from Hualien to Ilan Plain might present the collapse of NE Taiwan orogen due to PSP subduct beneath EP in the NE Taiwan (Teng, 1996) and the back-arc opening of southern Okinawa Trough examined by Sibuet et al. (1987)

and Nishimura et al. (2004). Thus, northeastern Taiwan has been highly involved with different stages of the tectonic evolution of Taiwan orogen. Numerous previous studies (e.g., Angelier et al., 1990; Clift et al., 2008; Wu et al., 2009; Kang et al., 2015) already discussed the tectonic evolution from the northern segment of Longitudinal Valley Fault (LVF) to the northernmost of Taiwan island. Based on their analyses, the local crustal deformation of Taiwan might be experienced through: (1) The ongoing oblique collision of NE-SW trending Chinese continental margin of EP with the mostly N-S trending Luzon Volcanic Arc (LVA) of PSP since 5 Ma (Ho, 1986; Teng, 1990; Shyu et al., 2005) formed the NE-trending Taiwan orogen. (2) Offshore of NE Taiwan has been influenced by the Ryukyu subduction system where the EP overrides the PSP along the Ryukyu Trench with the rate approximately 40 mm/yr in NE orientation (Lallemand and Liu, 1998; Nakamura, 2004) and (3) The back-arc opening in N170°-180°E direction with the rates of 50 mm/yr developed by the active rifting of the Okinawa Trough behind the Ryukyu arc (Nishimura et al., 2004; Sibuet et al., 1987) (Fig 1.1A).

The consequences of the arc-continental collision, subduction, and rifting have been suggested to lead the first-order crustal deformation pattern in NE Taiwan. Besides that, Lai et al. (2009) documented some earthquake events with the moderate-sizes (e.g., 2005 M_w 5.4, 2015 M_w 5.7, and 2016 M_w 5.6 events) at the Ilan plain. They are basically consistent with the strike-slip faulting motion (Lai et al., 2009). And the M = 7.3 earthquake event happened on the Milun Fault at the part of northern LVF segments, with two following M 7.0 earthquake sequences occurred in other segments of LVF (Chen et al., 2008). They have been questioned whether the manipulation of the focal mechanism from earthquake events motivated and modified the deformation patterns at

NE Taiwan, and, whether the combination of tectonic setting and earthquake events can generate the existence of a fracture pattern at NE Taiwan.

Previous seismic investigations practically indicated the transitional pattern of a stress state and seismicity in NE Taiwan (Lin et al., 2004; Wu et al., 2007; Wu et al., 2008; Chou &Chen, 2012 and Huang et al., 2012). In particular, Wu et al. (2008) illustrated that in the northeastern seismic zone, the intermediate-depth earthquakes are associated with the PSP-EP subduction system, whereas shallow events follow the opening of the Okinawa Trough and collision between EP and LVA. In Figure 1.1B, based on the results of relocated hypocenters and focal mechanism first motion, Huang et al. (2012) presented the evolution of stress state in NE Taiwan. In the northern part, normal faulting focal mechanisms (blue balls) are dominant, while 2 clusters of mostly left-lateral strike-slip focal mechanisms (light green balls) are discovered in the transition area (southern Ilan Plain and Nanao area). In the southern part, reverse faulting focal mechanisms are predominantly presented at the Hualien domain with 2 NNE-SSW trending clusters (red balls). Therefore, we supposed that the evolution of the in-situ stress pattern could govern and construct the surface fractures pattern in NE Taiwan by different stages.

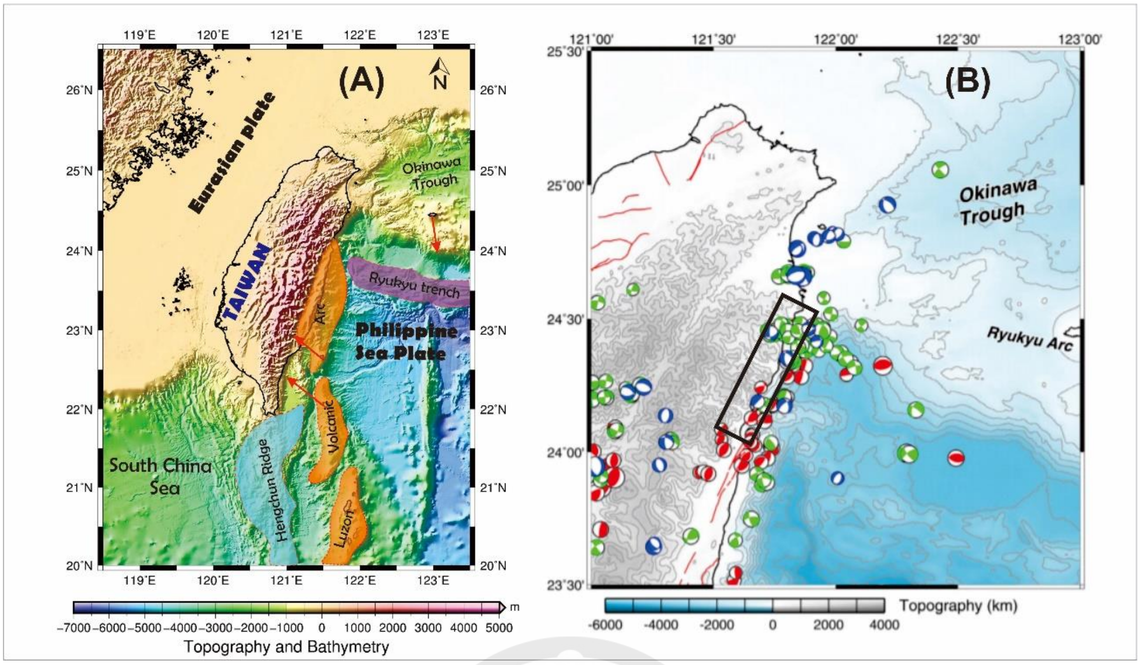

Figure 1.1: (A) Tectonic map of Taiwan showing tectonic units. (B) Distribution of focal mechanisms (169 EQ events, M>4). (A) Hengchung ridge in blue, Luzon volcanic arc in light orange, Ryukyu trench is in the light purple area. The red arrow indicated the predicted plate motion vector from NUVEL-1. (B) The kinematic model of the tectonic evolution in NE Taiwan was proposed by Huang et al., (2012) based on the distribution of focal mechanism. The study is located inside the black rectangle.

1.1.2 The model of fracture development at coastline area in NE Taiwan

The stress state is an important controlling factor for the instability behavior of fractures (Sauber & Molnia, 2004; Sutinen et al., 2009 and Vavrycuk et al., 2015). The slip vector of fractures might correspond with the distribution of the stress state, such as paleo-stress analysis comes from fault-slip data (Bott, 1959; Delaney et al., 1986). The structural characterization, network system, and assessment of the faults and fractures are the keys to analyzes and demonstrate in-situ stress. According to the evolution of the tectonic setting from south to north along the coastline area at NE Taiwan described in Section 1.1.1, we divided in coastline area into three different Domains I, II & III, respectively (Fig 1.2). In this figure, we proposed the simulated fractures evolution model of the coastline area. In the early stage, the whole coastline area supposedly experienced the compressional environment; hence it produced the fault and fracture slipped in the applied reverse faulting regime (red area in Fig 1.2A). The result of the flipping of subduction polarity between PSP and EP at the secondary stage, which is led the post-orogenic collapse from Hualien to Ilan Plain, has been conducted the presence of strike-slip faulting in the Domain I and II (Fig 1.2B). In the late stage, the opening of southwestern Okinawa Trough since 2 Ma years ago become an important driving force in NE Taiwan. At that time, it dedicated the normal faulting regime in northern Taiwan and promoted the construction of fracture patterns in Domain I (Fig 1.2C). However, pre-existing fractures generated by the paleo-stress state still under considering the reactivation by the current stress state. Therefore, the estimation stress state based on the fracture investigation is crucial. Thus, this study aims to mapping the fracture pattern in different domains and examining it with a regional stress state.

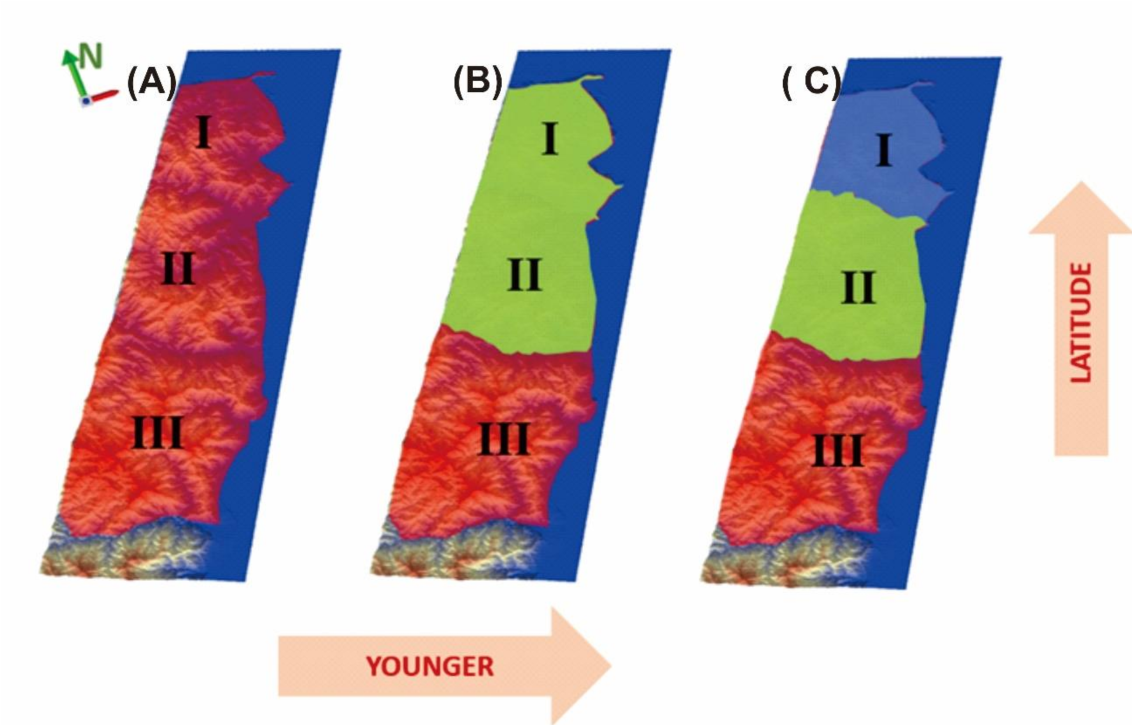

Figure 1.2: A proposed evolution model of fracture patterns in NE Taiwan. (A) First stage: The reverse faulting regime (red area) created a fracture pattern, which is corresponded to the collision time. (B) 2nd stage: Before the opening of Okinawa Trough, the flip of the subduction system PSP-EP in the northeastern most of Taiwan triggered the strike-slip faulting regime in Domain II and I (light green area). It developed fractures slipped and dilated in this stress state. (C) Final stage: The opening of the Southern Okinawa Trough was influenced the construction of fracture in normal faulting regime and punctured to NE Taiwan to form the Ilan Plain.

1.1.3 The reliability of digital elevation data in the geological examination

Fracture and fault can be indicated by lineaments, which is expressed in the topography. Additionally, lineaments are usually associated with the fault, the linear zone of fracturing, folding, as well as linear chains of some geological features. Quantitative approaches to reveal and classify fractures and faults by examining lineaments from remotely sensed images have been repeatedly consideration (Wilson, 1941; Lattman, 1958). Vinogradova and Eremin (1971) are the first researchers who operated photogrammetric procedures to reveal and classify fractures, as well as to measure their strike and dip angle.

In current time, accompanied with the progressive development of remote sensing research, geologists started to employ some standard techniques of digital elevation model to identify the fractures, such as a 3D topographic model constructed from aerial or satellite images (Campagna and Levandowski, 1991; Morris, 1991; Kukowski et al., 2001, 2008). Moreover, in recent years, the Digital Elevation Model (DEM) process can enhance "the contrast" of topography, which allows us to identify lineaments and fractures exposed on the surface. It has been providing the visualization of geological lineaments and their relationship to nearby geometric and geologic features. Especially, in the 3D model investigation, those geologic features exposed on the surface can be identified and classified by high-resolution DEM data. Further important applications of DEM data are the characterization of the fault and fracture system (Masoud and Koike, 2011a&b) and the construction of fracture plane from interpreted lineaments (Koike et al., 1998). The previous studies used DEM data to identify the dip direction of the bedding plane in sedimentary rock and examine equivalent structure geology (Cracknell et al., 2014).

In this study, we examined and recognized surface fractures at NE Taiwan from 5-meter DEM data. The lithology of NE Taiwan is dominated by metamorphic rock. In the counting, 2/3 rocks are schist and related schist. Fracture planes might be able to distinguish from foliation planes by cross-cutting relationships, which are present in the 3D DEM environment.

1.2 Purposes

The main purpose of this study is to correlate the existing or pre-existing fracture pattern on the surface with applied stress state inferred from the underground focal mechanism. The contribution of the 3D nucleated fracture map construction in this study aim to achieve steps (1) to investigate the significant characteristics to distinguish the fracture and foliation in the 3D DEM environment by cross-cutting relationship because we examined fracture planes in metamorphic rock; (2) produces the 3D nucleated fracture map with reliable, determined strike and dip of fracture planes from DEM data and constructs the cross-section of stress state by inverted focal mechanism data; (3) evaluate fault instability of reasonable surface fractures in an applied stress state to construct the 3D nucleated fracture map at NE Taiwan.

CHAPTER 2: GEOLOGICAL BACKGROUND

2.1 Tectonic setting

2.1.1 Taiwan mountain belt

The Taiwan orogenic belt was developed by the ongoing oblique collision between EP and PSP since the late Cenozoic (Ho, 1986; Teng, 1990). It is the consequence of the collision between mostly N-S trending of the Luzon volcanic arc and NE-SW trending of EP continental margin, which mainly constructed the current high topography of this island (Chi, 1981, Suppe 1981). According to Yu et al. (1999), PSP overrode northwestward in EP along the Manila trench with the rate 80 mm/ year. And this collision had begun in northern Taiwan a few million years before just now happened in the southern Taiwan island (Huang et al., 2012). And the suture zone of this collision is proposed as the Longitudinal Valley in southeastern Taiwan (Shyu et al., 2005). Besides that, the flipping of subduction polarity between PSP and EP caused by slab break-off (Teng et al., 1996; Teng et al., 2000) promoted PSP subducted under the EP resulting in the Ryuku Trench and Okinawa Trough (Yu et al., 1997; Wu et al., 2010) in the late Cenozoic (Fig 2.1). This subduction system, accompanied by the volcanic arc-continent collision, has been proposed to cause the post-orogenic collapse in NE Taiwan (Teng et al., 2000) and furthermore to form the Ryukyu trench and develop the NW-SE opening of the back-arc basin Okinawa Trough in northeastern Taiwan (Fig 2.1).

According to previous works, the crustal thickness decreases from > 33km to < 18km affiliated with the topographic drop from northern Taiwan to southern Ryukyu (Wu, 1978; Lee et al.,1980; Yen et al., 1995). Moreover, the formation of Okinawa Trough was associated with the Pliocene-Quaternary andesites of orogen strata. Extensional structures resulted from actively numerous submarine volcanoes located in the southwest Okinawa Trough (Lee and Wang, 1988) cut across the compressional structure by the andesites. Therefore, the Taiwan mountain belt involves the kinematic evolution of the different orogenic processes that evidential for the transition of the EP continental to PSP oceanic subduction from south to north of NE Taiwan (Malavieille et al., 2019).

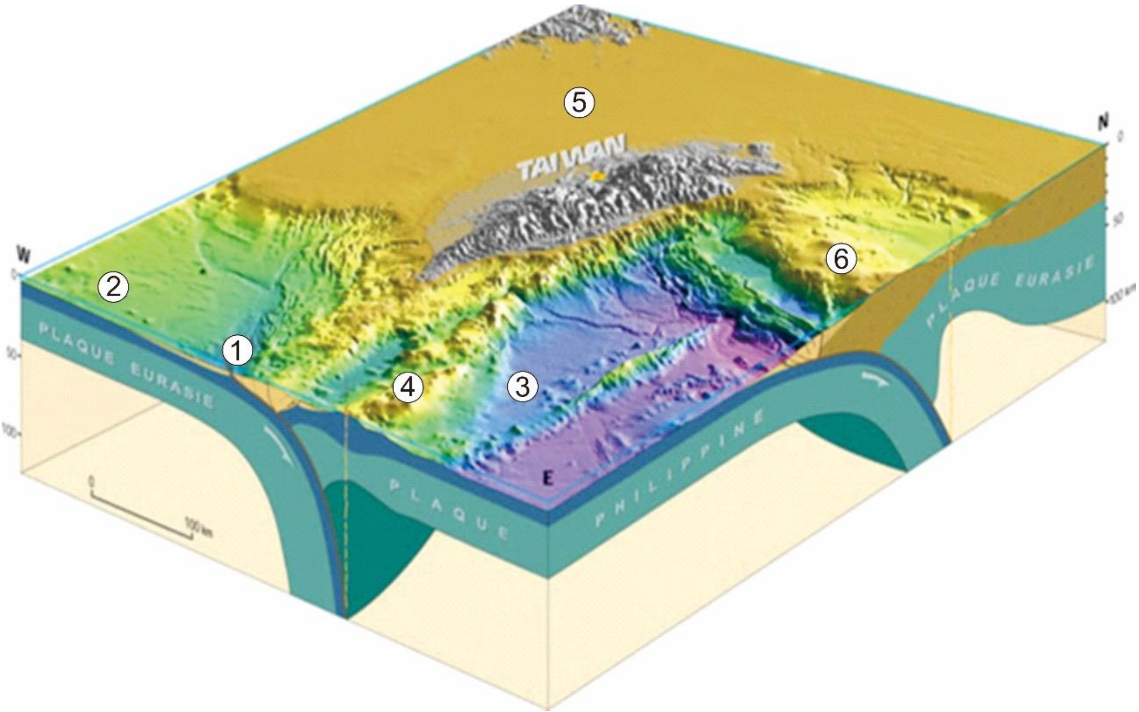

Figure 2.1: 3D model of the tectonic setting of Taiwan. In southwestern Taiwan, the oceanic crust of the South China Sea (2) subducted eastward under the PSP and created LVZ (4) along the transition area China continental margin. In eastern Taiwan, the northwestward movement of the western edge of PSP (3) collided with LVZ and overrode the EP (5) in the south, whereas it subducted beneath EP in the north along the Ryukyu arc (6) of NE Taiwan. (Malaivielle et al., 2019).

2.1.2 Kinematics in NE Taiwan

NE Taiwan, where is experienced in different tectonic environments from the collision in the south to extension in the north (Fig 2.2), indicated that the stress regime has evolved from the southern to the northern part (Wu et al., 2008). The collision primarily constructed orogen and explained the existence of the thrust sheet, fold, and other compressional structures. Teng et al. (2000) supposed that the Luzon arc in the early Pliocene overrode the continental margin rapidly during the movement of PSP-EP collision system. As the eastward subduction of the continent margin, the collision orogen grows to the maximum in central Taiwan. In the north, the tectonic setting getting more complicated. Sibuet and Hsu (1997) supposed that the post-orogenic collapse of NE Taiwan related to the westward propagation of the PSP-EP collision system via the PSP-EP subduction system and back-arc spreading of the southern Okinawa Trough. And, the flipping of the Ryukyu subduction polarity system caused the extensional process, which is highly connected with the post-orogenic collapse. The break-down of NE Taiwan orogen is referenced by the reduction of topography in Ilan Plain and the eastern of oceanic crust of southern Okinawa Trough. The fast rifting caused the southward bending of the mountain belt in nearly E-W striking (Hsu et al., 2009). Therefore, numerous extensional and compressional focal mechanisms were recorded and addressed in northeastern Taiwan orogen (Wu et al., 2008; Huang et al., 2012) (Fig 2.2).

The compressional stress regime (thrust and strike-slip faulting) is dominant in most of Taiwan (Yeh et al., 2014) (Fig 2.2). However, local tectonic variation in NE Taiwan induced the different distribution of the stress regime. In particular, Wu et al. (2008) and Wu et al. (2010) suggested the focal mechanism range from thrust and strike-slip faulting in the Hualien to normal faulting in the transition area and Ilan Plain. Especially, Wu et al. (2008) indicated that the trend of the tensile axis near Ilan Plain is close to NW-SE trending, whereas the NW-SE orientation of the compression axis is dominant in the southern part of the Heping area (Fig 2.2). Therefore, it is significant to evaluate the evolution of the stress pattern in NE Taiwan.

Huang et al. (2012) determined regional stress patterns at NE Taiwan from the focal mechanism in NE Taiwan by relocated EQ events with magnitude >4.0 (depth <30km) (Fig 2.3). Particularly, six different stress groups were identified from 169 focal mechanisms. Within them, three groups are associated with our studies. Firstly, the thrust faulting regime with NW-SE principal stress (σ_1) is dominant in the Hualien area (Domain III), which is displayed by the red circle. In the Heping area (Domain II), Huang et al. (2012) found the two different clusters of strike-slip faulting regimes, the first strike-slip faulting in the southern Ilan Plain (Domain I) has σ_3 orientation consistent with the opening direction of Okinawa Trough, whereas σ_1 orientation of the second strike-slip faulting regime in the Heping area might have corresponded with arc-continent collision. The light green square stress regime (Fig 2.3) of the Heping area represented the earthquake events with an NNW-SSE orientation of σ_3 and an ENE-WSW orientation of σ_1. Meanwhile, in southern Ilan Plain, the light green triangular stress regime (Fig 2.3) has a trans-tension stress pattern.

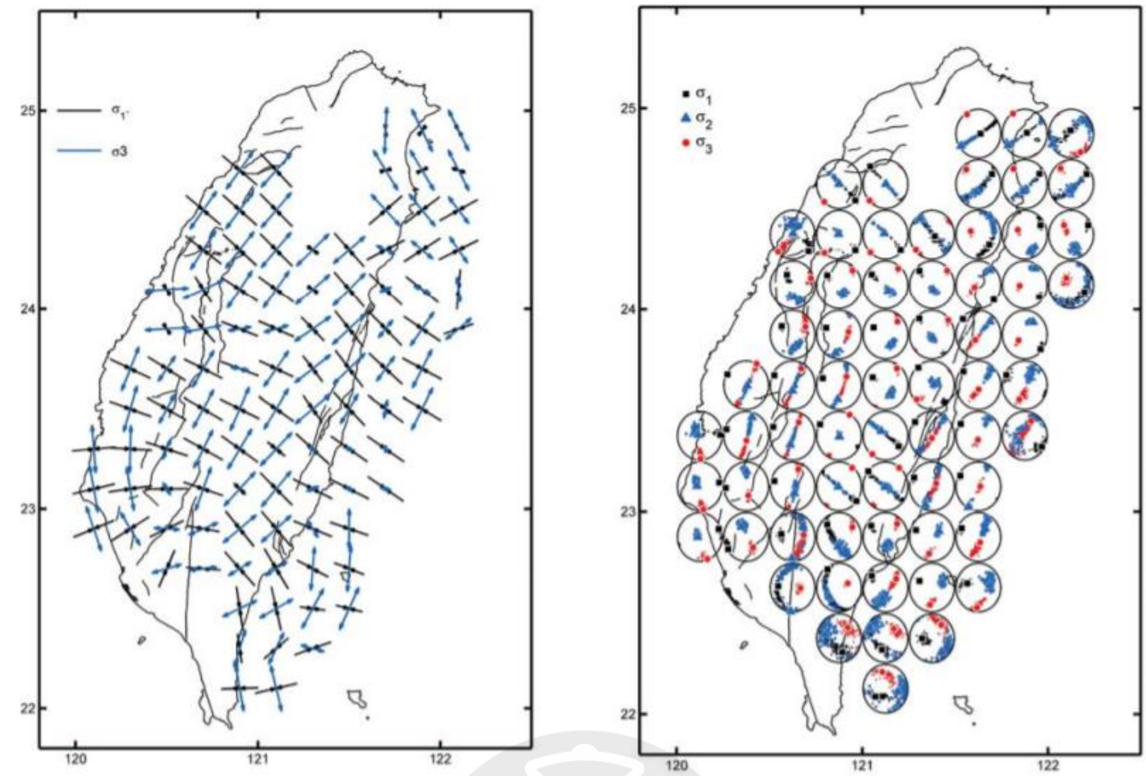

Figure 2.2: The kinematics of Taiwan island from stress tensor inversion. Surface projection of the σ1 and σ3 axes (left) and the different principal axes in the equal-area projection of the lower hemisphere (Wu et al., 2008).

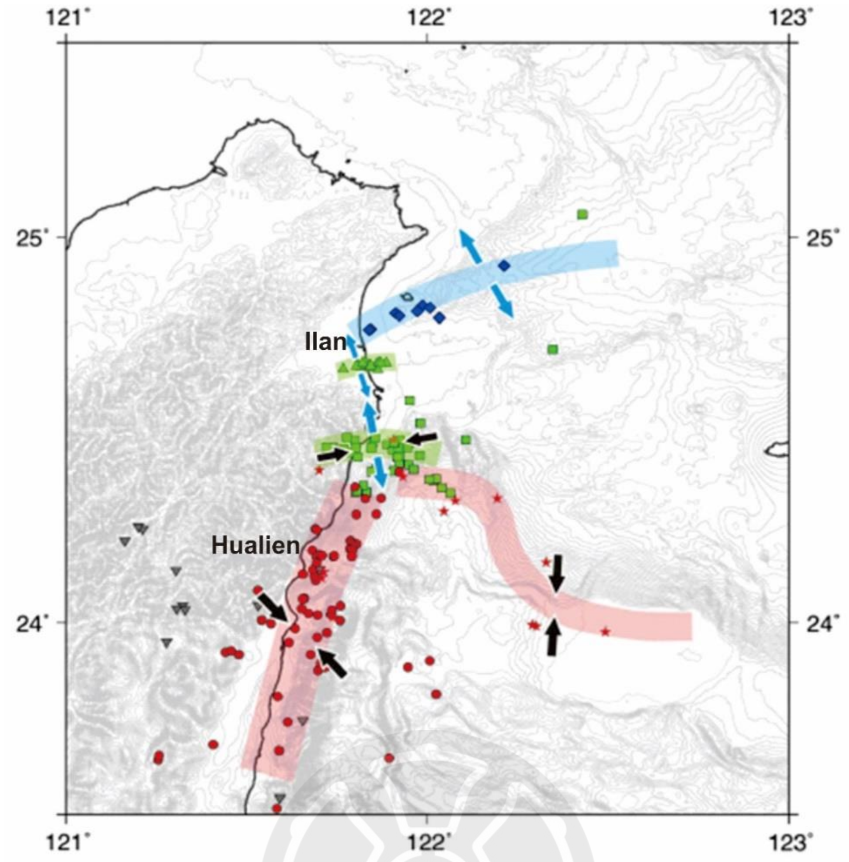

Figure 2.3: The evolution of the stress state in NE Taiwan. The result of the focal mechanism analysis from Huang et al. (2012) emphasized the stress state evolution in Northeastern Taiwan. In this figure, the normal-faulting focal mechanism cluster illustrated by the blue dots is dominant in Ilan Plain. High density of reverse-faulting cluster was discovered in Hualien county with the red dots and the strike-slip faulting cluster highlighted by green dots located in the central part of study area.

2.2 Geological Background

Taiwan orogen can be classified by six narrow geologic units parallel to the long axis of the island (Fig 2.4A). From west to the east, they comprised of the Coastal Plain (CP), the Western Foothill (WF), the Hsueshan Range (HR), the Central Range (CeR); the Longitudinal Valley (LV), and the Coastal Range (CoR). Inside, CeR contains the Tananao Schist (TC) (Ho, 1988). The Tananao Schist is the oldest metamorphic basement of Taiwan, experienced several phases of orogenic deformation, magmatism, and metamorphism (Wang, 1966; Ernst et al., 1983; Stanley et al., 1981). Especially, the higher metamorphic grade that occurred in the northeastern part of Tananao schist might be caused by the strong influences of the tectonic evolution of Taiwan. Furthermore, Tananao Schist can be divided into two metamorphic belts: the western Tailuko belt and the eastern Yuli belt (Ho, 1986). This research addressed the northeastern Tailuko belt (red box, Fig 2.4B).

NE Tailuko belt is mainly composed of Pre-Tertiary metamorphic rock such as pelitic schist, gneiss, migmatite, metamorphosed limestone, greenschist, and amphibolite. The detail will be described below.

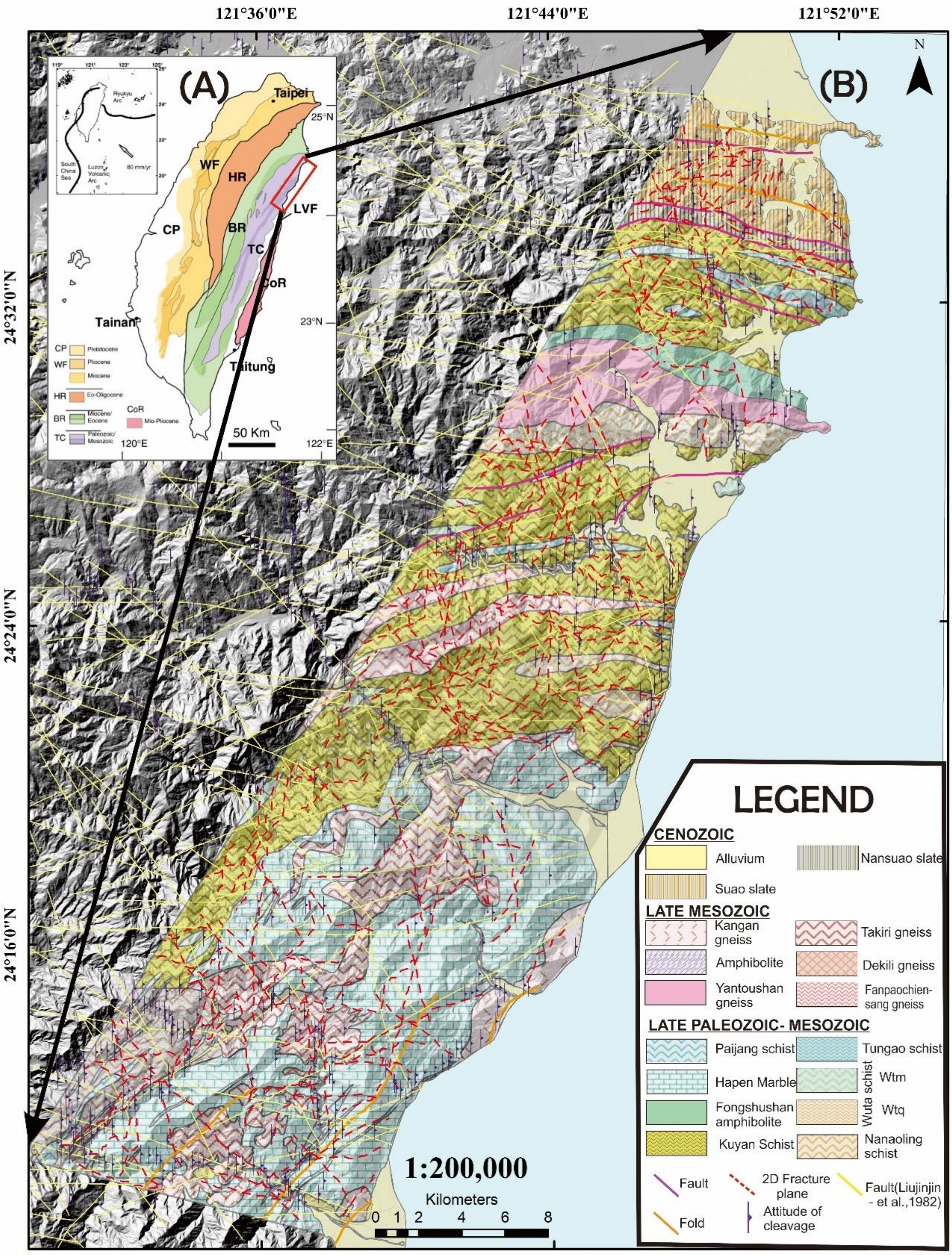

Figure 2.4: (A) Geological units of Taiwan (Ho, 1988), (B) The Geological map of NE Taiwan (Geological Central Survey, 1995).

Table 2.1: Lithological units in the study area (Central Geological Survey, 1995).

	Stratigraphical division	Lithology
CENOZOIC	Nansuao formation	Slate; Metastone and slate in alternation
	Terrance deposit	Gravel; sand and mud
	Alluvial deposit	Gravel; sand and mud
	Suao Formation	Slate and argillite with a thin bed of metastone
LATE MESOZOIC	Yuantoushan gneiss	Gneiss or metamorphosed granodiorites
	Metabasite	Metabasite
	Kangyang gneiss	Green-greenish granite and gneiss
	Dekeli gneiss	Green-greenish granite and gneiss
	Fanpaochienshan gneiss	Gneiss
	Amphibolite	Amphibolite
LATE PALEOZOIC TO MESOZOIC	Paijang Schist	Greenschist; siliceous schist and marble interlayer
	Happen Marble	Thick – bedded marble
	Fongshushan amphibolite	Amphibolite and horblende schist
	Tungao Schist	Marble; Amphibolite; Graphite schist and quartz-mica schist
	Wuta Schist	Marble and chlorite schist; Chlorite schist; Quarzt-mica schist
	Chiuchiu Marble	Thick-bedded marble, dolomite and chlorite schist intercalation
	Nanaoling Schist	Quarzt schist; paragneiss
	Kuyan schist	Phyllite; micaceous schist and quartz to mica schist

2.2.1 Pre-Tertiary metamorphic rock

The wide-spread lithological units in the basement can basically be classified into several complex series of geological features as listed below:

Kuyam schist belongs to Nanao Peak Schist (124-125.5K) located in the western Central Cross-Island Highway.

Nanaoling Schist incorporated with Tungao Schist became Donao Schist at 115-122.6 K along Central Cross-Island highway. In the Suao-Nanao area, they are lenticular bodies that interbedded with other kinds of metamorphic rocks.

Chiuchiu Marble is accompanied by the Happen marble located in the Suao-Hualien highway, north of the Heping area. They are lenticular metamorphosed limestone, which intercalated in the schistose rock (Ho, 1988). It is characterized by massive and thick-bedded and ranged from fine to coarse-grain.

Paijang schist was featured by lenticular greenschist, siliceous schist, and marble alternation. The greenschist are derived from mafic volcanic flows or pyroclastic rocks. Especially, the chlorite schist of Wuta schist formation is easily accompanied by the greenschist, and it has fine to medium-grain.

Amphibolite is elongated lenticular bodies that well-foliated rock distributed in the northern Nanao area. Its foliation plane is generally parallel to that of surrounding schist.

Six gneiss bodies were discovered by Yen (1954) contained two large gneiss bodies in the north and others contacted with metamorphosed limestone in the south. Granitic texture, which explained for the intrusion of the granite mass into the pervasive greenschist facies metamorphism. (Fuh, 1962) is characterized as the orthogneiss.

2.2.2 Tertiary metamorphic rock and sediment deposit

Nansuao and Suao formation located in the north of the study area. The rocks contained black to dark grey argillite, slate, and phyllite, and occasional interbeds with dark gray compact sandstone are characterized by the low metamorphic grade. Gravel, sand, and mud were deposited as alluvial and terrace that were distributed in the stream area.

CHAPTER 3: METHODOLOGY

The methodology of our research was briefly summarized in Fig.3.1. There are three major parts: (1) Using the 5-meter Digital Elevation Model to identify surface fracture planes and calculate their attitudes; (2) Operating the stress inversion program to obtain the stress state at NE Taiwan from focal mechanisms data of 1991-2016; and (3) the correlation of surface fracture pattern with a given stress state can help us creating 3D Fracture Nucleation Map.

Several geological definitions will be clarified in the first part of this chapter.

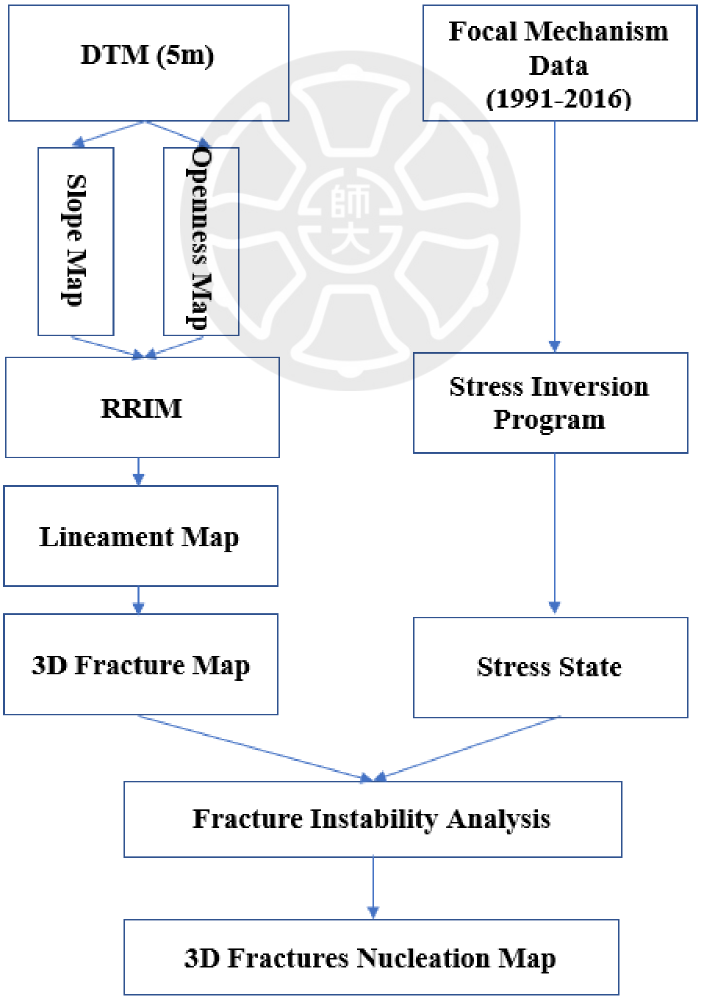

Figure 3.1: Flowchart of the method.

3.1 Geological definitions

3.1.1 Foliation

In general, foliation is a geological term defined for any planar fabric or curve structure (Fossen, 2016). There are two types of the foliation: primary foliation was formed during the formation of magmatic rock or deposition of sedimentary rocks, and secondary foliation is tectonic foliation responded to the deformation process.

Tectonic foliation is the penetratively structural fabric defined by zones of different grain size and flattened object or recrystallized tabular grain with the uniform orientation (Fossen, 2016). Therefore, the planar, parallel, triangular faces observed from the topography of metamorphic terrain is characterized as the existence of specified sheet texture in the 3D environment of Arc Sense. Under the surface processes, the foliated rock may easily split when the force overcomes its cohesion.

3.1.2 Fracture

Fracture in geology is a common term composed of structure features such as faults, joints, veins, dikes, and sills (Schultz and Fossen, 2008; Peacock et al., 2016). However, in this study, we proposed that the tectonic fracture is composed of only faults and joins, and they can reveal in digital elevation data. The study of Pollard and Aydin (1988) aimed to distinguish the joint and fault by the opening model and shear model.

- *Extension fracture:* where the fracture walls move apart, *opening model,* and may contain joints or faults.

- *Shearing-mode fractures:* a general term for discontinuity features along the wall rocks move sub-parallel to the plane of the fracture. These include fault and fault zones.

3.1.3 Stress tensor

Stress tensors are a specialized mathematic equation that can be used to define the Earth's forces. Individual components in a stress tensor are tractions acting perpendicular or parallel to three orthogonal planes. The normal axes to the three orthogonal planes define a Cartesian coordinate system. The stress tensor has nine components. Each of them has an orientation and a magnitude. Three of these components are normal stresses perpendicular to plan, whereas the other six are shear stresses, and their traction is applied along the plane in a particular direction.

3.2 Methods

3.2.1 DEM Database

In recent years, spaceborne satellite images, high attitude aircraft images, and their products, such as DEM, are highly efficient dataset able to characterize geologic features on the landform. Furthermore, it also is a reasonable source of information for the detection of crustal deformation patterns caused by faults and fractures (Wladis, 1999; Morelli and Piana, 2006). Because geology fieldwork is a costly, time-consuming, and sometimes dangerous undertaking, thus any beneficial techniques supported tool for effortless and convenient fieldwork should be considered. Therefore, in our research, we investigated the DEM of 5m raster cell data to analyze the surface fracture pattern along the coastline area of NE Taiwan under the 3D software environment. The surface patterns of the fracture plane can be recognized by geological lineaments. Therefore, we try to mapping lineaments through 2D view of the Red Relief Image Model (RRIM). Finally, 12536 lineaments were identified and picked through RRIM.

3.2.2 Red Relief Image Model (RRIM)

RRIM is a new conception of the geomorphology analysis that took a new approach of examining surface to classify geological structures. Compared with other topographic visualization methods such as contour map and shaded relief, RRIM eliminates the dependency of incident light direction and shows the 3D image without shadow (Chiba et al., 2008; Chiba and Hasi, 2016). Two landform element layers resulted in the RRIM (Chiba et al., 2008) are the topographic openness map and slope map. We used the Relief Visualization Toolbox (RVT 1.3) to create the openness map and slope map from DEM data. The RRIM was further created in Arc Map by overlap the topographic openness map and slope map. The adjustment of contrast, brightness, and transparency parameter of each layer in Arc Map software is required to clearly display RRIM.

3.2.2.1 Topographic Openness Map

The topographic openness map, including positive and negative openness maps, is an essential component to produces RRIM. Openness expressed the degree of dominance or enclosure of location on an irregular surface. The positive openness map refers to a calculation of concave-downward zenith angles. Yokoyama et al. (2002) concluded that positive openness represented the topographic ridges. On the others, negative openness referred to an evaluation with concave-upward nadir angles and characterized the valley (Fig 3.2A). Therefore, the concept of openness strongly emphasizes the dominance of concavities and convexities on the landscape. The zenith and nadir angles were computed the subtraction 90° to slope angles and calculated in eight different azimuth directions (D= 0; 45; 90; 135; 180; 225; 270; 315). The positive and negative values of the openness map were obtained by averaging angle for each direction. The openness map is designed by the gray tone to enhance its optimal detail and contrast. Positive openness takes a higher value of gray tones and generally encountered an expanse of terrain by one or several elevated relief features such as ridges (Fig 3.2B), while negative openness expressed the degree closure of the lower location as valley, river, or crater by elevated surroundings (Fig 3.2C) (Yokoyama et al., 2002). To successfully display the positive and negative map into ArcMap software, we need to adjust the contrast, brightness, and transparency parameters of each map. And the adjustments are continuously repeated until we observe clearly the topography. In summary, openness parameters highly support to highlight the different terrain features such as ridge, crests, gullies, or valleys (Fig 3.2D).

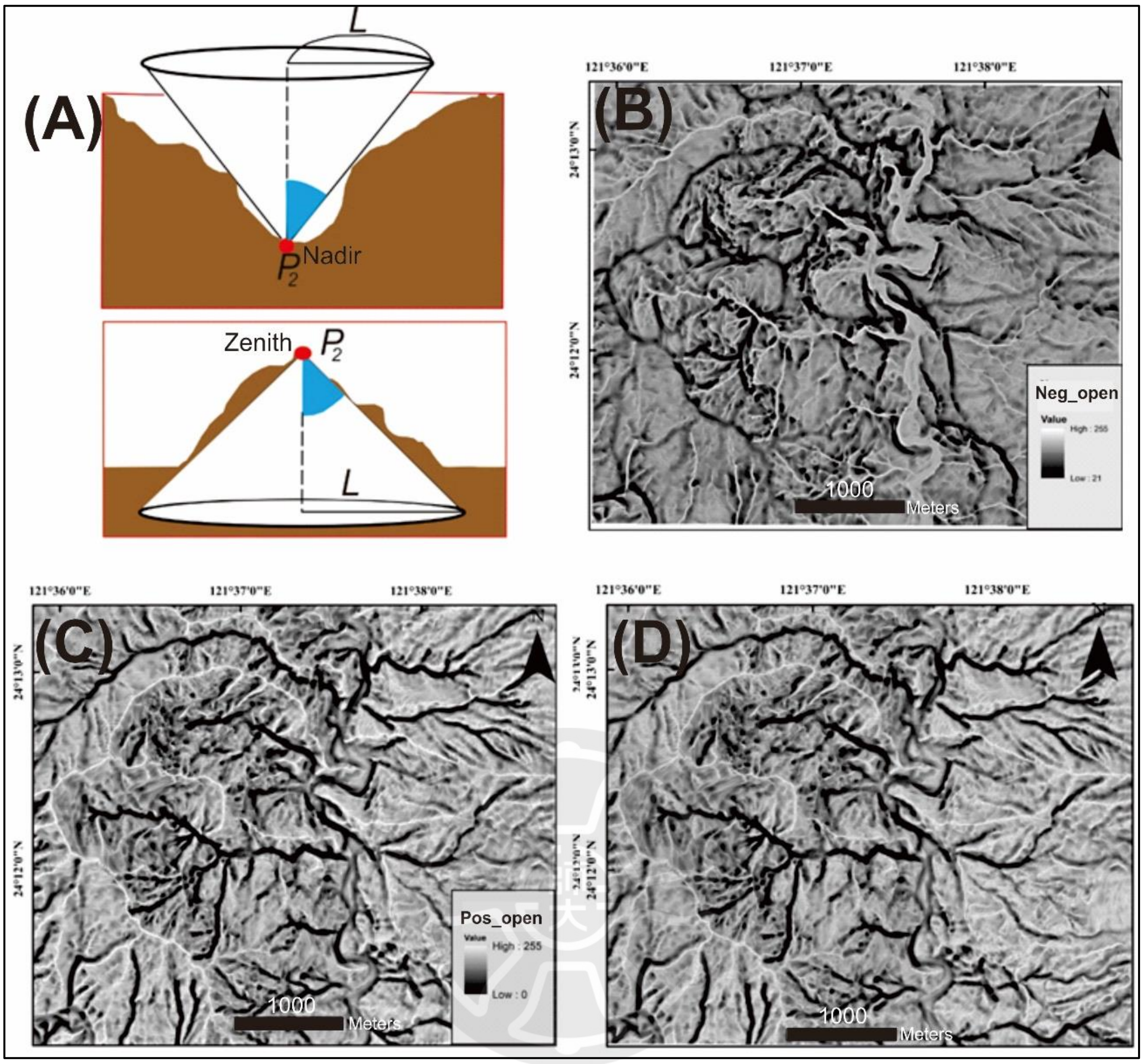

Figure 3.2: Elements of topographic openness map. (A) Using the nadir point to calculate the negative openness and zenith point to identify the positive value on openness map analysis (modified from Yokoyama et al., 2002). (B) Negative openness map. (C) Positive openness map. (D) Diagram of the concave and convex topography based on the concept of topographic openness map

3.2.2.2 Slope Map

The slope map was computed as the ratio of relief to irregular terrain surface and can be roughly identified topographic features of the area. If the openness map displays the gray tone in RRIM, the slope map layer is usually generated by a red color pattern because the red color has the richest tones for human eyes (Chiba et al., 2008). In similar, the contrast, brightness, and transparency parameters of the slope map also need to adjust. The slope map should be overlap with the topographic openness map and repeatedly adjust the parameter until the clearly observe topography (Fig 3.3). The yellow lineaments were mapped along the gullies and primarily indicated for the surface fracture traces in the 2D view of ArcMap software.

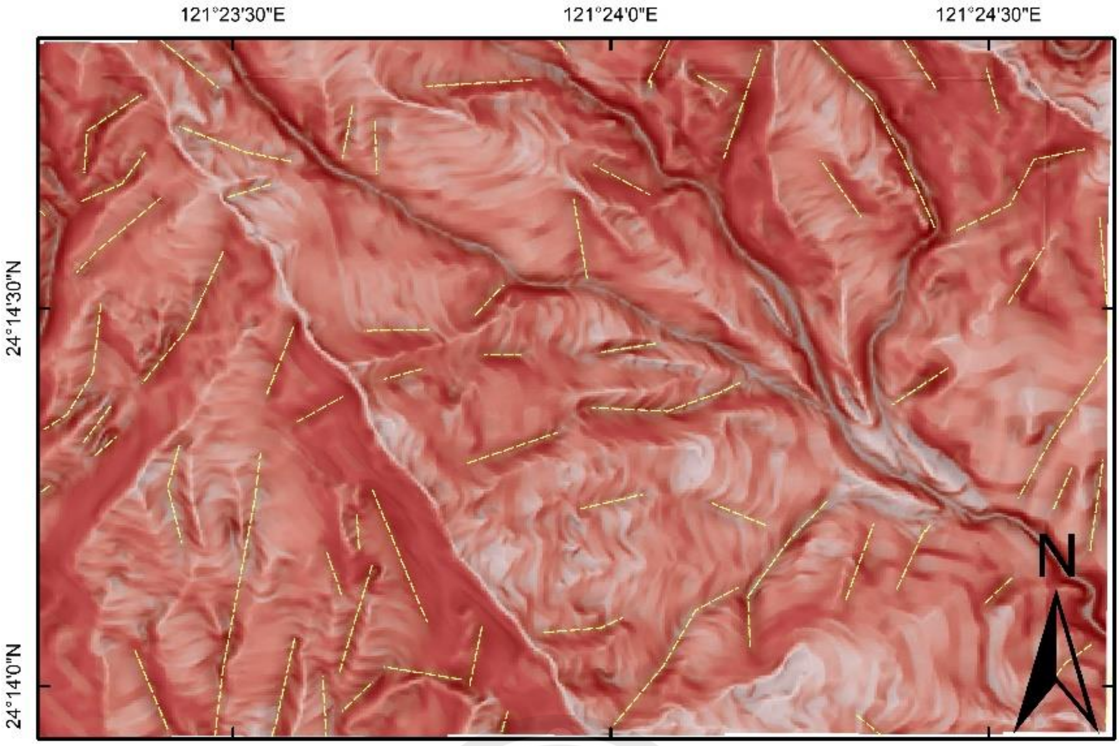

Figure 3.3: Red Relief Image Model. Yellow lineaments presented in the RRIM are emphasized the convex topography. Lineaments correspond to the straight or slightly curved edge of convex topography and might be affected by the geological features, such as join, fault or cleavage, etc. (Koike et al., 1998).

3.2.3 Lineament Map

Geological lineaments can be associated with the rupture of Earth's surface from a different origin such as structure, lithology, surface processes, etc. They commonly demonstrate a particular type of fracturing (Hobbs, 1904; Wise et al.,1985; Twidale et al., 2007). The topographic expression of the rupture area with the offset of the surface, differential erosion of juxtaposed units, or erosion of damaged rock could help us to classify the geological structures such as faults, fault zones, or joints, etc. Therefore, mapping lineaments is a necessary step for interpreting and examining the fracture plane.

Typically, lineaments displayed by straight or slightly curved components can be observed and recognized through high-resolution remote sensing data. The identification of lineaments distribution in the DEM is strongly dependent upon the effect of illumination such as azimuth, imagery declination angle, and view direction (Koike et al., 1998). However, RRIM enhances lineament quantity by the independent illumination for any viewing direction (Chiba et al., 2008).

The lineament map of NE Taiwan was generated by hand-picking the lineaments through RRIM. In this study, we recognized and picked lineaments along gullies, straight river banks, or broken ridge. It basically displays in RRIM by yellow dash lines (Fig 3.3). In total, we mapped 12536 lineaments in the coastline area of NE Taiwan. The fracture planes can be identified based on the distribution of lineaments in the 3D view.

3.2.4 Extraction of Fracture Attitude

RRIM overcomes the shortcoming of the illumination problem to identify the lineaments, which might be considered as a trace of the fracture plane. Fracture planes are three-dimensional and are commonly represented in the spatial by attitude (Fig 3.4). In the field investigation, the attitude of fractures is examined on the surface by using the clinometer. The strike and dip direction of the fracture surface are commonly measured.

In recent years, the development of the reformative resolution of digital elevation data was able to obtain the strike and dip of the sedimentary bedding (Yeh et al., 2014). It follows the same traditional principle method that the dip angle was calculated by measuring the angle between bedding and horizontal plane (Fig 3.5). They defined that the sedimentary bedding planes in the LiDAR are measurement triangles. Each measurement triangle contains more than three points to compute a regression plane. The strike and dip of the bedding planes are acquired from the attitude of the regression planes (Fig 3.6).

In this study, we tried to use the DEM with 5 meters of resolution to conduct the 3D fracture map. We also assume that fracture planes in the spatial are shaped as the triangle and should be fitted with the regression planes. At least three measurement points defined the triangle, but more than three points are needed to obtain the smooth and correctly triangle. To conduct the 3D fracture map, we floated the lineaments map into the 3D environment of Arc Sense. After that, hand-picking the triangle planes (S), which are defined by the group of green dots (Fig 3.5) in 3D environments. The attitude of fracture planes was calculated by measuring both the intersection and the inclined angle between a triangle (S) and the horizontal plane (H) (Fig 3.5).

In the TM2 coordinate system, the x and y gave the longitude and latitude of the point, while z is the elevation above a given datum. The regression plane can be represented by z= ax+ by+ c. To derive the strike and dip of the measurement triangle, we take the cross product of the normal measurement vector and the normal horizontal plane vector (Fig 3.6). Calculating the gradient of two-variable function can reveal the dip direction of any point on the surface: $\vec{v}_{dip} = \nabla z = (\partial z/\partial x)\vec{\imath} + (\partial z/\partial y)\vec{\jmath}$, where $\vec{v}_{dip}$ is the fracture plane dip direction and $\vec{\imath}, \vec{\jmath}$ are the unit vector of x, y-direction. The dip angle was calculated by the following equation: $S_{dip} = \|\vec{u}_{dip}\| = \|\vec{v}_{dip}/\|\vec{v}_{dip}\|\|$. The strike vector can be calculated at any point over the regression surface using the following equation: $\vec{v}_{strike} = \vec{n}_{dip} \times \vec{n}_{zsurface}$, where $\vec{v}_{strike}$ is the strike direction, $\vec{n}_{dip}$ is the dip unit vector, and $\vec{n}_{zsurface}$ is the unit vector of the regression surface in z. The angle between the north and strike direction is considered as the strike value.

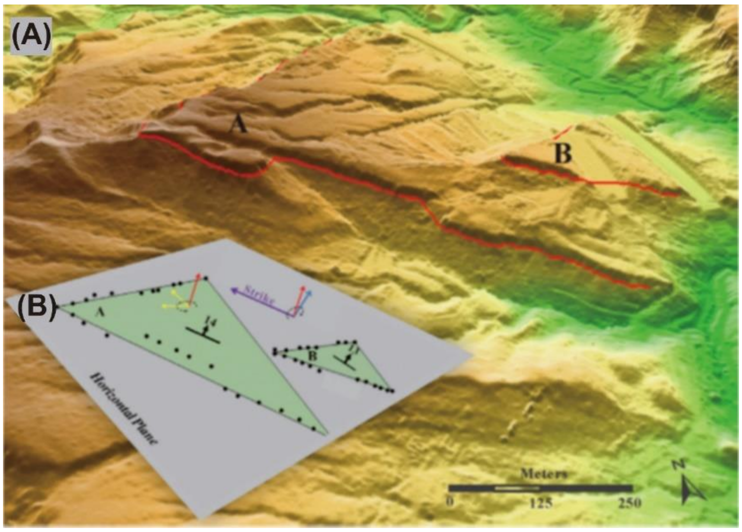

Figure 3.4: Illustration of plane attitude from LiDAR. (A) The bedding planes. (B) The spatial vector calculation for bedding planes A and B. Two triangles are the planes regressed from the black dots (Yeh et al., 2014).

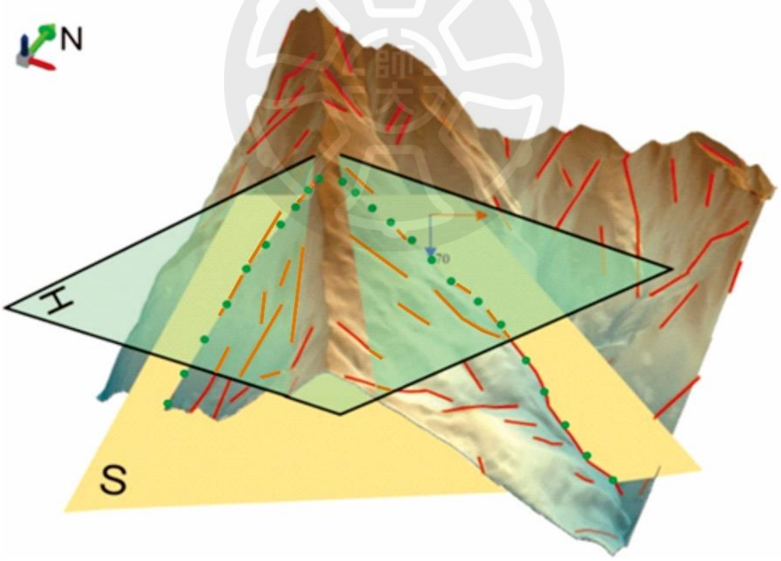

Figure 3.5: Demonstration of fracture planes from lineaments in the 3D view of Arc Sense software. The fracture plane was defined as the yellow triangle. The strike and dip angle calculated from the result of the intersection between the fracture plane (S) and the light green horizontal plane (H). Many green measurement points were conducted on the fracture plane based on several lines in the 3D environment.

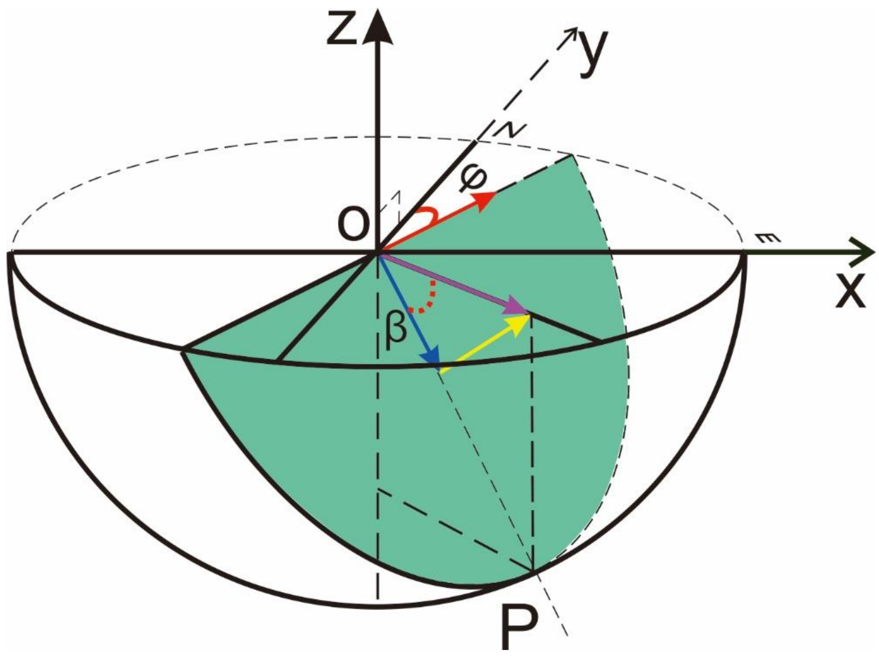

Figure 3.6: The calculation of fracture and foliation plane attitude in lower hemisphere projection. The dark green imaginary fracture plane is plotted in the lower hemisphere. The red, dark blue, yellow, and purple arrow indicated for the strike, dip direction, normal measurement triangle, horizontal vector. They are supported to calculate the fracture plane attitude.

3.2.5 Stress Inversion and Instability Analysis

3.2.5.1 Focal mechanism data

In this study, we used 295 focal mechanisms data from earthquake events in Taiwan from 1990 to 2016 (Wu et al., 2008) for producing the cross-section of the stress state of NE Taiwan because the focal mechanism of earthquake events displays the stress regime patterns resulted from regional tectonic setting. Additionally, Scholz (2002) indicated that the aspects of the stress field might be associated with the fracture possesses in the Earth's crust. Also, the stress fields might construct the new fracture from the intact materials or change the kinematic behavior from pre-existing fractures. For this study, we calculated the fracture instability to evaluate the development of nucleated fractures from stress evolution. The approach of reactivation potential at any existing fractures will discuss in Chapter 5 by examining slip tendency.

In detail, to model the stress state of three different domains in NE Taiwan, we analyzed the movement of the seismic fault of the focal mechanism. This method solves the maximum shear stress direction on the fault, which was assumed by Wallace (1951) and Bott (1959), to determine the stress state of NE Taiwan. Furthermore, we try to calculate the three direction cosine of principal stress and relative size (Φ) in the Mohr's circle by applying the reduced stress tensor method.

3.2.5.2 Reduced stress tensor

Reduced stress tensor was first introduced by Bott. (1959), which applied to reconstruct three principal stresses axes and stress ratio (Φ) from the conjugate faults system in the isotropic media. The conjugate faults are mainly caused by the consequence of deformation-induced by the stress field. The fault movement along the fault plane, when earthquake happens, is assumed to be induced by stress tensor. The direction and sense of slip vector that occurred in the fault plane are assumed to be the same with those maximum resolved shear stresses. Hence, whether we knew the orientation and senses of fault movement on the fault plane, reduce stress tensor can be instituted. To solve reduced stress tensor, four unknown independent parameters should be obtained. Therefore, we primarily calculate the eigenvalue and eigenvector in order to determine the orientation of principal stress axes and stress ratio.

3.2.5.3 Effective stress calculation

In order to analyze seismic fault instability, we need to obtain the effective stress. The reduced stress tensor included only the direction of the principal stresses and the stress ratio (Φ). And the stress ratio has governed the shape of Mohr's circle but remains Mohr's circle size and position unknown because it depends on the unknown quantities of differential stress and means stress magnitude. To determine the exact position of Mohr's circle, Lisle and Srivastava (2004) assumed that the k_1 and k_2 are unknow parameters related to the absolute size and position of the Mohr's circle, and the frictional sliding envelope is tangential to the σ_1 and σ_3 Mohr circle. Thus, the stress states compatible with a known Φ were calculated by:

$$\sigma_1 = k_1 + k_2$$
$$\sigma_2 = k\Phi + k_2 \qquad \text{(Eqn. 3.1)}$$
$$\sigma_3 = k_2$$

The effective stress was calculated by applying the assumption of Mohr's circle tangent with the Mohr-Coulomb failure criteria. Therefore, the notable magnitude of principal stresses compatible can be calculated with the rock mechanics data and stress ratio and orientations. The average frictional angle and rock cohesion for the failure criteria basically were calculated from the rock strength database with area weighting are 49.5°, 7.2MPa, respectively (Table.3.1). Besides that, the effective stress is considered. Pore pressure (p) static increases with depth. The rock density is 2.7 g/cm^3. Consequently, we can estimate the instability of fracture varies as a function of its orientation concerning the magnitude of the principal stress.

Table 3.1. The summary of rock mechanics data (SNFD-ITRI-TR2016-0002-V5PN_SNFD2017).

Lithology	**Area (m^2)**	**Friction angle (°)**	**Cohesion (MPa)**	**Tensile strength (MPa)**
Marble	4306201	57.1	13.8	8.41
Schist	118651907	48	4.11	8.38
Gneiss	13532320	56.8	32.63	10.44
	136490428	49.16	7.24	8.58

3.2.5.4 Fracture Instability

The differently oriented faults have different susceptibility to be active and be individually unstable in the given stress fields. To evaluate the fault instability, Vavrycuk et al. (2015) primarily determined the unstable fault plane from the focal planes by quantified with the Mohr-Coulomb failure criterion. According to this criterion, shear traction (τ) on an activated fault must exceed a critical value (τ_C) (Eq. 3.2) (Beeler et al., 2000; Scholz, 2002), which is calculated from cohesion C, fault friction μ, compressive normal stress (σ_n), and pore pressure (p) (Eq. 3.3).

$$\Delta\tau = \tau - \tau_C \qquad \text{(Eqn. 3.2)}$$

Where $\tau_C = C + \mu(\sigma_n - p) \qquad \text{(Eqn. 3.3)}$

They demonstrated that the distribution of fault planes inside the unstable area (red area in Fig 3.7) corresponded with the principal fault plane of the focal nodal plane. The concept of instability (I) was introduced, and fault instability of all fault orientation can be defined in the range from 0 to 1 (Fig 3.7) by the following formula (Vavrycuket al., 2015).

$$I = \frac{\tau - \mu(\sigma - \sigma_1)}{\tau_c - \mu(\sigma_c - \sigma_1)} \qquad \text{(Eqn. 3.4)}$$

Where τ_C, σ_C is the shear, and effective normal stresses along the principal fault plane from focal mechanism data and τ, σ is shear, normal stress along the DEM-derivation surface fracture.

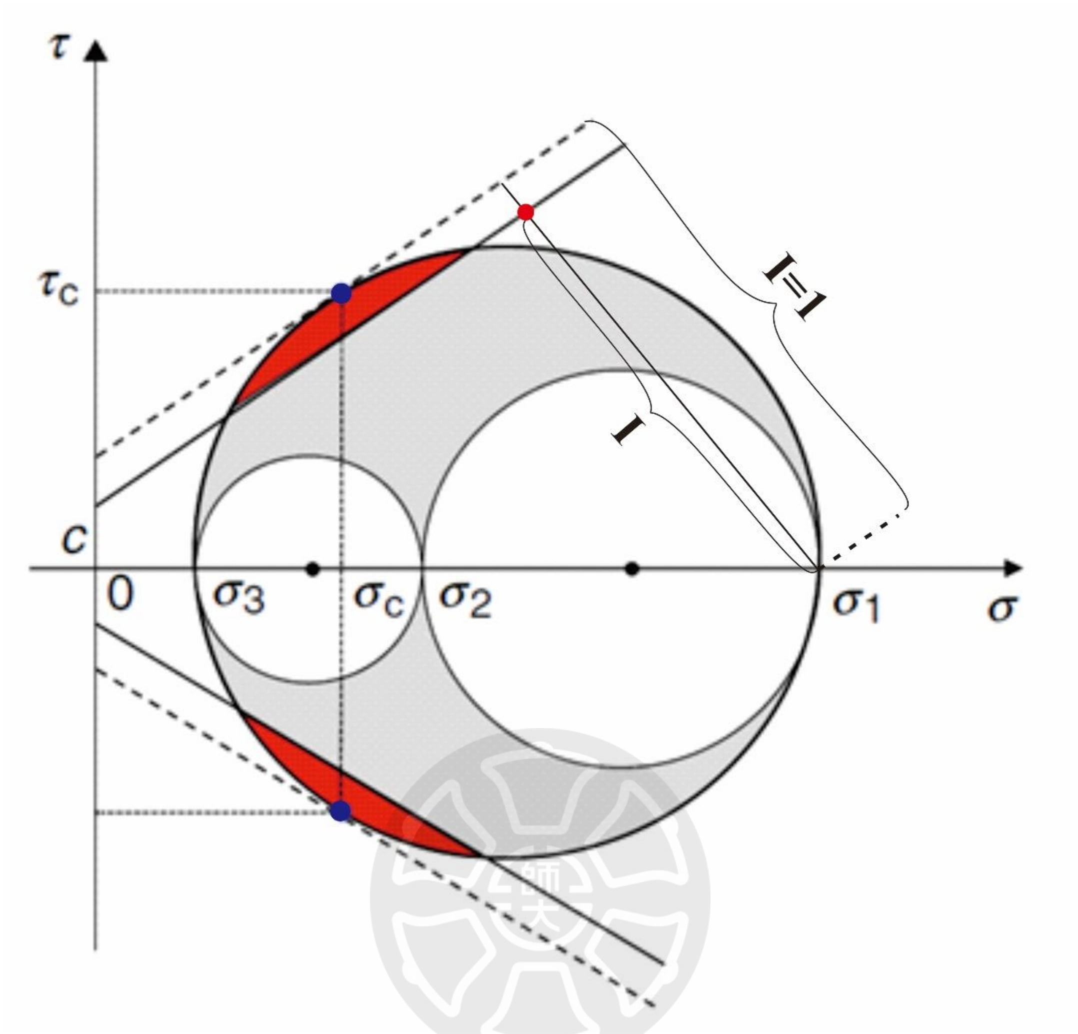

Figure 3.7: Fault instability in Mohr ‘s diagram. The red area marked unstable areas of principal fault planes from focal mechanisms, and blue dots characterized the principal fault instability I=1. The red dot marks an arbitrarily oriented fault with instability I. τ, σ are the shear and effective normal stresses, respectively. σ1, σ2, and σ3 are the effective principal stresses. (Modified from Vavrycuk et al., 2015).

CHAPTER 4: RESULTS

4.1 Identification of fracture and foliation

On a large scale, the consequence of the deformation structure and weathering process might support the significant modification of landform by several activities such as uplift, crustal thinning, surficial erosion, or deposition process. These activities can occur in a variety of deformation styles, such as ductile, ductile-brittle, or brittle modes. The cutting-relationship among individual fracture planes or between fracture and foliation is considered as a priority to characterize the fracture and foliation planes in the metamorphic area. The cross-cutting relationship also provides the relative age information of fracture sequences. Therefore, four locations were picked up at different domains (Fig 4.1) to demonstrate the relationship between fracture and foliation plane and its characteristics.

4.1.1 Attitude of foliation planes

In the 3D view of Arc Sense, several foliation planes were exhibited in Figure 4.2A. And, purple lineaments (Fig 4.2B) were identified and mapped through RRIM in the same area (Fig 3.3). The foliation planes were highlighted by the small dark blue triangle planes in the DEM data (Fig 4.2C). The 3D parallel, planar, triangle faces are characterized as foliation planes in 3D view. Figure 4.2D indicated that the features of planar morphologic geometry of foliation (purple lines) in the ridge where was truncated by fracturing (red and green arrows). Fracture planes with NW-SE strike and west-dipping (red arrows) and ENE-WSW strike fracture planes (green arrows) cut and broke the foliation, and foliation became the discontinuously geological features (Fig 4.2D). Although in detailed observation, the fracture surfaces are gently unsmooth due to the influence of surface process, the fracture plane still is able to be mapping. In summary, the foliation and fracture planes can be observed by using the DEM with GIS relevant applications. Furthermore, their attitudes have the potential to calculate if they are clearly exposed on the surface by one plane. The calculation of foliation attitude was following a similar approach to fracture planes. The results were examined in three representative locations for three domains of this study area. The foliation characteristics in the 3D environment are shaped by parallel triangle faces, and, in comparison, the results of the foliation attitude calculation from DEM were similar to attitudes with field data from the geological map (Fig 4.2E). Therefore, the research methodology of this study is the potential to apply in the calculation of fracture attitudes.

Figure 4.1: Location map of geologic features in the study area.

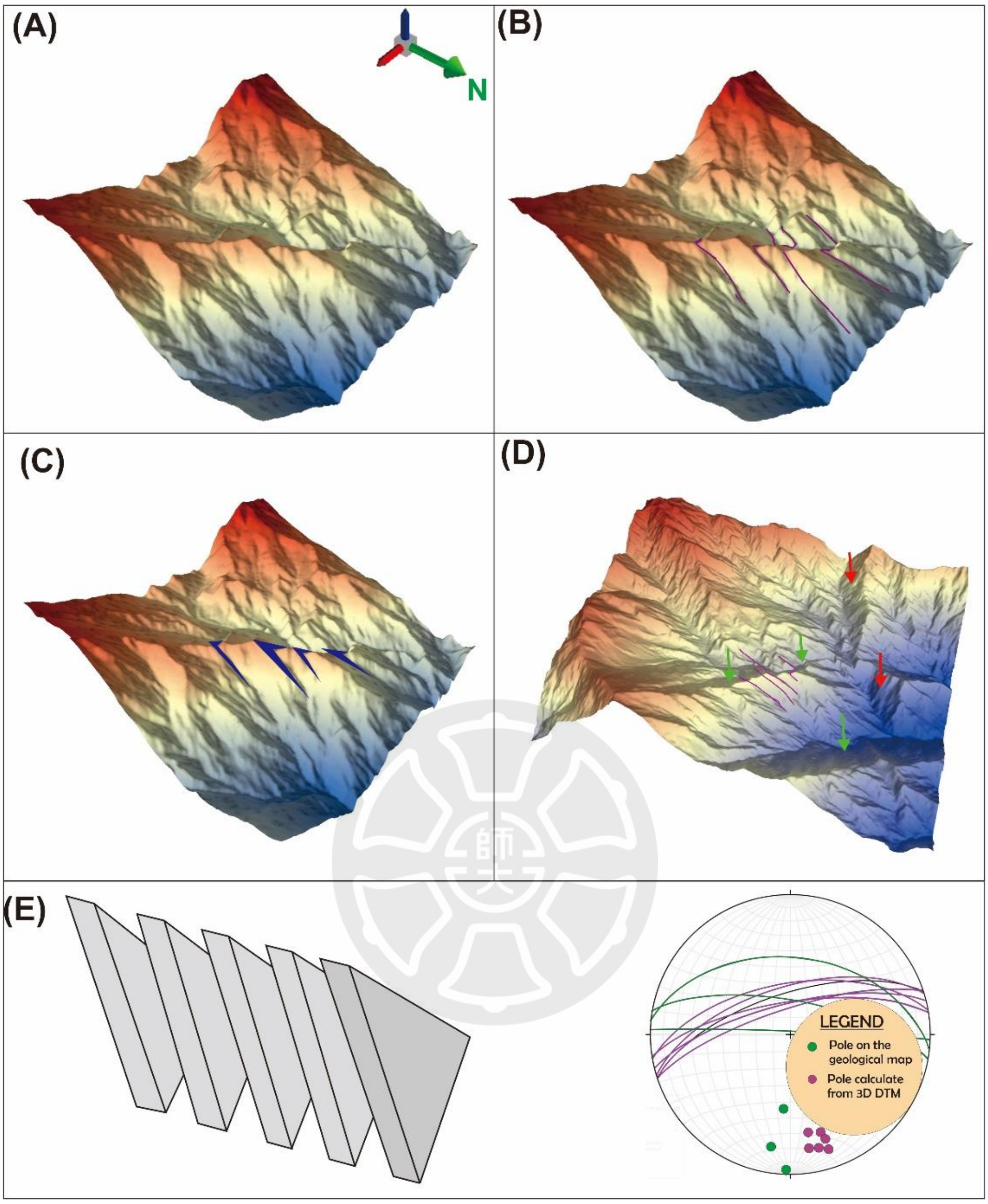

Figure 4.2: Foliation traces and foliation planes in the 3D view. (A) 5m DEM illustrated the regional foliation aspects in schist rock of the NW Heping area. (B) Purple lines were mapped as the foliation traces. (C) Regional foliation planes. (D) Cutting-relationship between foliation system and fracture system. (E) The diagram showed that each stacked triangle reflected the foliation plane and the lower hemisphere projection presents a similar attitude between foliations from DEM-derivation and foliation from fieldwork.

4.1.1.1 Domain I

The systematic parallel solid purple lines in NE-SW trending are interpreted as the trace of the foliation plane and have been traced along the gullies of the Dongao greenschist area in the 3D environment of DEM data (Fig 4.3A). Foliations are gently west-dipping with a dip angle of 48°-58° (Table 4.1). It can continually extend several hundred meters if the surface process does not modify the landform. The attitude of foliation from nearly field data (Table 4.2), which are marked by green dots (Fig 4.3A), was selected to compare with our foliation attitude calculation results. The lower hemisphere projection in Figure 4.2B illustrated that the green great circles presented the foliation attitude derived from field data, whereas the purple great circles described the foliation plane from DEM (Fig 4.2B). It shows a strong similarity of attitude between field mapping and calculation. Also, poles to the plane displayed a similar distribution of foliation in this area between field data and DEM-derivation.

In this domain, the red arrows indicated the traces of NE-SW striking fracture planes that cut the NW-SE purple foliations. According to the cutting-relationship between the fracture traces and foliation, we can distinguish fractures from foliation.

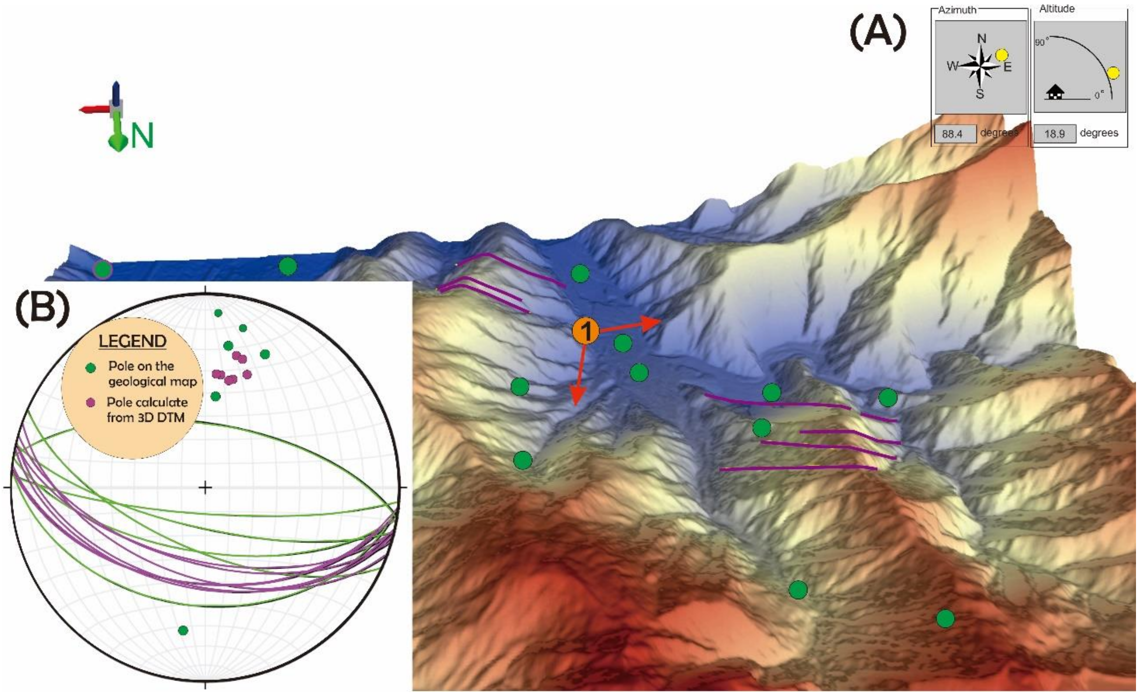

Figure 4.3: Comparison of foliation attitude between DTM-derivation and field data at the location 1. (A) The NW- SE purple lines indicated the foliation plane and the green dots referred for the existing foliation at the geological map. (B) Comparison results of foliation attitude between our interpretation from DEM (dark green dots) and field foliation data from Geological map (purple dots) in the lower hemisphere projection.

Table 4.1: The foliations attitudes calculated from the DEM data at Domain I.

No.		Strike		Dip		Long	Lat	R^2
13	N	76	W	48	W	331747	2714714	1
14	N	83	W	49	W	331641	2715032	0.99
15	N	78	W	47	W	331747	2715133	1
16	N	84	W	49	W	331904	27213	1
17	N	70	W	52	W	332842	2713772	0.98
18	N	77	W	59	W	332915	2714096	0.99
19	N	74	W	58	W	332944	2714024	0.99

Table 4.2: Foliation attitude from the geological map

No.	Dip Direction	Dip
783	009	63
785	186	39
786	189	63
820	184	79
789	193	73
787	194	64

4.1.1.2 Domain II

In the Heping area, we clearly observed the predominance of W-E striking lineaments. The representative lineament illustrated by purple, parallel lines (Fig 4.4A) supposedly indicates foliation traces located in the west flank of the ridge were cut by three distinctively fracture planes numbered by 1, 2, and 3 (Fig 4.4A). This is these fracture planes also cut across the ridges, and normally explained why we could clearly observe numerous discontinuous lineaments. Therefore, the planes cut the foliation traces, and together cut across the ridges on a large scale can consider as the fracture planes (Fig 4.4A).

Field investigations are often difficult to perceive in highly forested metamorphic terrain. Although, only two field data were documented at two locations near the river area (Fig 4.1) and simply marked by green dots in the 3D scene of Arc Sense (Fig 4.4A). However, these valuable field data gave us an opportunity in foliation attitude comparisons. The attitudes calculation of foliations from DEM derivation are closely vertical and ranged from 62° to 72° (Table 4.3), and in the comparison, they are compatible with the foliation attitudes from field data (Fig 4.4B).

N-S striking and west-dipping fractures numbered by 1, 2, and 3 (Fig 4.4A) were generally used to distinguish the foliation of metamorphic rock.

Table 4.3: The distribution of foliation attitudes calculated from DEM data of Domain II.

No.		**Strike**		**Dip**		**Long**	**Lat**	R^2
1	N	76	E	72	W	323948	2704302	0.84
2	N	72	E	66	W	323890	2704421	0.96
3	N	80	E	60	W	323806	2704525	0.95
4	N	72	E	75	W	323928	2704176	0.99
5	N	81	E	71	W	323784	2704758	0.8
6	N	73	E	62	W	325737	2705467	0.97

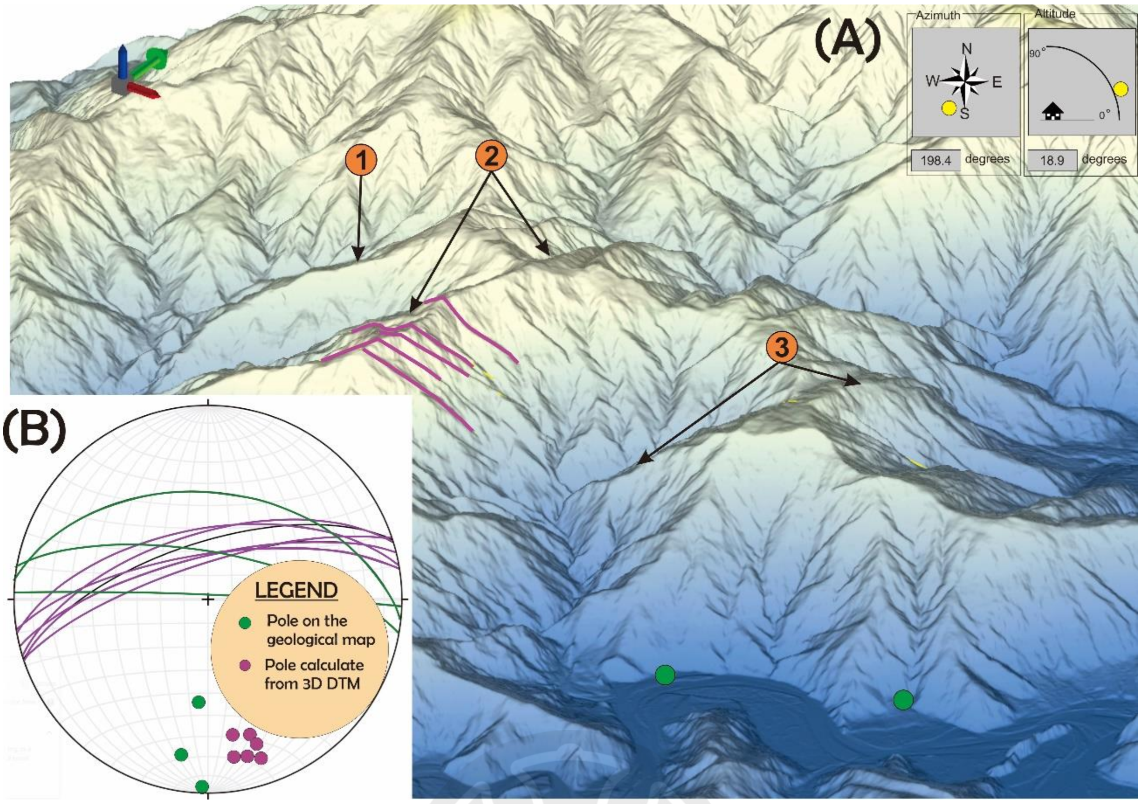

Figure 4.4: Comparison of foliation attitude between DTM-derivation and field data at the location 2. (A) The NE-SW systematic purple parallel lines were identified as the traces of foliation in the Heping area, and foliation was cut by fracture surfaces numbered by 1, 2, and 3. (B) Stereonet showed the foliation attitude determined from DEM data and field data in the geological map.

4.1.1.3 Domain III

We identified the NE-SW striking and NW dipping foliation system at location 3 where it is greenschist (Fig 2.4) near the lithological transition area between marble and greenschist. The purple lines, which are displayed in the 3D environment of Arc Sense, are illustrated for the foliation traces (Fig 4.5A). The similarity of attitudes is observed in the lower hemisphere (Fig 4.5B).

The dip angle of foliation planes with ranged from 41°-52° was cut by one fracture plane. This fracture plane is composed of three planar surfaces numbered by 1, 2, and 3 and has attitude in W-E striking and south-dipping (Fig 4.5A). The fracture planes with strikes in NW-SE in this area were denoted by yellow arrows (Fig 4.5A). Those fracture planes are considered as the different fracture systems from previous W-E striking fracture planes. It could denote disparate deformation phases with the W-E fracture system due to the evolution of the tectonic setting.

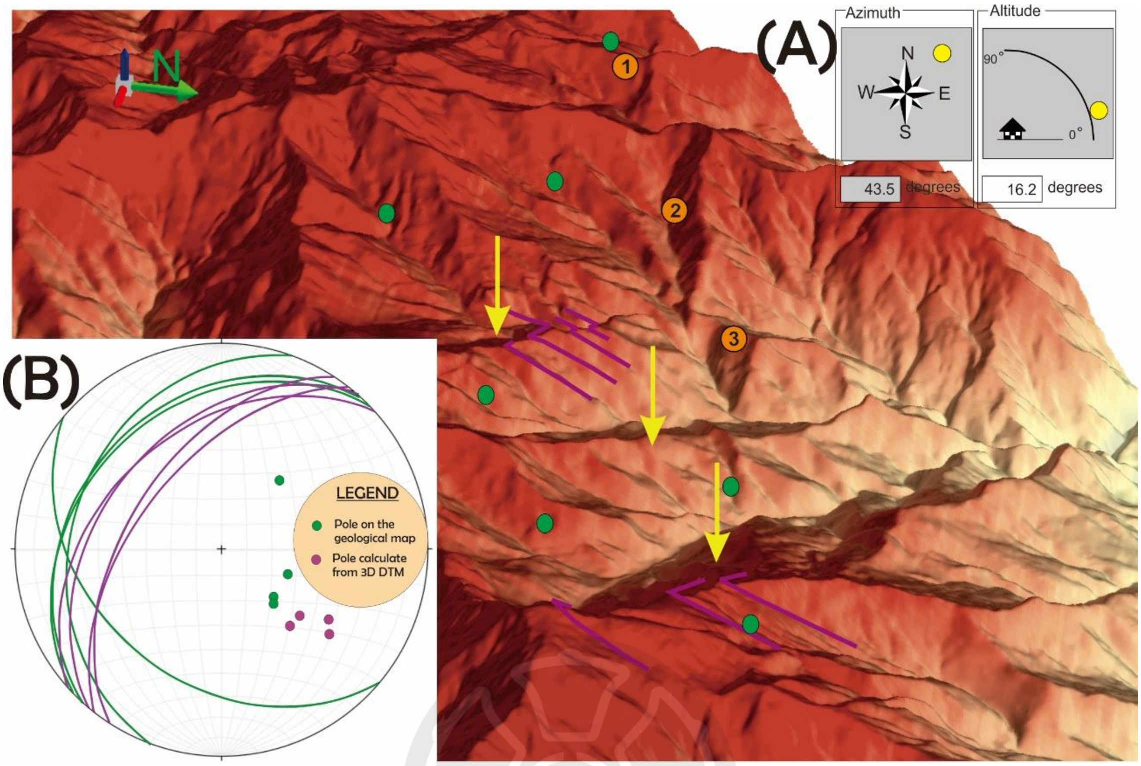

Figure 4.5: Comparison of foliation attitude between DTM-derivation and field data at the location 3. (A) The regional foliation with NW – SE striking (purple linear) was cut by a NE-SW trending fracture plane, which was distinguished by three planar planes numbered by 1, 2 and 3. (B) The great circle in stereonet presented a similar strike and dip angle of regional foliation calculated from DEM and the attitude of foliation in geological map.

Table 4.4: The distribution of foliation attitudes calculated from DEM data of Domain III.

No.	Strike			Dip		Long	Lat	R2
1	N	48	E	41	W	308956	2685017	0.99
2	N	49	E	41	W	309033	2684946	0.98
3	N	33	E	52	W	309283	2684879	0.92
4	N	38	E	56	W	309182	2684922	0.98

Table 4.5: The distribution foliation attitudes of field data analyzed from the geological map.

No.	Dip Direction	Dip	Long	Lat
386	290	28	308413	2684239
387	310	36	307750	2684787
382	316	30	310948	2686848
383	312	28	310235	2686456

4.1.2 Fracture plane mapping

4.1.2.1 Interpretation of fracture plane

The surface fracture set, in combination with the ductile foliation, define the regional morphotectonic lineament pattern. Therefore, Florinsky (2016) dedicated that the mapping morphological lineaments can be used to recognize geologic structures, especially the lineaments located along the straight river bank, across the ridge, etc., are able to present the plane of the fracture. The planes, when breaking the slope or scarp during the action of the tectonic or non-tectonic process supposedly are planar (Fig 4.6A) and exposed on the surface. In a 2D map, lineaments located along the plane supposedly is "traces" (Fig 4.6B). Tracking the "traces" in the 3D environment of Arc Sense can recognize the fracture plane and even evaluate the contribution and development of the fracture system in the 3D model (Figure 4.6C). Along lineaments, because the supposed fractures are represented the sensitive and risky area with the erosional surface process, the topography is easy modification and forms the gullies topography. Therefore, tectonic lineaments along the gullies structure implied the fracture planes. The paths of gullies are significant features to recognize the neotectonics fracture (Chen et al., 2016).

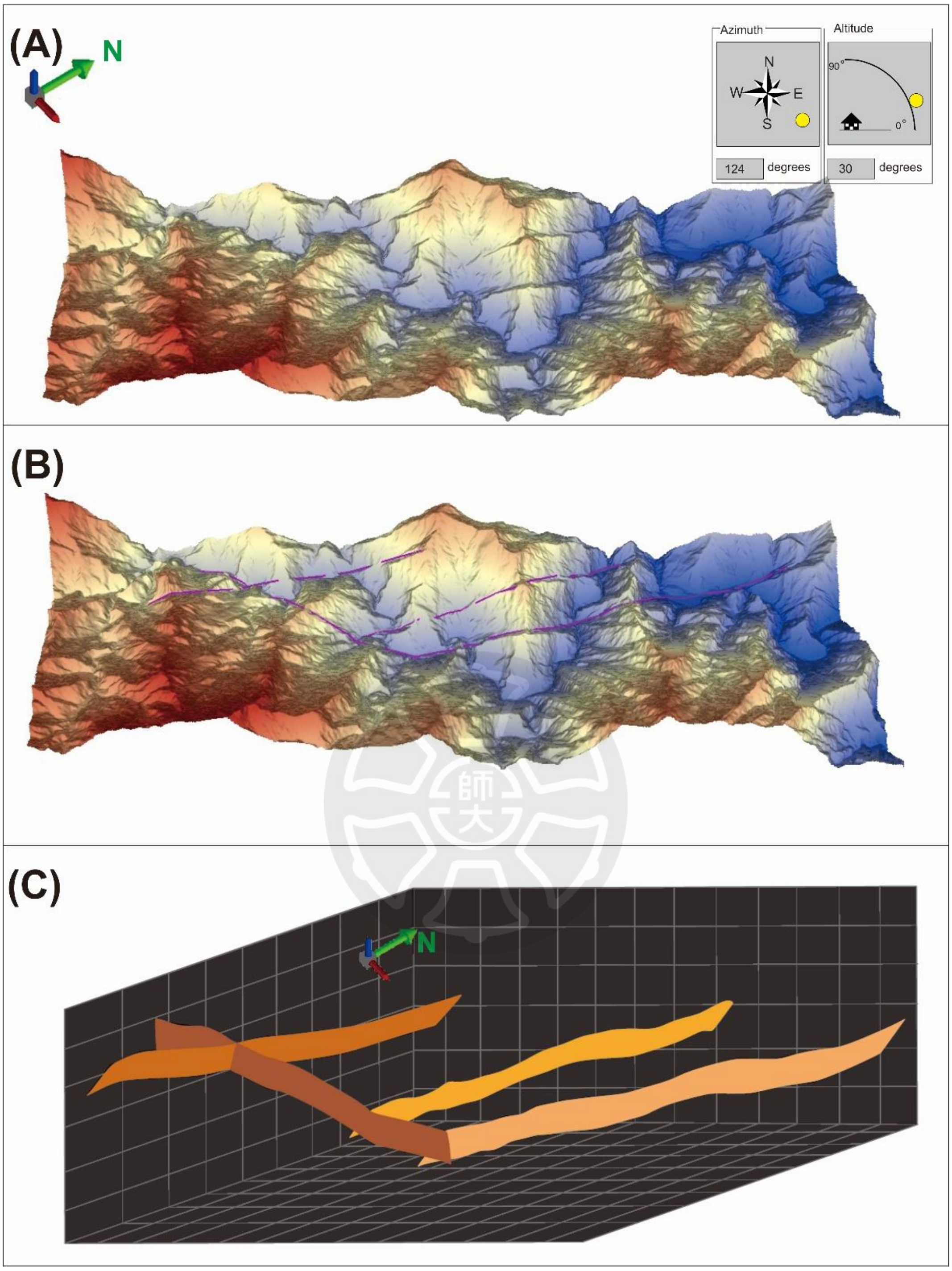

Figure 4.6: Characteristics of the fracture plane in the 3D view of Arc Sense. (A) The footprint of the fracture plane on the surface significantly correlates with the distribution of lineaments. (B) Four lineaments (purple lines) along with the fracture footprint. (C) Four fracture planes are mapped based on the fracture trace in 3D view.

4.1.2.2 DEM-derived fracture plane

In DEM mapping, 187 fracture planes were identified, mapped, and calculated their attitudes in three different domains. In the Domain I, 50 fracture planes was recognized with the orientation dominated in ENE-WSW striking, and the mean fracture plane was evaluated and displayed by the ENE-WSW striking great black circle in the lower hemisphere projection. 65 & 72 fractures in Domains II and III were recognized, respectively. The attitudes of fracture planes at Domain II were gently clockwise rotated to NE-SW compared with the attitude of N-S striking of fracture in Domain III. The evidence in the lower hemisphere illustrated 30° differences in the strike of mean fracture attitude of Domain II and III (Fig 4.7).

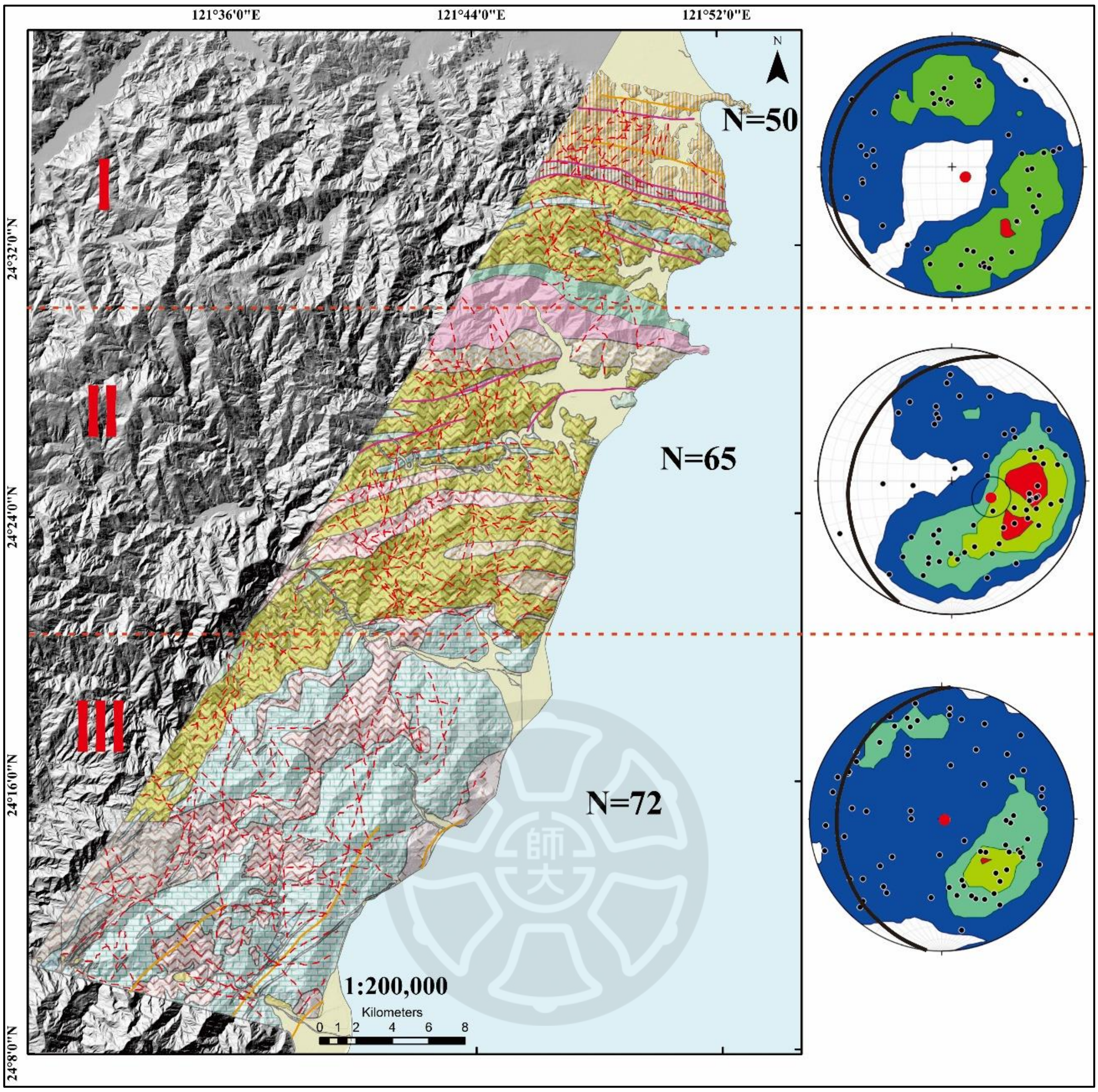

Figure 4.7: Spatial distribution of surface fracture planes in DEM data. 187 fracture planes were identified, mapped, and calculated their attitude in three different domains of NE Taiwan via used the 5m DEM data. 50, 65, and 72 fractures were mapped in Domain I, II, and III, respectively. The lower hemisphere projection represented the distribution of the fracture plane by the contour map. The mean fracture attitude was calculated and displayed by the mean pole (red dot) and the great mean circle (black curve lines) in different domains.

4.1.2.3 Restriction of Selected Fracture Plane

The strike and dip of DEM-derived fracture planes are evaluated from each measurement triangle. Triangle selection in the study area is based on the following restrictions for better results of representative fracture plane results.

Reliability of regression calculation

During calculating the fracture attitude, the regression reliability (R^2) values of the measured triangle can also be determined. Yeh et al. (2014) indicated that the selected triangles with high R^2 have the goodness of fit for the regression plane. Therefore, the fracture planes were classified into ten groups based on different R^2 values (Fig 4.8). The dark green to light green lines represented the fracture plane within lower R^2 (0.03-0.4), the yellow to orange line represented fracture planes of middle R^2 (0.41-0.8), fracture planes of high R^2 (0.81-1) values were indicated by red lines. Totally, in three domains, 120 measurement triangles with $R^2 > 0.85$ based on the above restrictions are used for the instability analysis.

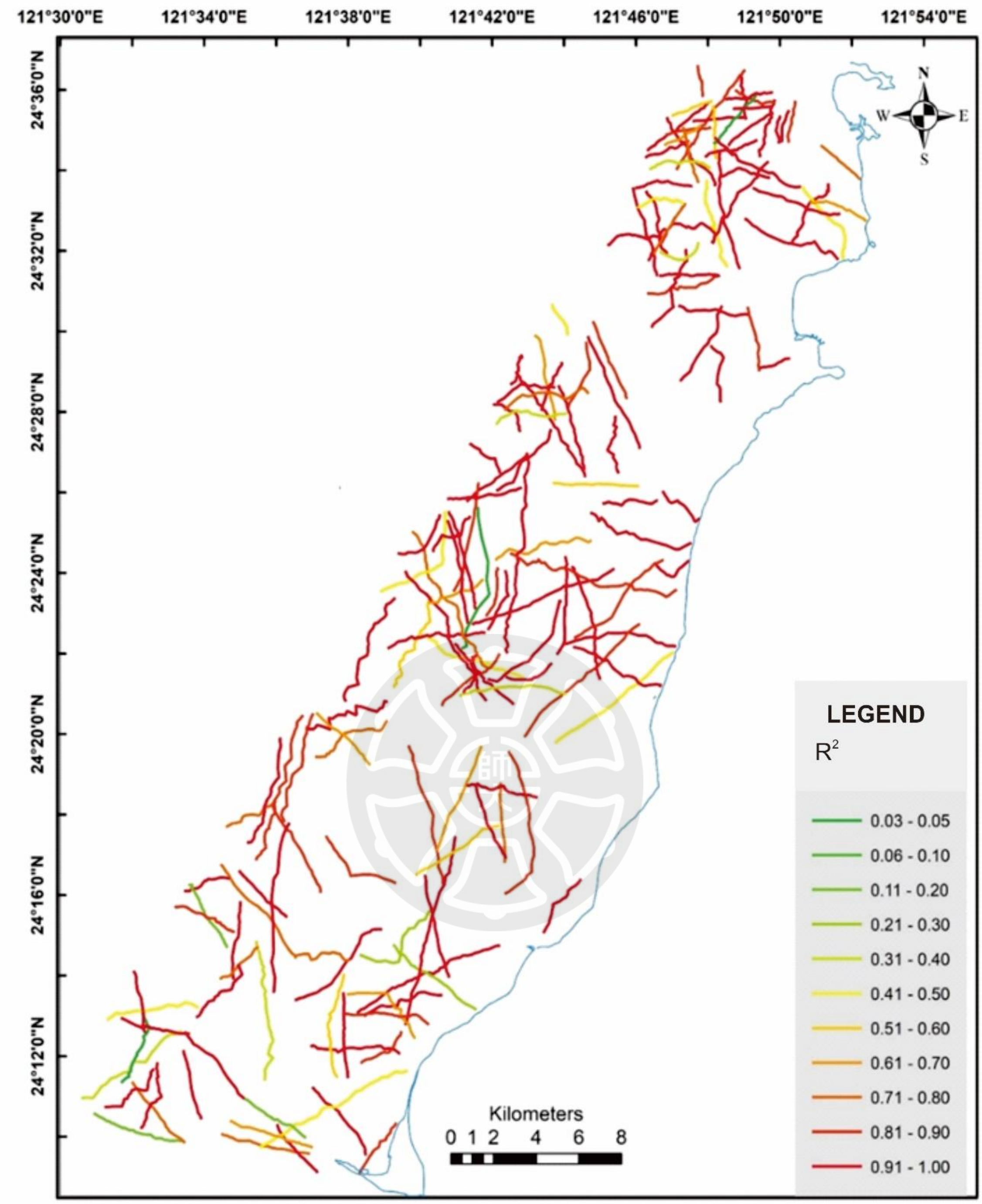

Figure 4.8: Classification of the fracture planes based on R^2 value. 120 selected fracture planes (red lines) are reasonable for the input database of tendency analysis.

Subsurface Rupture Length

Furthermore, we supposed that the fracture patterns in NE Taiwan correlated with earthquakes events. The known magnitude earthquakes events conducted the fault ruptures (Well and Coopersmith., 1994). Therefore, the rupture area of the fracture is an important key to evaluate the correlation of fracture pattern with earthquake events. And, the rupture parameters commonly including rupture length and fracture width that they can be estimated in the spatial.

The observational data from field studies of faults as well as theoretical studies of seismic moment suggest that earthquakes magnitude should correlate with the amount of rupture area along the causative faults (Well and Coopersmith., 1994).

The subsurface source can obtain rupture length and rupture area. The magnitude (M) of earthquake events is positively correlated with the fracture rupture length (Fig 4.9). Well and Coppersmith (1994) concluded that the smallest earthquake events with M=4 could be conducted 1km rupture length along the fault and 600km rupture length can be created by the earthquake events in M > 8.

In our study, the horizontal distance (RLD) of fracture planes were calculated from the first and end vertices of fracture coordinate. The fracture rupture lengths are in the range of 1-9 kilometers (Fig 4.10). The focal mechanism in NE Taiwan (Wu et al., 2008) provides the seismic magnitude (M) is in the range of 2.5-6.5 of different seismic fault types. We categorized seismic fault types from focal mechanism data by rake angles. Therefore, the distribution of fracture rupture length corresponded with the magnitude size of single EQ events should be in range 1-20km.

Finally, we determined 120 fracture planes based on the restriction of R^2 and RLD, which are illustrated by the red lines in Fig. 4.11. Those fractures will be used to test the hypothesis that whether the fracture sequences are correlated with the stress evolution in NE Taiwan.

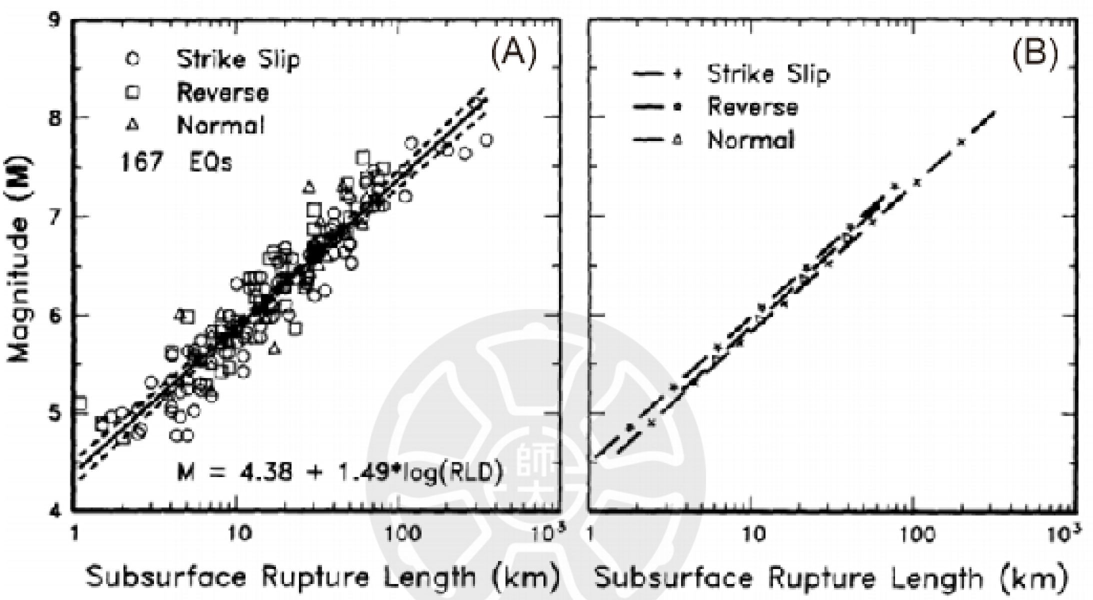

Figure 4.9: Relationship of subsurface rupture length with the magnitude of earthquake events. (A) The regression of average subsurface rupture length with earthquake magnitude (M) for all fault types. (B) There is no distinct difference in the regression line (Well and Coppersmith, 1994).

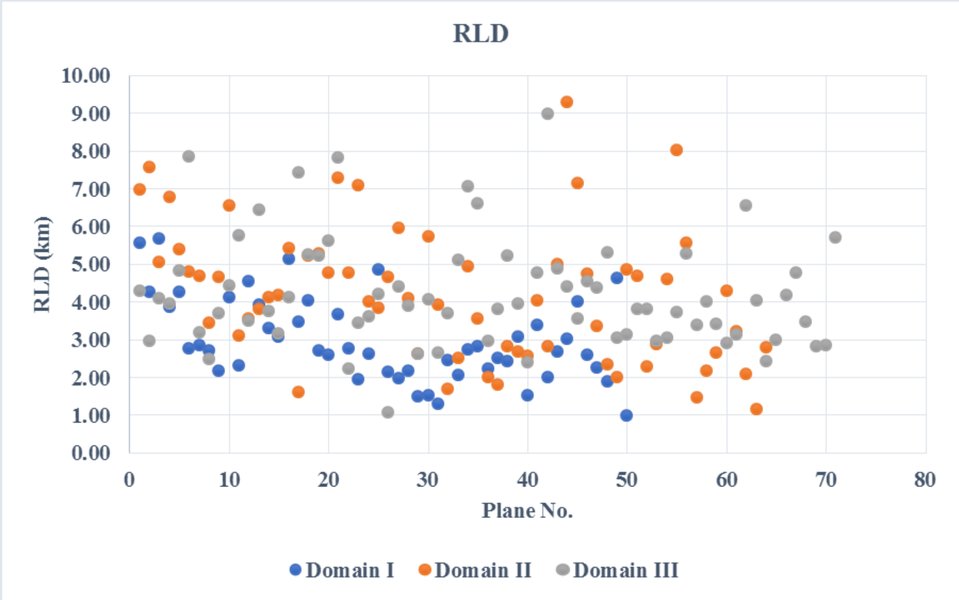

Figure 4.10: Distribution of subsurface rupture length of fracture planes in study area.

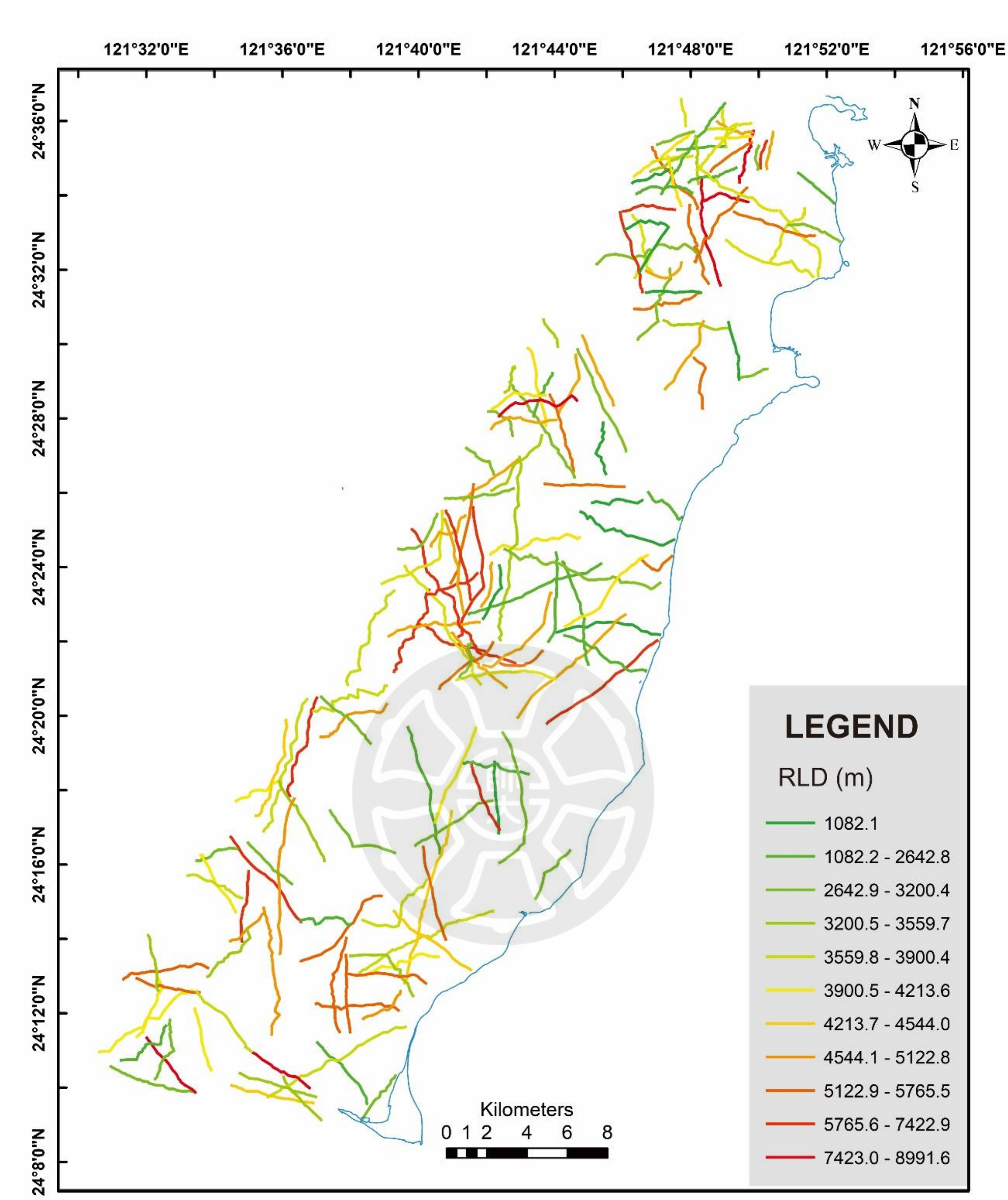

Figure 4.11: Classification of fracture planes based on the horizontal distance.

4.2 Analysis result of focal mechanism data

4.2.1 Distribution of focal mechanism.

The distribution of several focal mechanism clusters can be identified and illustrated in the tectonic evolution of NE Taiwan (Fig 4.12). The reverse faulting focal mechanism (1) is dominated by the NNE-SSW trending and is positioned along the coastal line from the Taroko to the Hualien. In the transition area between Ilan and Hualien, two clusters of strike-slip focal mechanisms (3) and (4) were recognized. The NNE-SSW trending strike-slip focal mechanism cluster (3) is inclined ENE-WSW trending cluster near the Heping area (Domain II). ENE-WSW trending the focal mechanism cluster followed the orientation of the Ryukyu volcanic arc. This cluster could represent the transition area between the collision and the subduction system. Other strike-slip focal mechanism clusters extend NNE-SSW trending from Nanao Plain to southern Ilan Plain (Domain I). The normal faulting focal mechanisms are distributed in two different clusters in this area. A small cluster of normal faulting (5) was represented in the south of Okinawa Trough, whereas NE-SW normal faulting trending (2) was presented in the eastern flank of the Central Range. Two cross-sections (NE-SW trending AA' profile and ENE-WSW trending BB' profiles) are established to analyze the distribution of focal mechanism, and the location of profiles was shown in Figure 4.12. In Figure 4.13, N15°E striking-profile AA' presented the clearly various distribution of focal mechanisms not only from south to the north but also from shallower to deeper part of the crust. Three determined focal mechanism clusters are placed along this cross-section (Fig 4.13). In the south, the normal focal mechanism clusters (2) are located at about 5-7.5km and overlapped with thrust faulting clusters (1).

The thrust faulting cluster extends farther to the north and becomes deeper, suggesting the seismic belt (Huang et al., 2012). Along this profile, the arbitrary distribution of the strike-slip faulting events and normal faulting events conspicuously developed at a distance of 25 km. The strike-slip focal mechanism events are particularly dominant in comparison with normal faulting events. Especially, one sub-vertical strike-slip focal mechanism cluster (3) was observed as the distancing at 45-50 km, which is considered as mostly left-lateral strike-slip events (Huang et al., 2012). Previous seismic investigation (Ku et al., 2009) examined this cluster may extend further seaward, which is correlated with this event in Figure 4.13.

In Figure 4.15, along with N80°E striking profile BB’, three recognizable focal mechanism clusters were observed. At 20 km distance, the distinct thrust faulting events (6) (Fig.4.14) was regarded under the eastern flank of Central Range (Huang et al., 2012). The other cluster thrust faulting (1) is located primary shallower than 12.5 km deep in the eastern part of this profile. In the western part of this profile, a west-dipping the normal faulting cluster (2) is found in the shallow depth of about 5-10 km.

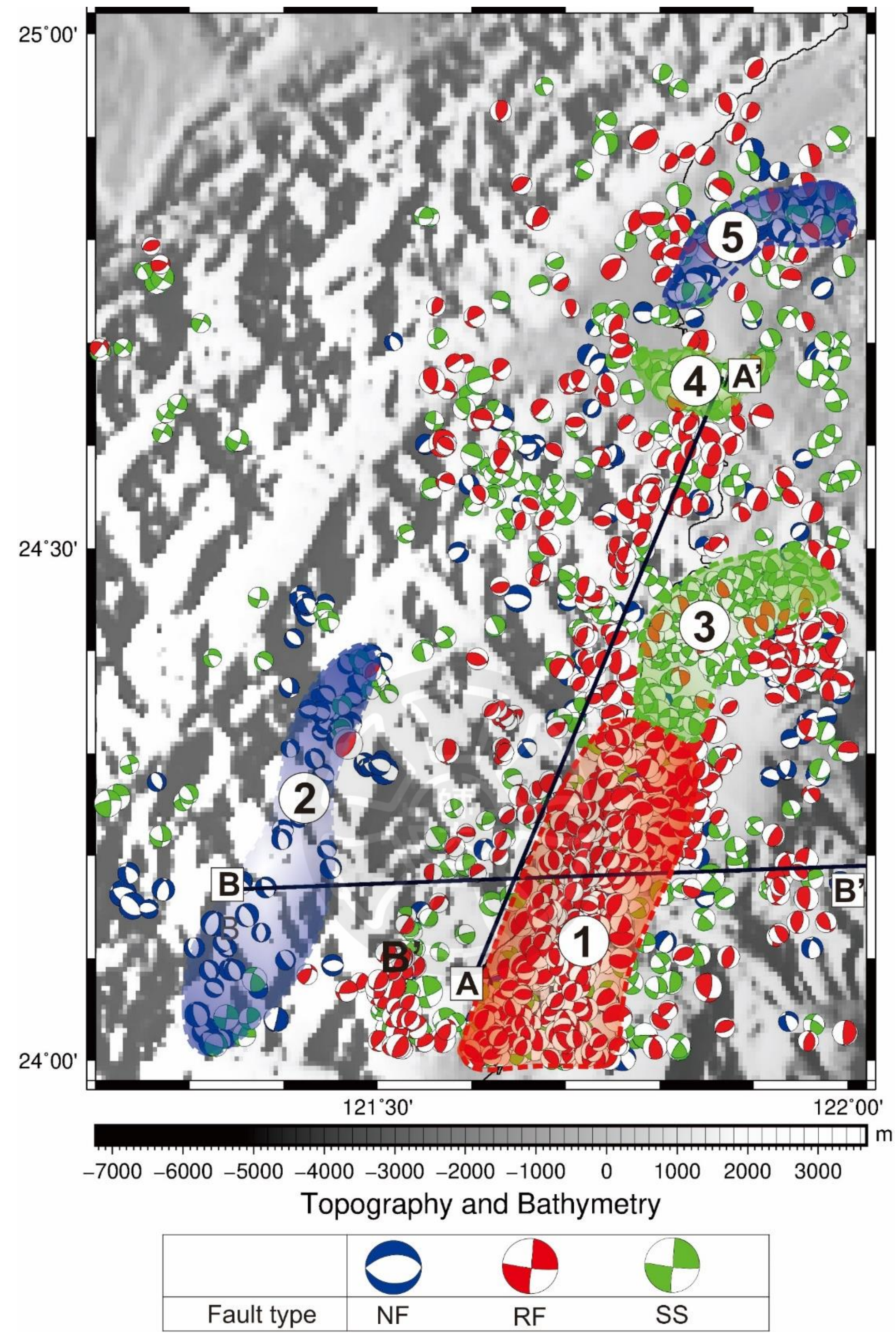

Figure 4.12: Distribution of focal mechanism of NE Taiwan (M>2). Normal, thrust, and strike-slip faulting are categorized by the rake angle (Huang et al., 2012) (thrust, 45° to 135°; normal, - 45° to - 135°, others) and presented by blue, red, and green. Lines A-A' and B-B' are the locations of the cross-section.

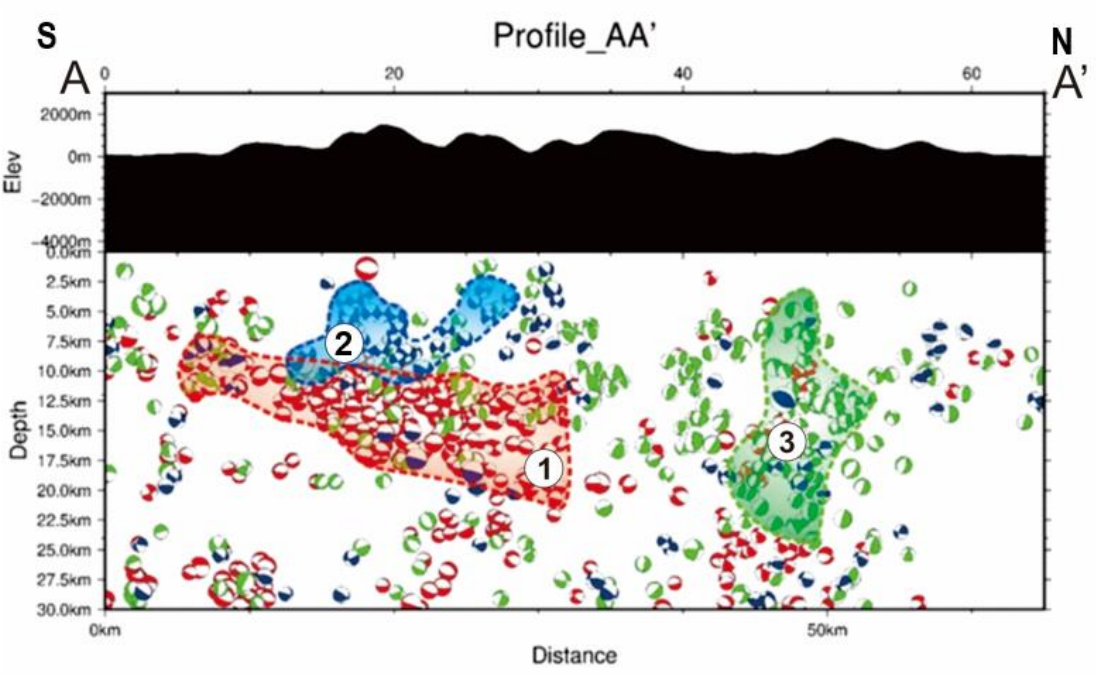

Figure 4.13: Focal mechanism data distribution along cross-section AA'. In the south, the normal faulting cluster (2) dominated at about 5-10 km and overlapped with the thrust faulting cluster (1). The thrust faulting cluster extends farther to the north and becomes deeper at about 7.5-20 km. The strike-slip faulting cluster (3) is located in the northern area.

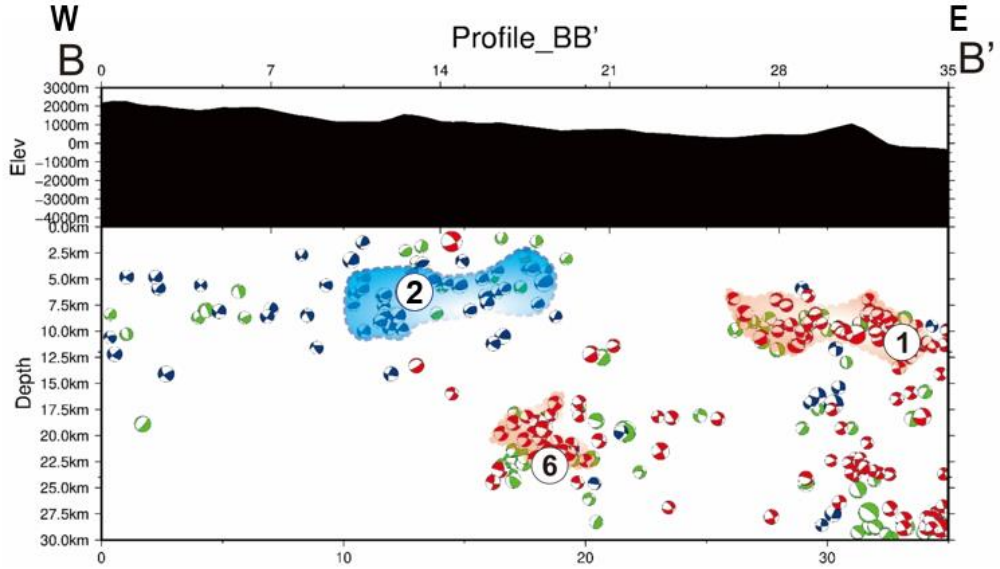

Figure 4.14: Focal mechanism distribution of B-B' cross-section. Two distinct clusters of focal mechanism events are composed of a thrust-faulting cluster in the west (6) and thrust faulting cluster in the east (1) at shallow depth. The normal faulting cluster (2) presented the normal stress regime under the western flank of CeR.

4.2.2 Stress inversion

164 focal mechanisms with a magnitude larger than 2.5 are collected to obtain the seismotectonic stress tensor of three domains by solving the inversion solution with code (Vavryčuk, 2014). The focal mechanism data inside each rectangle are applied to evaluate the inversion results of each domain (Fig 4.15). Thus, the result of stress inversion analysis for three different domains was demonstrated in Figure 4.17. and it was conducted shallower than 10 km depth due to the exhumation rate of this area (Liu, 1982; Hsu et al., 2016; Chen et al., 2016) (Fig 4.16). At least four earthquake events are required to calculate four unknown parameters of the stress tensor, including three

directions of principal stress and stress ratio (R). The stress regime along NE Taiwan coastline is established from focal mechanism data (Fig 4.17).

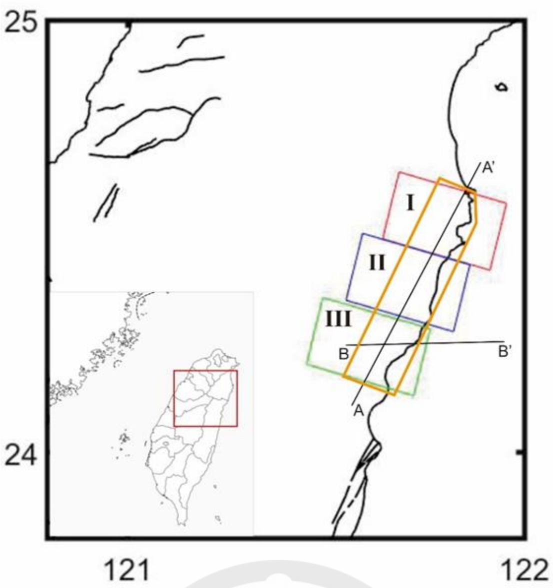

Figure 4.15: Map of stress domains in the study. (red, blue, green rectangles are noted for the Domain I, II, III, respectively), the orange polygonal indicated study area. A-A' and B-B' are the cross-sections.

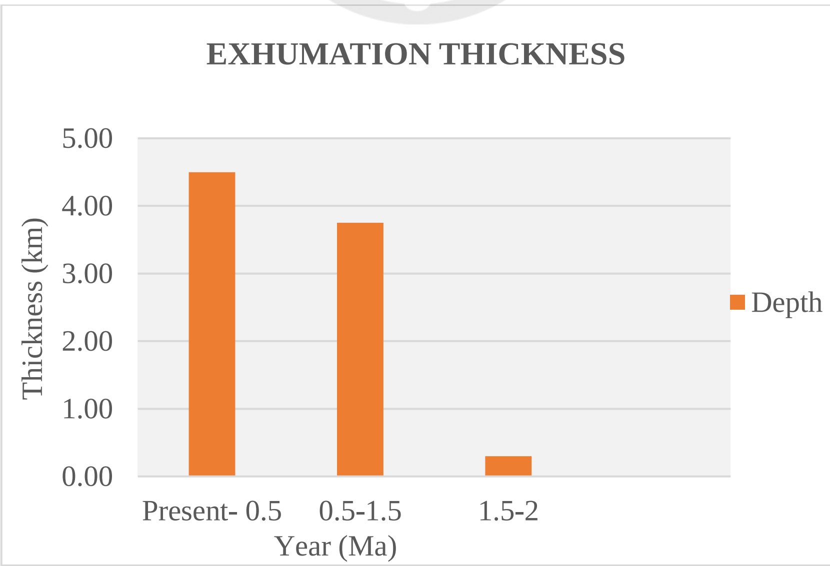

Figure 4.16: Exhumation rate of NE Taiwan area

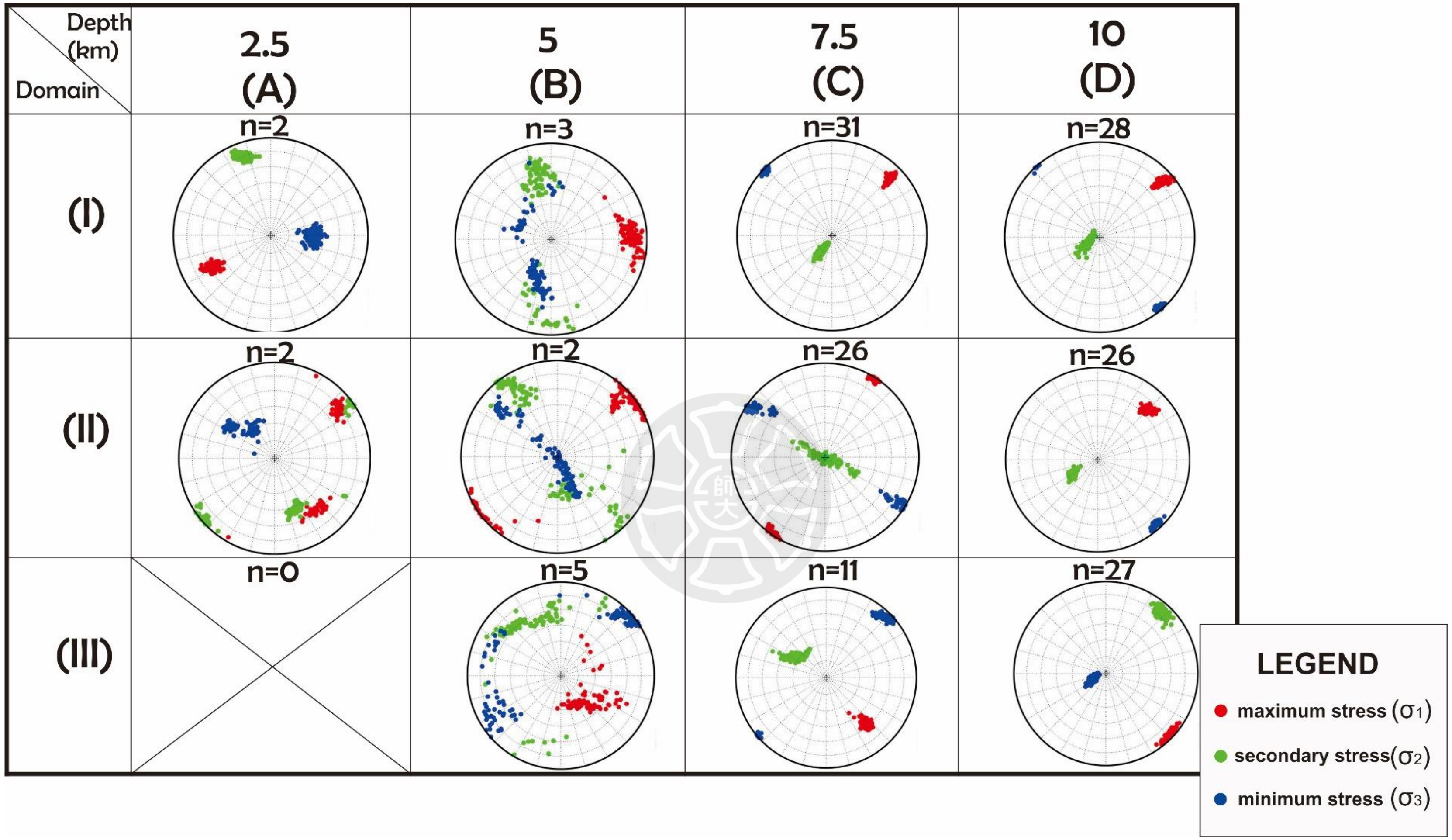

Figure 4.17: Stress inversion results with different depths. In each Domain, σ1, σ2, σ3 are maximum, intermediate, and minimum principal stress and are presented by red, green, and blue circles, respectively. n is earthquake event.

In this figure, at the lower crust, no reliable stress state is available in Domains I, II, and III due to the lack of the focal mechanism data. Only two or three focal mechanisms are obtained from earthquake events at 5 km of Domain I and II, whereas no earthquakes event happened in the domain III. After examining five earthquake events at 5 km depth, the stress inversion results demonstrated a normal faulting stress regime, but the stress state is unstable because σ_3 and σ_2 orientation are slightly permutation (Fig 4.17). Hence, only stress states ranged from 7.5-10 km depth of each domain are reasonable for operating fracture instability analysis (Fig 4.18).

In the middle crust at about 7.5-10 km of Domain I and II, the prevailed strike-slip faulting regime was observed. The compression orientation was detected in NE-SW trending, while the tensile orientation is NW-SE. However, at Domain III, the compression turned to NW-SE orientation, and the tensile axis of stress state was NE-SW trending. Especially, the stress state shifted at 7.5 km from the strike-slip faulting with sub-vertical σ_2 to thrust faulting stress regime at 10 km. The orientation of three principal stress states and the standard deviation was addressed in Table 4.6.

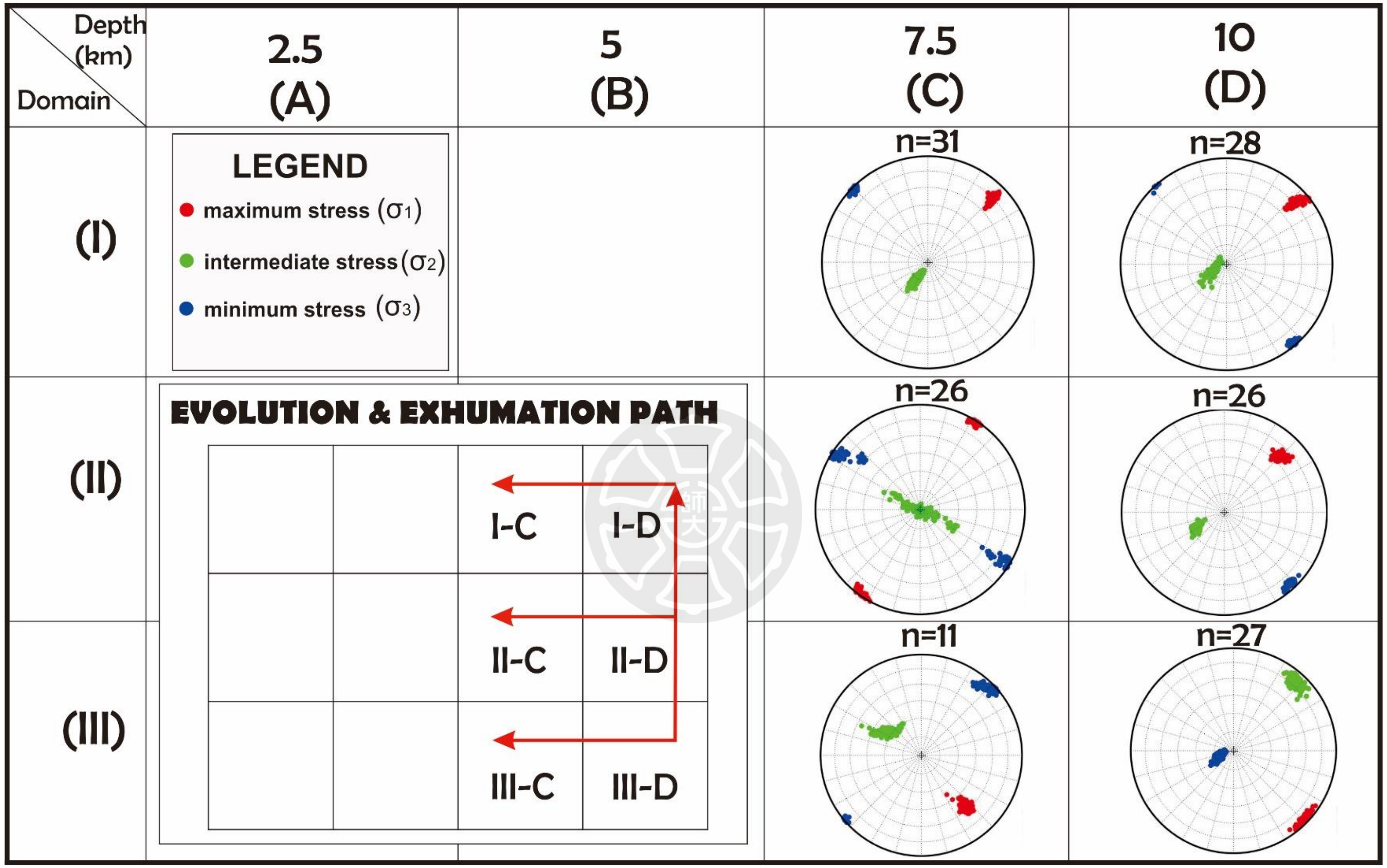

Figure 4.18: The reasonable stress state of each domain for fracture instability investigation. And, the evolution and exhumation path of the stress state might be indicated the variation of fracture system from south to north of NE Taiwan.

Table 4.6: The principal stress orientation and standard deviation.

Principal stress / Domain	σ_1 Azimuth/Plunge	σ_2 Azimuth/Plunge	σ_3 Azimuth/Plunge
III-D	135.4/3.8 ± 7.9	44.2/14 ±10.8	239.8/75.4 ± 9.6
III-C	139.4/29 ±15.6	309.5/60.5 ±20.43	47.0/4.2 ±13.1
II-D	46.8/26.3 ±11.2	241.8/6.28 ±10.9	139.8/6.07 ± 8.1
II-C	218.4/8.23 ± 15.4	114.2/59.5 ± 60.4	313/29.1 ± 59.8
I-D	49.5/9.9 ± 15.4	249.1/79.4 ± 15.6	140.1/3.46 ±7.42
I-C	46.1/20.2 ± 15.7	217.5/69.6 ±15.7	315/2.8 ± 3.5

4.3 Fracture Instability

4.3.1 Threshold value of fault instabilities

4.3.1.1 Domain III

The calculation of the threshold value of fault instabilities at Domain III is 0.8. Because at 10 km, the reasonable fault plane with the instability large or equal 0.8 is pretty dominant, even the quality index of focal mechanism data (Qfp) of mainly reverse faults (RF) is below 1 (Fig 4.19B). Furthermore, the normal faults (NF) possessed the instability over 0.8 are mainly distributed at 7.5 km, as well (Fig 4.19A). Therefore, we supposed that fault planes at Domain III are more unstable if the instability larger or equal to 0.8.

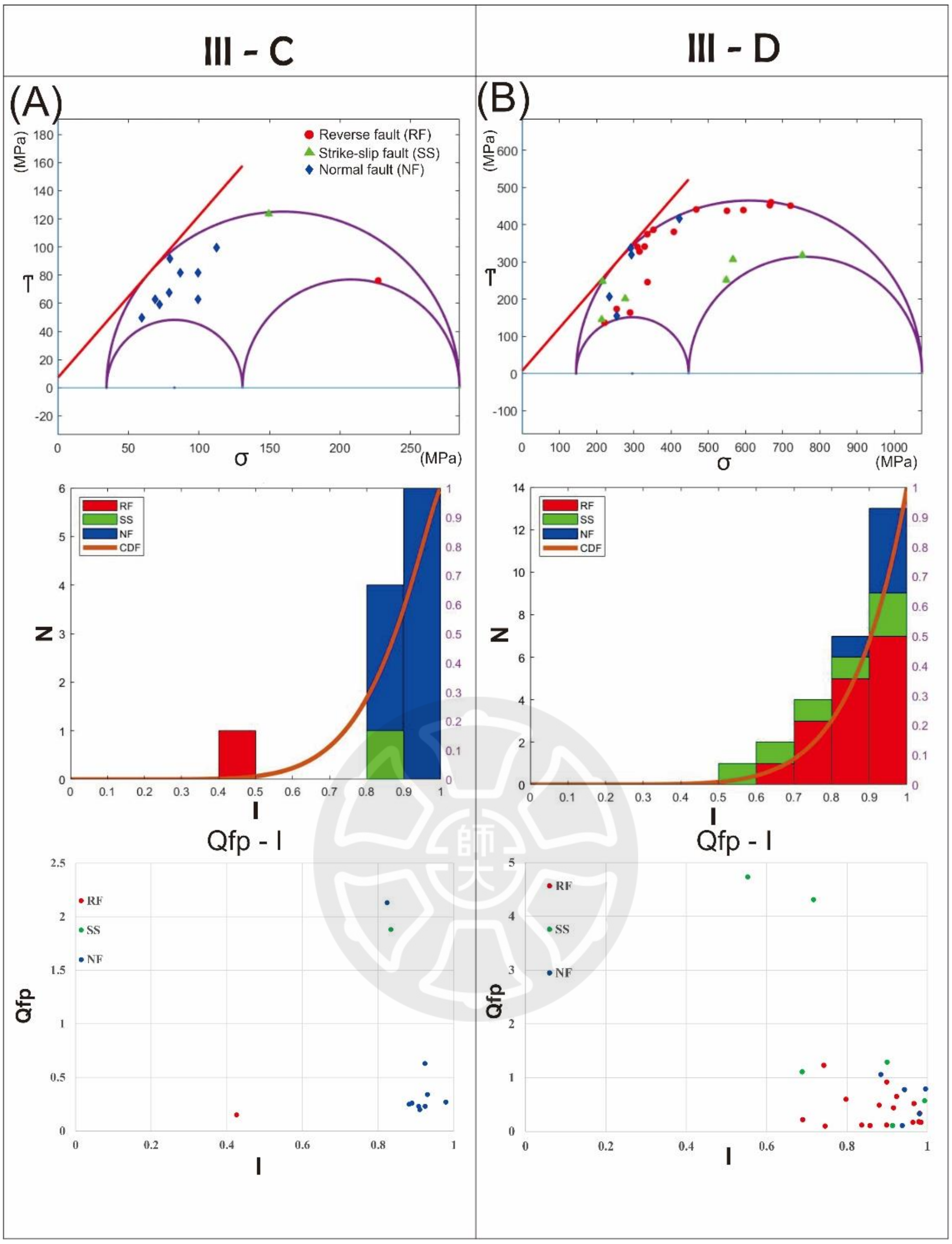

Figure 4.19: The threshold of fault instability at Domain III. Morh's diagram and Mohr-Coulomb failure criterion (red line) defined fault instability, Cumulative Distribution Function (CDF), and the distribution between fault instabilities and Qfp of distinct fault types, respectively, at different depth of Domain III. A. At 7.5 km, B. At 10km. N fault plane number; Qfp: qualify index of focal mechanism (Qfp =0 no constraint, Qfp>1 good solution).

4.3.1.2 Domain II

The dispersed instabilities of fault plane in Mohr's diagrams and Qfp-I diagrams have driven the uncertainly of identifying the instability threshold of this domain. However, at 10 km, focusing on the CDF of the mainly strike-slip faults (SS) (Fig 4.20B), the instabilities are tightly higher than 0.8 because it dominated 45% of focal planes. And, the minority of NF and RF with the low instabilities and Qfp or even high Qfp is unacceptable. Thus, 0.8 is the instability threshold to evaluate the unstable surface fracture at Domain II.

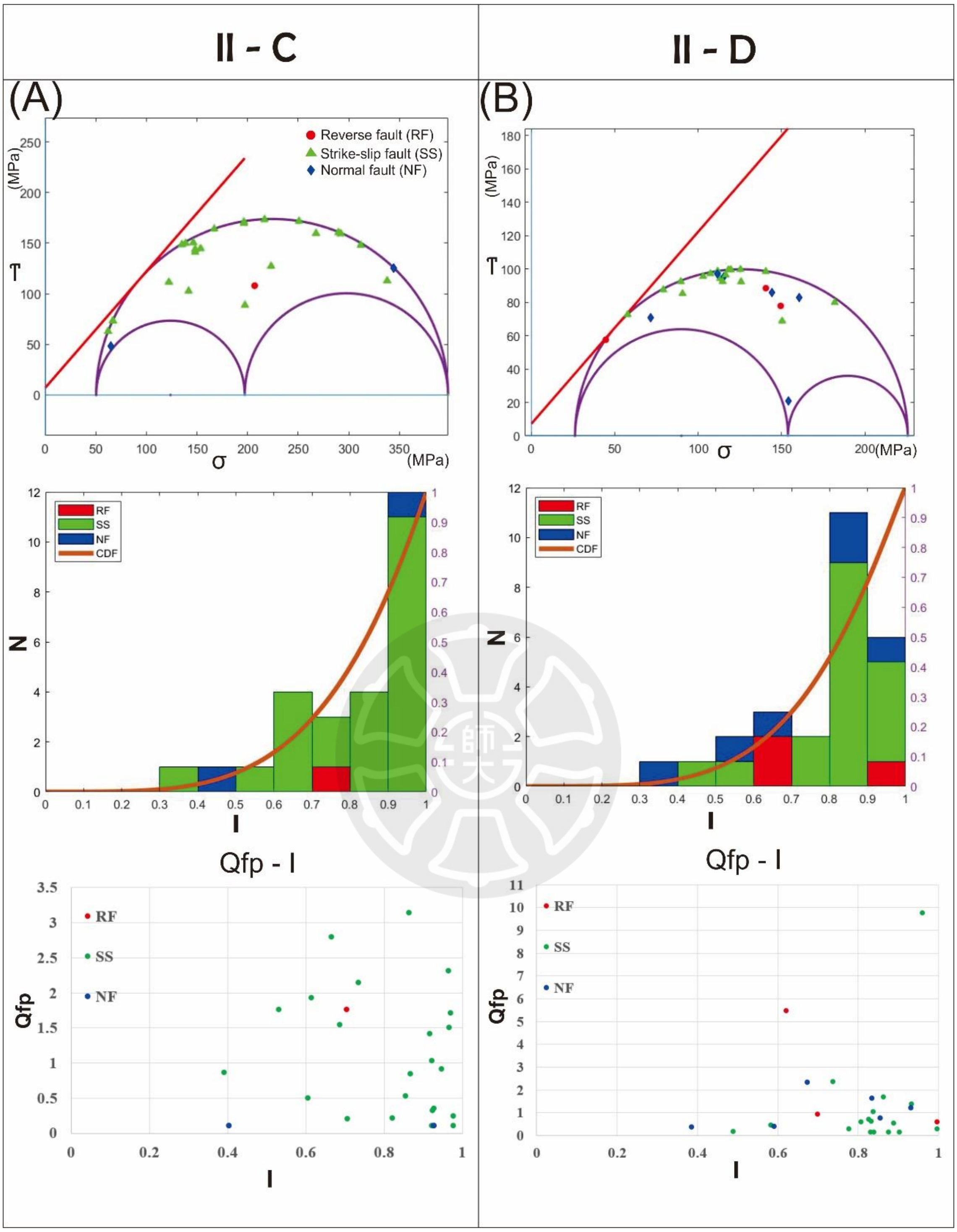

Figure 4.20: The threshold of fault instability at Domain II. Mohr's diagram, CDF, and the distribution between fault instabilities and Qfp (Qfp-I) of distinct fault types, respectively, at different depth of Domain II. A. At 7.5 km, B. At 10km.

4.3.1.3 Domain I

In similar, at 10 km depth, we pick up the threshold of fault instability is 0.6 because the dominant SS fault planes have the instability large than 0.6, and it has mainly instability values with acceptable Qfp values large than 0.6 (Fig 4.21B). At 7.5 km, the instability value of fault planes is clearly higher than the deeper part and approximately larger than 0.7 (Fig 4.21A). Thus, the fracture planes at I-C are unstable if the instabilities larger or equal 0.7.

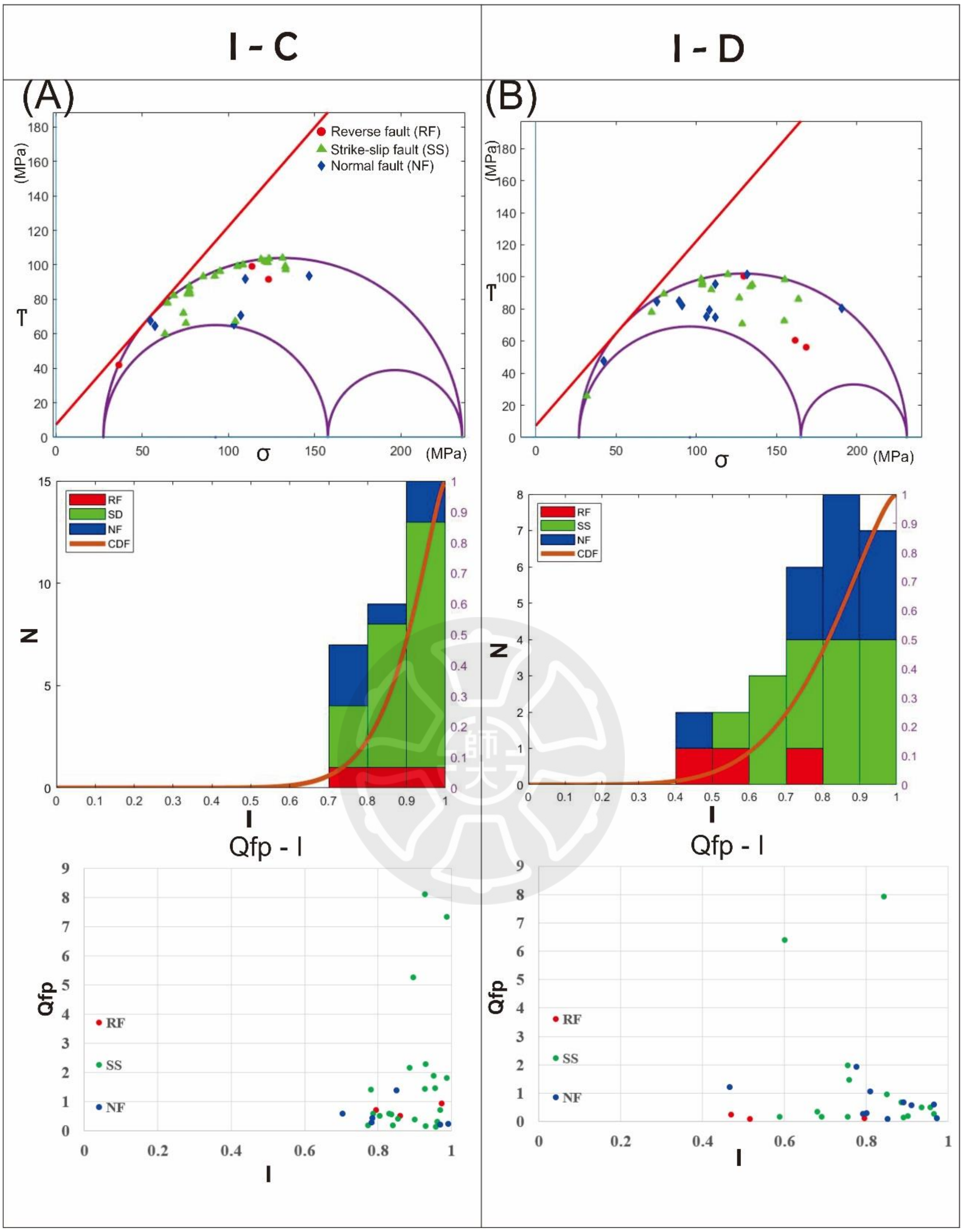

Figure 4.21: The threshold of fault instability at Domain I. Mohr's diagram, Cumulative Distribution Function (CDF), and the relationship of fault instabilities and Qfp (CI-Qfp) of distinct fault types, respectively, at different depth of Domain I. A. At 7.5 km, B. At 10km.

4.3.1.4 Threshold values of fracture instability

According to the threshold value of fault plane instabilities, which were addressed at section 4.3.1, we have demonstrated the distribution of threshold value of surface fracture instability as the table below:

Table 4.7: Threshold values of surface fracture instability examination.

	Domain I	**Domain II**	**Domain III**
C	**0.78**	**0.8**	**0.8**
D	**0.65**	**0.8**	**0.8**

4.3.2 Evolution of fracture system in NE Taiwan

120 surface fractures, which identified from DEM data, were calculated the instability and evaluated the distribution under the influences of the stress evolution from reverse faulting stress regime in the south (Domain III) to strike-slip faulting regime in the north (Domain I) along with NE Taiwan. The introduction of the evolution and exhumation path of the stress regime was mentioned in Fig 4.17 of section 4.2.2. Additionally, the instability computation of surface fractures depends on different depths with reliable stress regimes. The unstable surface fracture was evaluated by comparing their instabilities values with the estimated threshold values in table 4.7. Instability thresholds were calculated from the instability investigation of seismic faults from the focal mechanism data of Taiwan (1991-2015). The instability computation of 120 surface fractures can be assessed by the proposed stress field with depth and fracture attitudes (Fig 4.22).

Figure 4.22 shows our classification results of unstable surface fractures in the evolution of stress regimes of the study area. We analyzed the results of nucleated fracture planes formed by the evolution & exhumation path (Fig 4.18).

After calculation, we obtained 46 unstable fractures planes, which were produced by the stress field in III-D, and these planes were distributed in three domains (Fig 4.22F). After removing 46 (39%) risky planes under the III-D cell, 17 (14%) new unstable fractures caused by the strike-slip faulting regime are recognized under the stress state of cell III-C (Fig 4.22E). 36 (30%) planes suspected to be unstable planes under the stress of II-D and reverse faulting regime in the III-D with NW-SE compression orientation transformed to strike-slip faulting in the II-D with NE-SW compression orientation has promoted the development of these new fractures (Fig 4.22D) without reactivation processes. At the shallower part (Fig 4.22C), few risky fractures in the central region are identification. Under the stress field of northernmost of NE Taiwan coastline area (Fig 4.22B), 7 (64%) new unstable fractures are realized and generally in Domain I. Meanwhile, no fractures plane developed by the strike-slip faulting regime at the shallower part (Fig 4.22A).

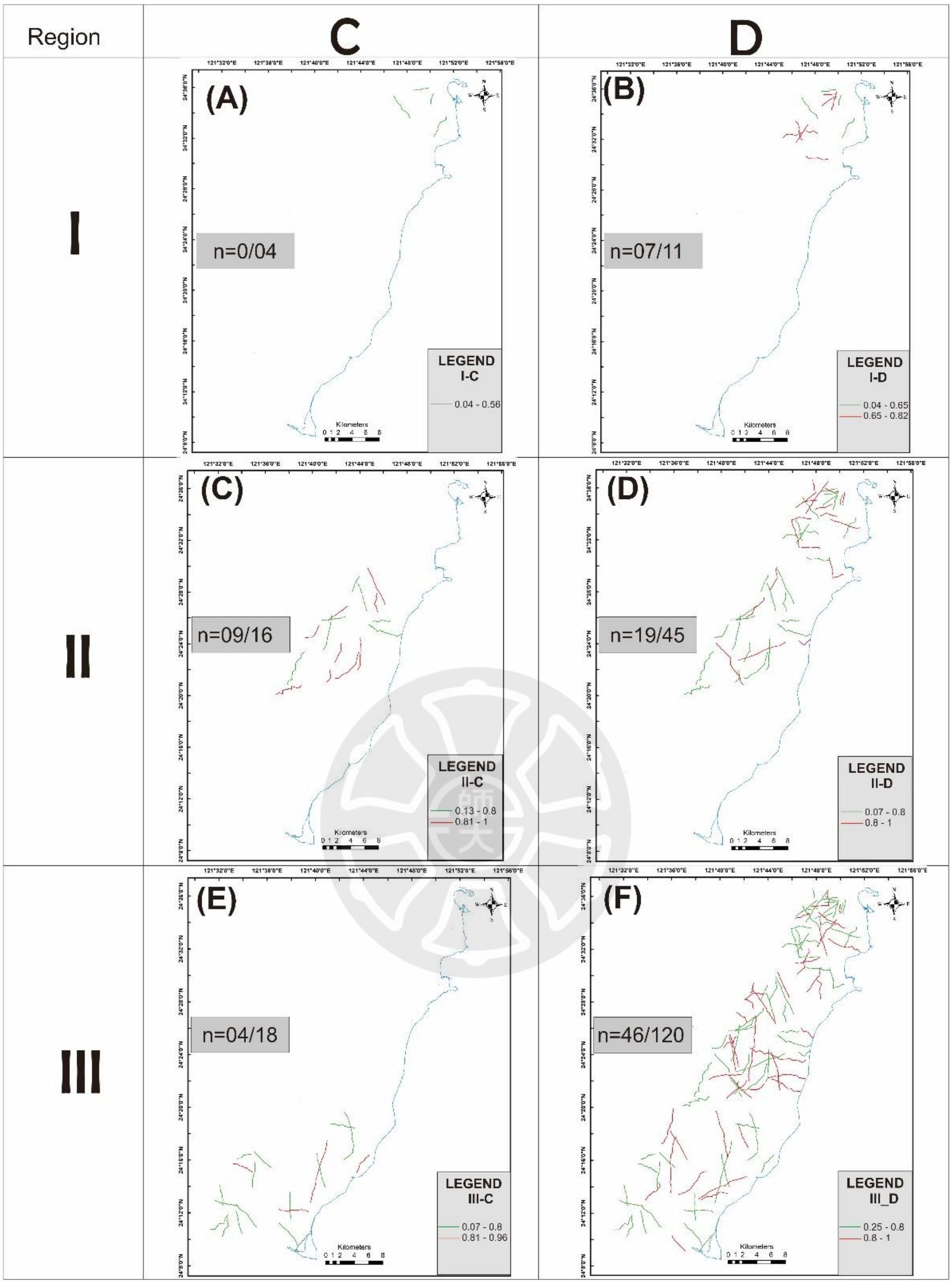

Figure 4.22: The evolution of surface fracture patterns in NE Taiwan through the stress field variation from southern to the northern part along with NE Taiwan (red, green lines described the risky or un-risky fracture planes). n is the number of the unstable fracture planes within inactive of fractures from previous stress state.

CHAPTER 5: DISCUSSIONS

This chapter aims to discuss (1) verifying the number and quality of surface fracture planes, which are derived from DEM data, because the surface process, such as erosion, might affect the identification of quality and quantity of fracture planes during mapping. (2) examining the stress evolution path based on the result of the stress state along cross-sections from surface to 10 km depth at NE Taiwan. Basically, our results, consistent with many previous studies, indicated that the evolution of stress state from reverse faulting regime at the south to strike-slip faulting at the north of NE Taiwan. However, we also found the strike-slip faulting regime in the shallow crust of Domain III. (3) evaluating the spatial distribution of mean strike of fracture planes with the evolution of regional stress state from the south to the north of NE Taiwan, because of the results of the fracture pattern could be consistent with the evolution of the stress state (Chapter 4). In comparison, nucleated fracture patterns along stress evolution differ with fracture pattern generated from each cell, thus (4) to examine the reactivation of surface fractures with the evolution of stress states in the coastline area of NE Taiwan. The reactivated fracture planes will be analyzed by evaluating the slip tendency. (5) In counting, except nucleated fractures and reactivated fractures, 4 remained fracture planes only were generated without seismic activity and might be constructed by the surface process.

5.1 Mapping limitations of DEM in metamorphic area

DEM can be used to detect and map the signatures of geological features in the context of topography (Tarolli and Dalla Fontana, 2009; Arrowsmith and Eielke, 2009; Chen and Wang, 2014). The resolution of 5-meter DEM data, which contains the vegetation layer, challenges the interpretation and mapping of the fracture planes. However, our assumptions supposed that the fracture pattern could correlate with the evolution of the stress state, which derived from earthquake events. Therefore, the length of surface fracture should be large than the expected rupture length of earthquakes. The mapped fracture plane in the DEM is reliable to compare with the investigation field works. Some small factors influenced the reliability of fracture planes during the mapping process will be discussed:

1. The differentiation between fracture and foliation plane is highly based on cross-cutting relationships. It is a clear observation that fracture cuts foliation. For example, the single-plane, breaking the ridge (numbered by 1), cut the parallel, planar and triangular faces, characterized as foliation (Fig 5.1). The cross-cutting relationship between fractures and foliations can be accurately reflected the relative timing of foliation and fracture planes on a small scale. Observing the fracture in the 3D view, the surface of the fracture plane primarily is un-smooth because of the significant existence of foliation traces (purple arrows in Fig 5.1A).
2. Furthermore, the surface process is primarily active in foliation with favorable orientation and promoted the display of foliation plane on the surface. However, the effectiveness of the surface process has differences in different areas. For example, the different erosion rates triggered by natural conditions (slope, raining, etc.) on two flanks of the mountain will manipulate the apperception of notable

traces of foliation and fracture. The eroded material can cover part of the fracture plane to make the fracture smaller, shorter on the surface (Fig 5.1B&C). Thus, the modification of landscape from the surface processes not only can cause the fracture or foliation traces unclearly observed but also can discontinue the trace of fracture planes (Fig 5.1D&E). From that, it will be challenge to connect foliation or fracture traces across two sides of the mountain or valley. However, in order to warrant that the reasonable fractures and foliations are plane, they are necessarily traced through the ridge or valley. And the fracture planes are created by earthquake events under assumptions. Hence, the minimum lengths should be large than 1km (Fig 4.9). In the 2D view, traces of foliation or fracture plane on the surface are curved lines, and their estimated planes in 3D view are approximately planar.

3. The resolution of DEM absolutely should be enhancing to obtain detailed results. Remote mapping foliation and fracture can be a replacement to reduce the threatening, and costly field works. Our study result indicated with the attitudes of the foliation plane in DEM calculation (Chapter 4) are usually compatible field data of foliation in the accessible area of NE Taiwan. Therefore, the mapping of foliation planes can be considerably mapped in the high mountain of the metamorphic area with the investigation of the high resolution of DEM. Therefore, it encourages the implementation of the structural studies with trustable information of fracture distribution in the high mountain.

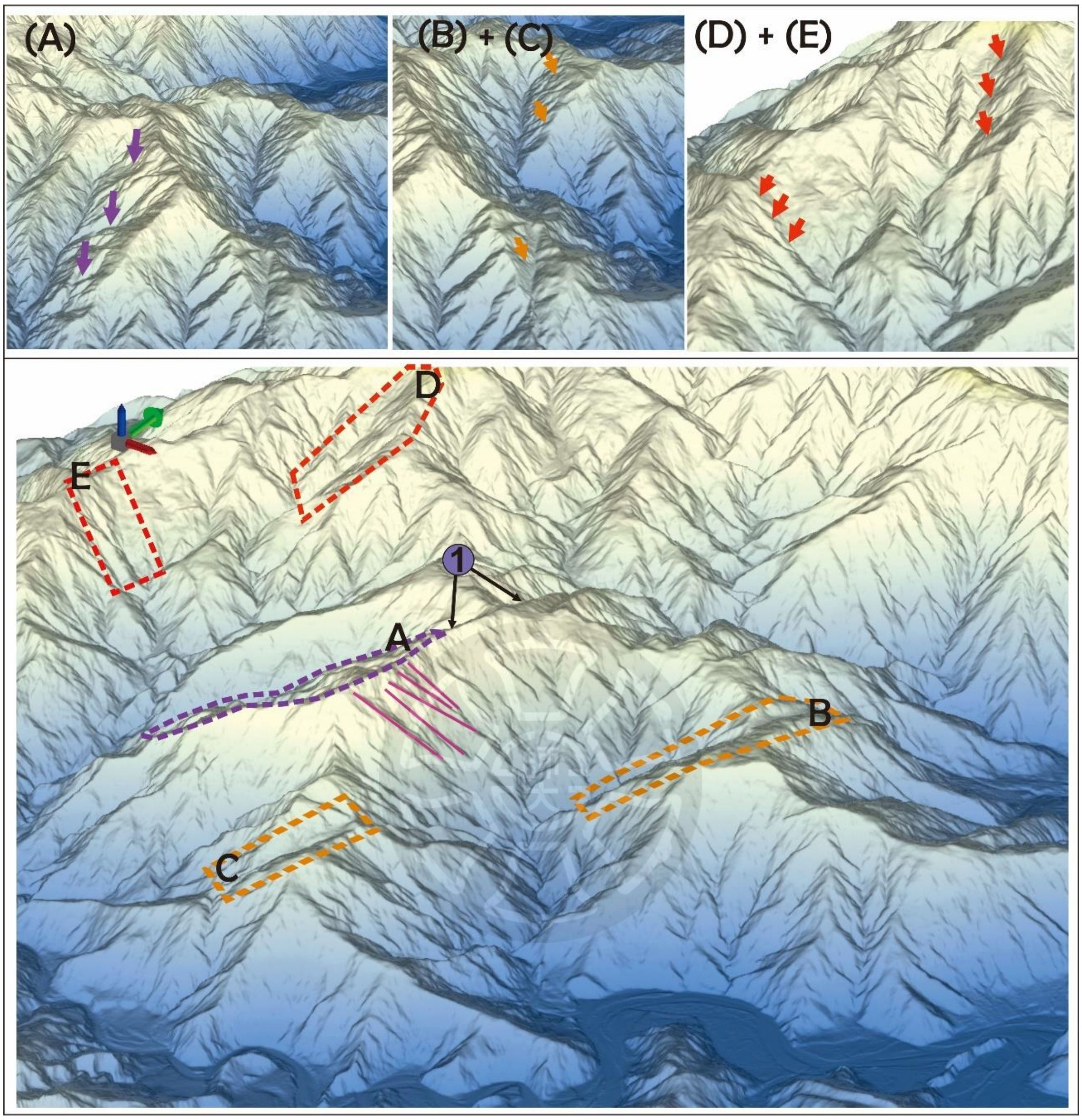

Figure 5.1: The effective surface process on fracture plane mapping. The appearance of parallel, planar, triangular faces of foliation (pink lines), and single planar of fracture planes (numbered by 1) in the 3D view of Arc Sense software. (A) The purple arrows indicated the existence of foliation traces on the surface of the fracture plane. (B&C) Short and small fracture plane. (D&E) Unclearly part of fracture planes in the slope of mountain flank.

5.2 Stress inversion results and stress evolution path in NE Taiwan

In general, the stress inversion results in our study are similar to previous works (Shyu et al., 2005; Wu et al., 2008; Wu et al., 2009; Wu et al., 2010; Huang et al., 2012). The results display that the stress states primarily transfer from reverse faulting regime at the Domain III to strike-slip faulting at Domain I (Fig 4.17). This evolution of stress state has already been discussed and confirmed that it might result from the change of plate motion between two plates at about the latitude of 23.7° of NE Taiwan region (Wu et al., 2009). In addition, in this study, when we evaluated stress state at the cross-sections from surface to 10 km depth around the coastline area of NE Taiwan, we found the change of stress field near the Heping area (Fig 4.12 & 4.13) instead, the transition had been found at adjacent Dongao plain by Huang et al. (2012) (Fig 1.1A).

The strike-slip faulting regime at 7.5 km depth of Domain III-C could relate with the back-arc opening and PSP-EP subduction system because the intermediate axis (σ2) of principal stress starts keeping vertical while the compression axis (σ_1) is the horizontal component at NW orientation. The results of the focal mechanism of the NE seismic zone (Wu et al., 2008) represented that the crust separates into two layers. The intermediate-depth layer of earthquakes events is related to the subduction system between PSP and EP, whereas the layer at shallow events is primarily associated with the opening of the Okinawa Trough and subduction system between PSP and EP. In detail, Huang et al. (2012) proposed that the upper crust of the northern part of the Coastal Range attached to the EP and are left above the Domain III surface, while the middle to lower crust needs to subduct northward with the PSP. This argument is based on the model provided by Wu et al. (2010). Therefore, the strike-slip focal mechanism event at 7.5 km of the northern part of the Coastal Range could be correlated with the stress state in Domain I, where are conducted by collision and back-arc Okinawa Trough opening (Fig 4.13 & 4.17). It supported that the strike-slip faulting regime in the northern part of NE Taiwan was more dominant and became the driving force to construct the fracture surface. And the fracture planes at Domain III in the upper crust (< 7.5km) could be influenced by the strike-slip faulting regimes.

Stress evolution also supported the transformation between the compression and extension orientation of principal stress from south to the north along with NE Taiwan. The cross-section represented the permutation of σ_1 and σ_3 orientation from domain III via Domain II to the Domain I of stress inversion results in Figure 4.17. These results are consistent with previous studies (Wu et al., 2008; Huang et al., 2012). The maximum principal stress (σ_1) orientation of N135°E at Domain III was parallel to the plate motion vector of PSP when it collided with EP at NE Taiwan at N55°W (Suppe, 1984; Yu et al., 1999). In the transitional area (Domain II), the minimum principal stress (σ_3) orientation substituted the maximum principal stress (σ_1) orientation from NE-SW to NW-SE direction. This indicates that the correlation of the stress state with the subduction system between PSP and EP and back-arc opening of Okinawa Trough (Wu et al., 2009; Nakamuara, 2004) and also implies the strong influences of subduction and back-arc opening movement in northernmost of NE Taiwan region. Additionally, the transformation of tectonic forces in the transition area was confirmed the slow clockwise rotation rate of 0.5° ± 0.63°/Myr of Central Range Block (CeR) (Rateb et al., 2017). Their model also illustrated that the GPS velocity is different in the south and north of CeR. In the south, CeR is not entirely rigidly rotated northwestward, whereas northern CeR turns eastward to southeastward. This movement of northern CeR has been proposed to be bent due to the southward development of the back-arc extension and subduction system (Huang et al., 2012). According to the difference of GPS velocity between the southern and northern parts of NE Taiwan, the spatial distribution of surface fracture could be changed.

5.3 Spatial distribution of surface fractures

The back-arc opening of Okinawa Trough is becoming the driving forces (Fig 5.2) (Huang et al., 2012) to cause the evolution of reverse faulting regime in the southern part (domain III) via strike-slip faulting regime in the central (Domain II) to northern part (Domain I) of NE Taiwan (Fig 4.17, Fig 4.18). According to Huang et al. 2012, the development of the southward opening of Okinawa Trough results in the southward movement of CeR and the western Ryukyu arc. Therefore, the tectonic force of NW-SE opening could be the main reason for promptly the NW-SE bending of the crust in the northern part of CeR (Fig 5.2); (Huang et al., 2012; Rateb et al., 2017) and be strongly related with the development of a distinct fracture pattern of each domain (Fig 5.3).

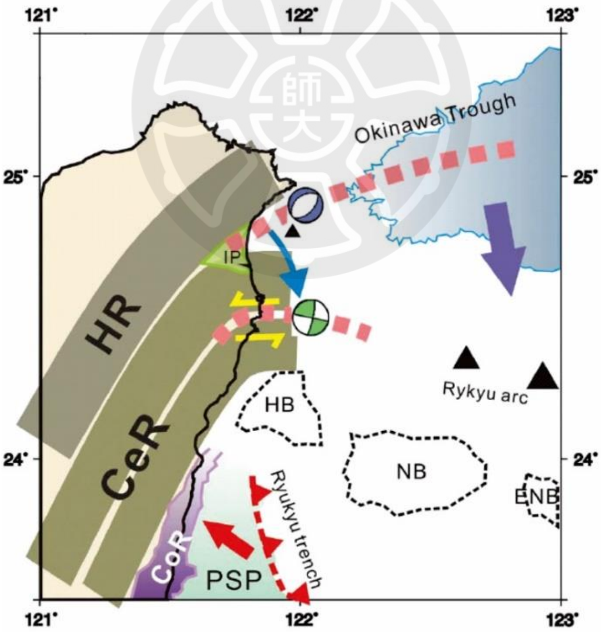

Figure 5.2: The current kinematic model of NE Taiwan (Huang et al., 2012). This model proposed the consequence of the dominant driving force of back-arc opening into the topography of NE Taiwan.

In Figure 5.3, the mean strike of surface fracture was recognized in N-S orientation at Domain III, and the dip angle approximately in the range of 20-25° toward the west. Due to the southwestward bending of the southern CeR, the dominant strike of surface fracture differs 55° compared with the collision vector of N55°W between LVA with EP at (Suppe, 1981; Chi, 1981). However, the maximum principal stress (σ_1) orientation at N135°E-N140°E in Domain III-D (Table 4.6, Fig 4.17) was consistent with the motion vector of PSP, resulting in the 23/46 nuclear surface fractures in three Domains (Fig. 4.22).

The mean strike of surface fracture changed from N-S orientation at domain III to NE-SW orientation at the domain II (Fig 5.3). It is the first significant signal to mark the clockwise rotation of the northern CeR block (Huang et al., 2012; Rateb et al., 2017) due to the northward subduction of PSP under the EP in northern Taiwan. The consequences of this evolution stress state in the transition area also confirmed that the mean strike of fracture plane at N20°E-N23°E is related to the orientation of the maximum of principal stress ($\sigma 1$) orientation of Domain II-D with N46°E-N52°E (Table 4.6, Fig 4.17).

In the southern area of Ilan Plain, the fracture planes with strike orientation in the range of N35°E-N38°E are dominant. The maximum principal stress ($\sigma 1$) orientation of Domain I ranged from N50°E-N70°E. The minimum principal stress ($\sigma 3$) orientation agree well with the extension axis of Okinawa Trough opening (Table 4.6, Fig 4.17). In comparison, the mean strike of fracture in the Domain I larger than domain II because it could be responded strongly to the influence of the subduction and back-arc opening. Furthermore, the rapid rotation rate of the Southern Ilan Block (Rateb et al., 2017), estimated around 34.9° ± 65.9° in southward movements, might influence the strike differences of surface fractures at Domain I with the mean fracture plane of Domain II.

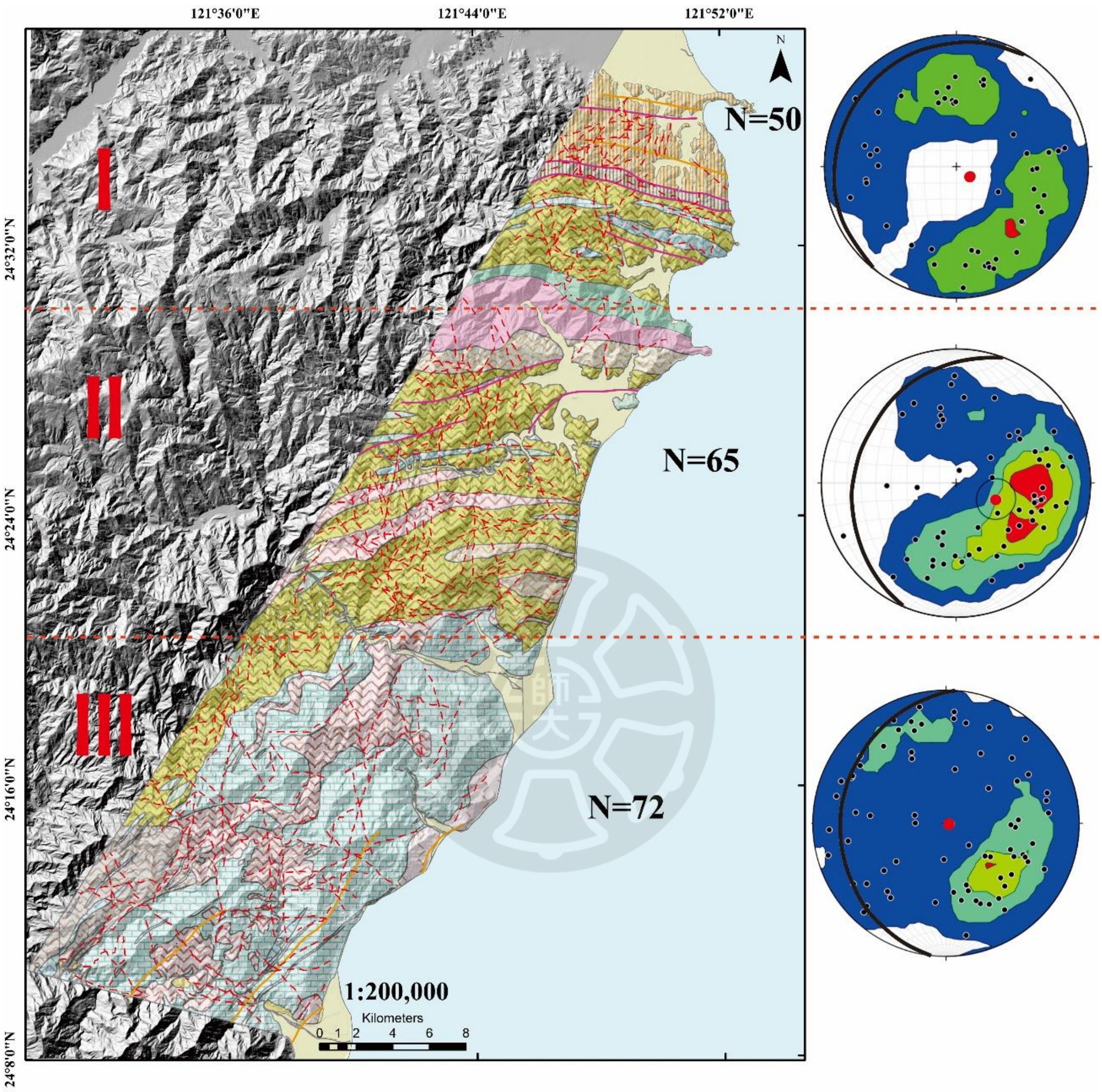

Figure 5.3: Distribution of mean strike of surface fractures from southern to northern part of NE Taiwan coastline.

The fracture instability results show that the distribution of nucleated surface fractures is moderately corresponded with the evolution of the stress regime from the south to the north region (Fig 4.22). And, the mean strike pattern of the fracture plane in Domain II and Domain I strongly response with the opening of Okinawa Trough due to the bending of NE Taiwan topography. Therefore, the regional normal stress state derived from the back-arc opening strongly influenced on the fracture system of NE Taiwan. To evaluate the crucial position of the normal faulting regime affected the fracture system, we produce the fracture instability of 120 surface fractures (Fig 5.4).

In Figure 5.4, 120 surface fracture instabilities on the different cross-section of the stress state of each cell are demonstrated. The risky surface fractures were dedicated by red lines, mainly dominant in Domain I and II (Fig 5.4A; Fig 5.4B and Fig 5.4C). The amount of these sensitive fractures certainly recognized in I-D, I-C, II-C cells is 75, 52, and 58 fracture planes, respectively. And, 46, 28, and 36 fracture planes are identified in III-D, III-C, II-D cells. Therefore, the different distribution of higher fracture instability in different cells and the superiority of number fracture planes in the Domain I and II could emphasize the important role of rifting development in southern Okinawa Trough. Based on the occupation of the normal stress regime in the frequent earthquake event that happened in NE Taiwan, this stress state produces of normal faulting stage of the reactivation of the nucleated surface fractures in this area. To analyze the reactivation of surface fractures, we evaluated slip tendency analysis in section 5.4.2.

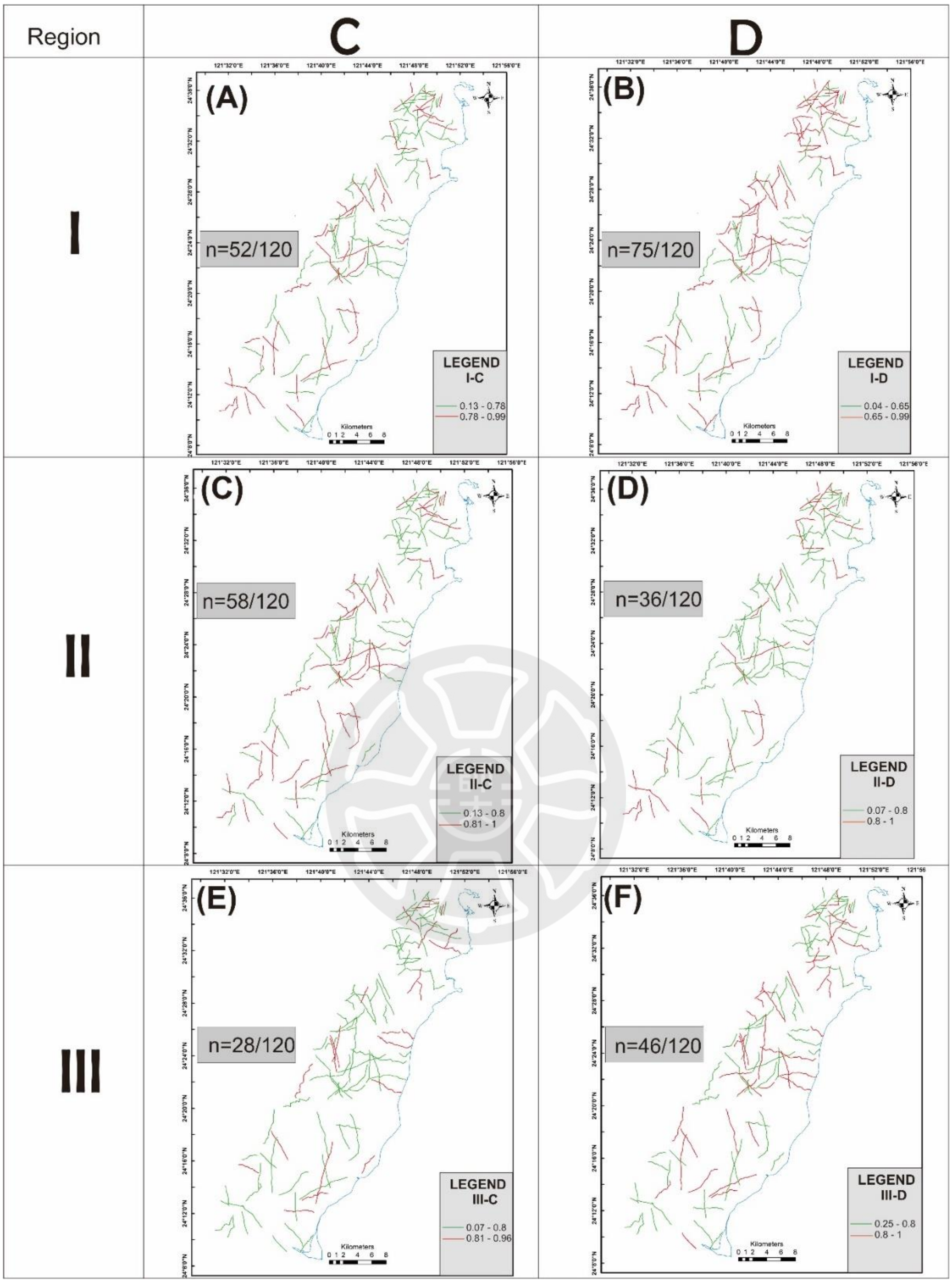

Figure 5.4: Nucleated fracture at NE Taiwan under the prevailing stress regime at each cell from southern to northern part of NE Taiwan. Red, green lines indicated for unstable and stable fracture, respectively. n demonstrated the unstable fractures within 120 selected surface fractures from DEM data.

5.4 Evaluation of reactivated fractures in NE Taiwan

The coastline area along NE Taiwan has experienced the evolution of the stress field from southern to the northern part (Fig 4.17). The nucleated surface fracture planes can be compatible with stress state evolution (Fig 4.22). Besides that, the driving force of the back-arc opening is dominant and could motivate the reactivation of the pre-existing fracture system in NE Taiwan. Therefore, we proposed another stage to the evolution model of the stress pattern of this area (Fig 5.5). In this model, the latest stage (Fig 5.5) of the tectonic setting, the normal stress regime, more activates, and generates the reactivated fracture pattern in the study area. We use the slip tendency analysis to verify whether the subsequent stress sequences of the earthquake events can govern the fracture reactivation.

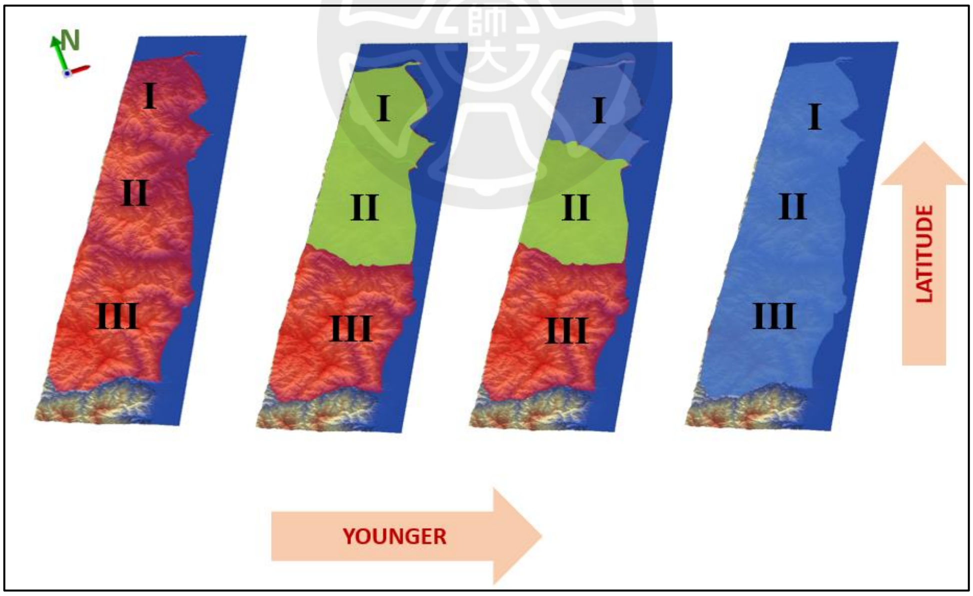

Figure 5.5: A proposed evolution model of reactivated fracture patterns in NE Taiwan.

5.4.1 Slip tendency analysis

5.4.1.1 Slip tendency

Slip tendencies basically represented the slip ability of the fracture plane in an applied stress state (Morris et al., 1996; Ferrill et al., 1999; Lisle and Srivastava, 2004). In Figure 5.6, the given normal faulting regime forced the potential slip on the fracture plane. The giving fracture plane where shear stress and normal stress acting on would reveal the slip direction. And, slip likely occurs when resolve shear stress (direction of slip), ج, is equal or exceeds the frictional sliding resistance. Hence, the slip tendency is the ratio of resolved shear stress to resolved normal stress on the surface (Morris et al., 1996) and is indicated by Equation 5.1:

$$Ts = \left(\frac{\tau}{\sigma_{eff}}\right) > \mu s \qquad \text{(Eqn. 5.1)}$$

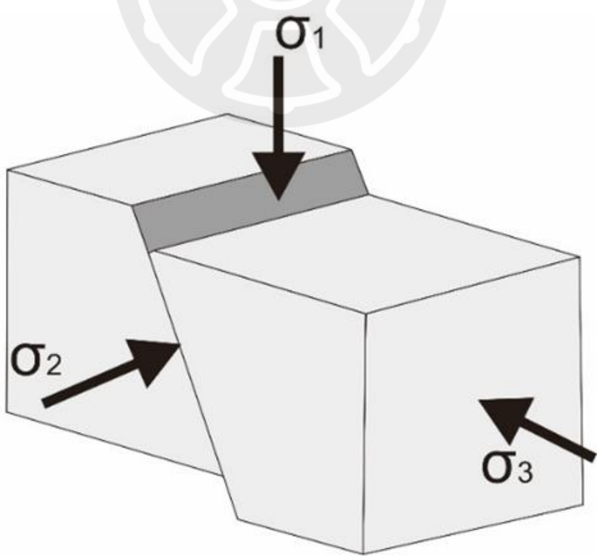

Figure 5.6: The simulation model of slip tendency in applied stress state with three principal stress components σ1, σ2, and σ3 with σ1 > σ2 > σ3.

5.4.1.2 The threshold of slip tendency at Domain I

The threshold of fault plane in domain I-C is defined by the minimum of slip tendency value in CDF (Fig 5.9A); it presented 0.7. In the I-D, we picked 20% (slip threshold is 0.65) of fault planes from the focal mechanism (Fig 5.9B) to evaluate the distribution of reactivated surface fracture of NE Taiwan.

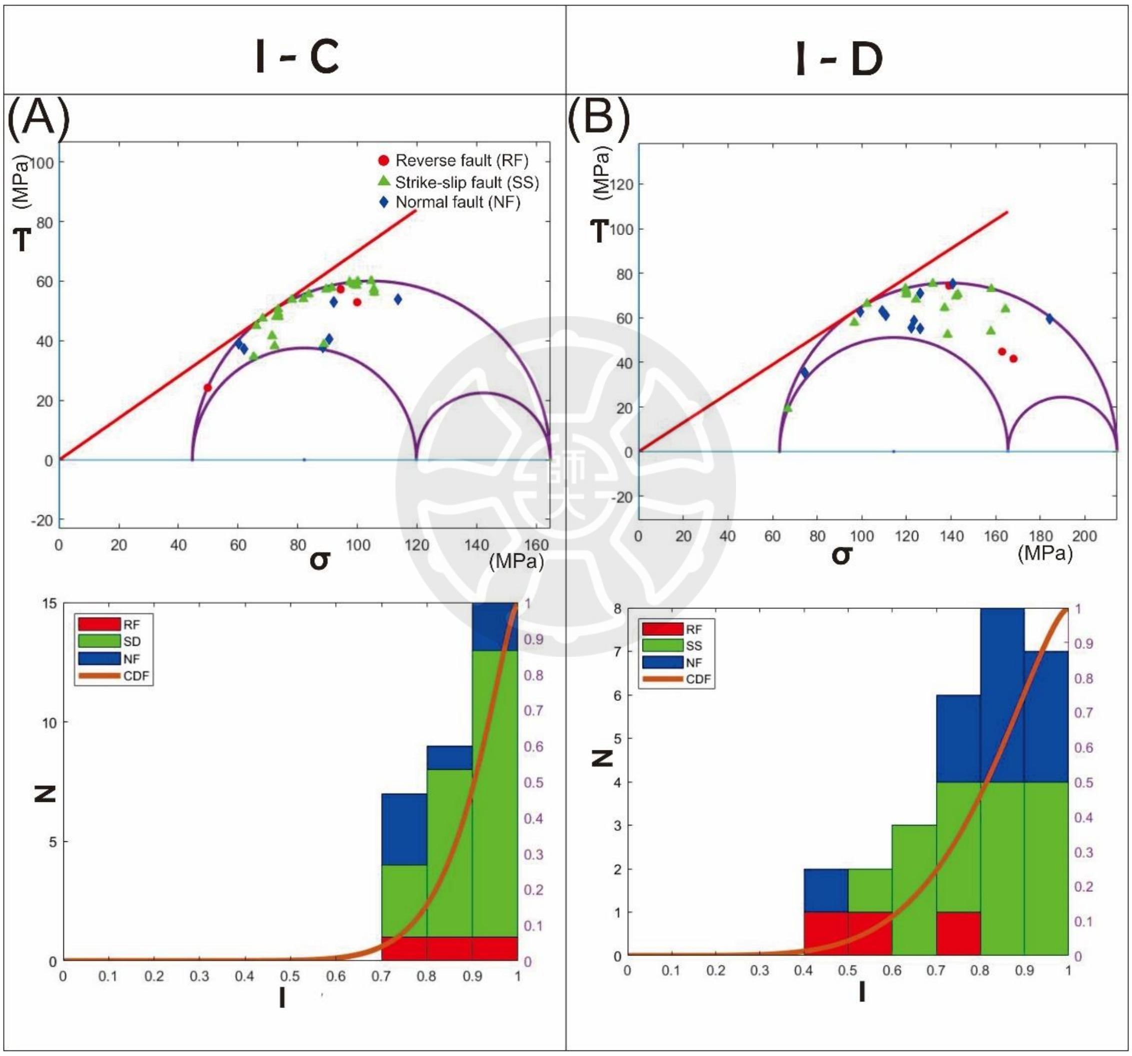

Figure 5.7: Threshold of slip tendency at Domain I

5.4.1.3 The threshold of slip tendency at Domain II

The threshold of slip tendency highly recommends 0.8 for both II-C and II-D cells because we picked 40% of the seismic focal plane in CDF (Fig 5.8A&B).

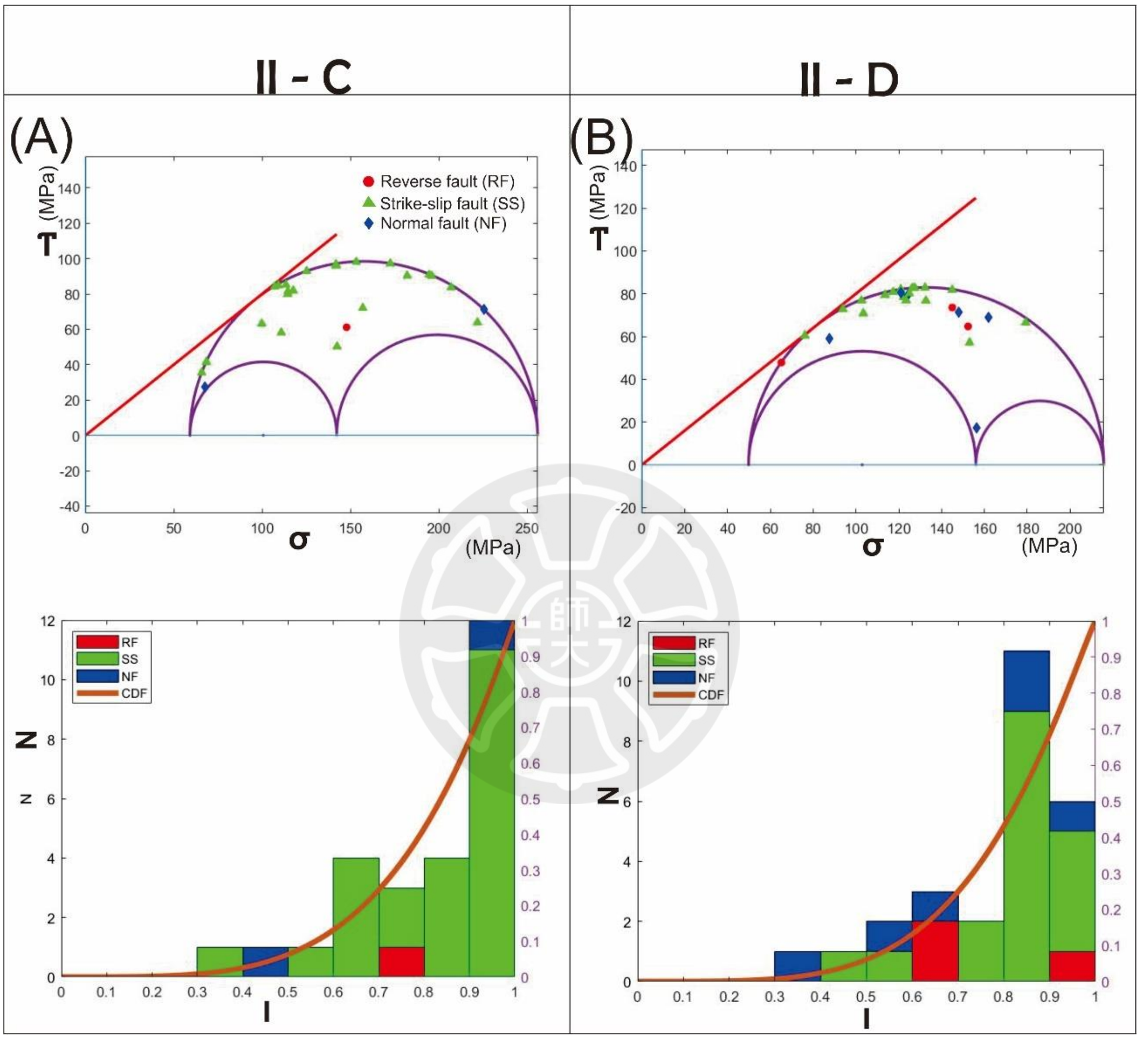

Figure 5.8: Threshold of slip tendency at Domain II

5.4.1.4 The threshold of slip tendency at Domain III

In a similar way of estimating the threshold of fracture instability, the threshold of slip tendency is estimated by evaluating the distribution of stress values inferred from the focal mechanism in the Mohr's diagram. The slip tendency is analyzed at the cohesionless surface of the fracture plane.

The threshold of slip tendency in the Domain III-C clearly showed 0.8 because the dominance of normal seismic fault in this cell can be reactivated when slip tendencies large than 0.8 (Fig 5.7A). In the Domain III-D, the determination of threshold is difficult, but according to Mohr's circle of slip tendency distribution and CDF, we picked up 20% focal planes to be slip as the slip tendency (0.8) of surface fracture.

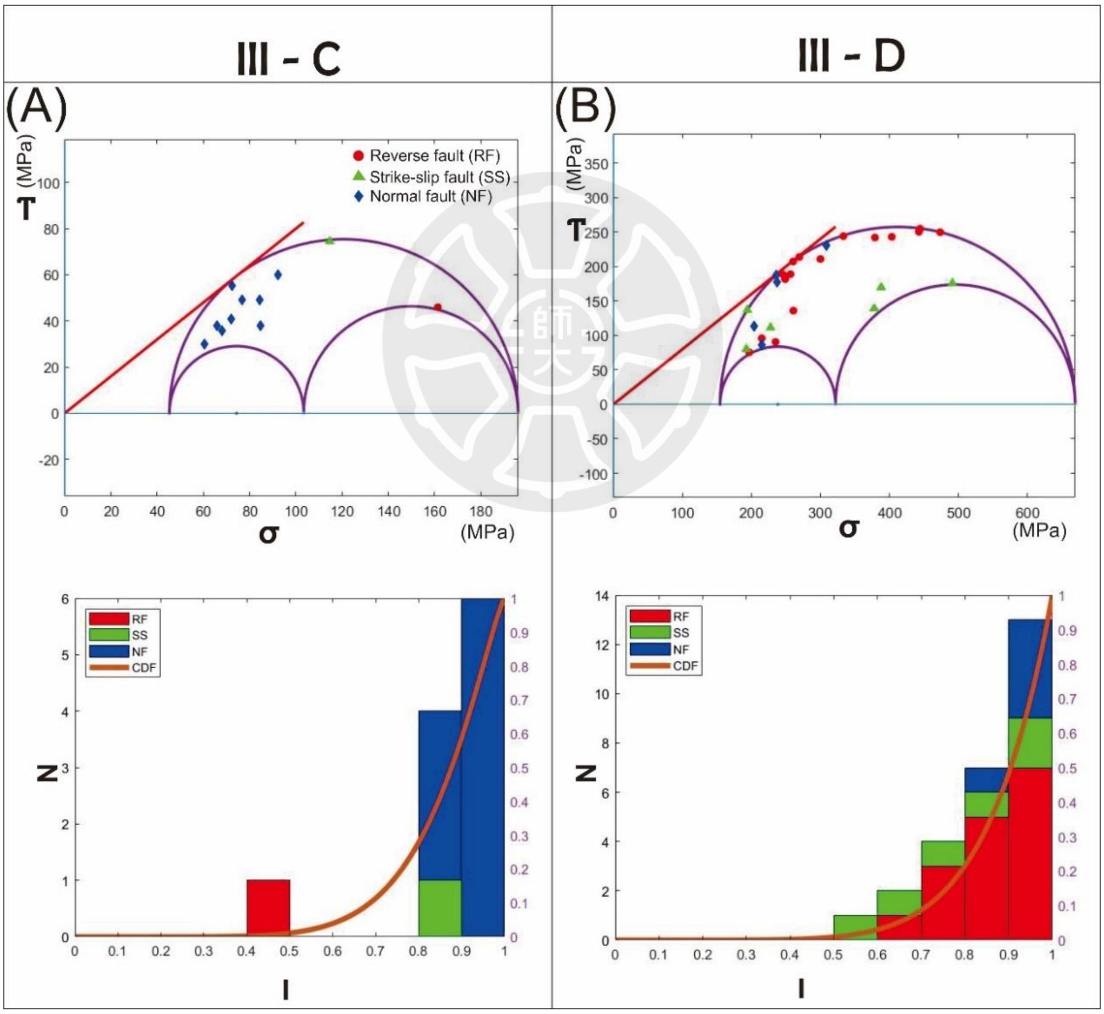

Figure 5.9: Threshold of slip tendency at domain III

The threshold of surface fracture planes in three domains defined and summarized in Table 5.1.

Table 5.1: Threshold values of slip tendency in this study.

	Domain I	**Domain II**	**Domain III**
C	**0.70**	**0.8**	**0.8**
D	**0.65**	**0.8**	**0.8**

5.4.2 The reactivated fractures in the tectonic evolution scenery

The reactivation examination of pre-existing surface fractures in NE Taiwan is based on calculating and analyzing slip tendencies of the 120 fracture planes under the opening of Okinawa Trough. The potential fractures slipped under the stress field are highlighted by red lines (Fig 5.10). In the counting, only 18, 9& 14 nucleated fracture planes of III-D, III-C& II-D cells (Fig 5.10D, Fig 5.10E, and Fig 5.10F), respectively, are going to reactivate under the operation of reverse faulting regime and strike-slip faulting regime. And, in the comparison, the reactivated fractures statistics in Domain I (Fig 5.10A and Fig 5.10B) and lower crust of Domain II (Fig 5.10C) show that the number of fracture planes is prominently reactivation. 65, 48, and 40 surface fracture planes are supposedly reactive due to the stress regime evolution and exhumation.

In Domain III, 18 fractures distributed in domains I and II can be reactivated under the III-D reverse faulting stress. Only one fracture plane could be reactive in Domain III (Fig 5.10F). The mean strike of the fracture plane reactivated by II-D stress shows the N-S orientation in the lower hemisphere. At 7.5km for III-C, II-C, and I-C, when σ_2 became the horizontal components instead σ_3 (Fig 4.17), the number of reactivated fracture planes in the study area are different 6/9 fracture planes are located in Domain III, and the mean fracture plane displayed a NE-SW striking (Fig 5.10E).

In domain II, the number of reactivated fractures under the strike-slip faulting regime (II-D) was less than reactivated fractures under the reverse faulting regime (III-D). 14 fractures planes were recognized in II-D cell, only 2/14 fracture planes in the domain III could be reactivated. The 14 reactivated fractures present an N-S strike in the lower hemisphere (Fig 5.10D). The result of slip tendency analysis under II-C stress represented that the reactivation of surface fracture is more predominant. 40 surface fractures can be reactivated, and most of the reactivated fractures found in Domain I and III (Fig 5.10C). In the lower hemisphere, the mean fracture of 40 reactivated fracture at II-C marked NE-SW orientation.

In the Domain I, surface fractures along the coastline of NE Taiwan strongly respond with the strike-slip faulting regime. At 10km, 65/120 (54%) surface fractures are able to reactivate (Fig 5.10B). These reactivated fractures were located in three domains, and the ENE-WSW striking of mean fracture was represented in the lower hemisphere. At 7.5km, 40/120 (30%) of surface fractures could be reactivated under the I-C stress (Fig 5.10A). And, in the lower hemisphere, the mean strike of the fracture plane at I-C presented the NE-SW orientation. It is different from the mean strike of fracture at III-D in the comparison; the mean fracture plane of I-D cell presented ENE-WSW striking. Therefore, the mean strike of fracture at the study area has clockwise rotation, from N-S orientation in III-D and II-D via NE-SW orientation in III-C, II-C, and I-C to ENE-WSW orientation in I-D.

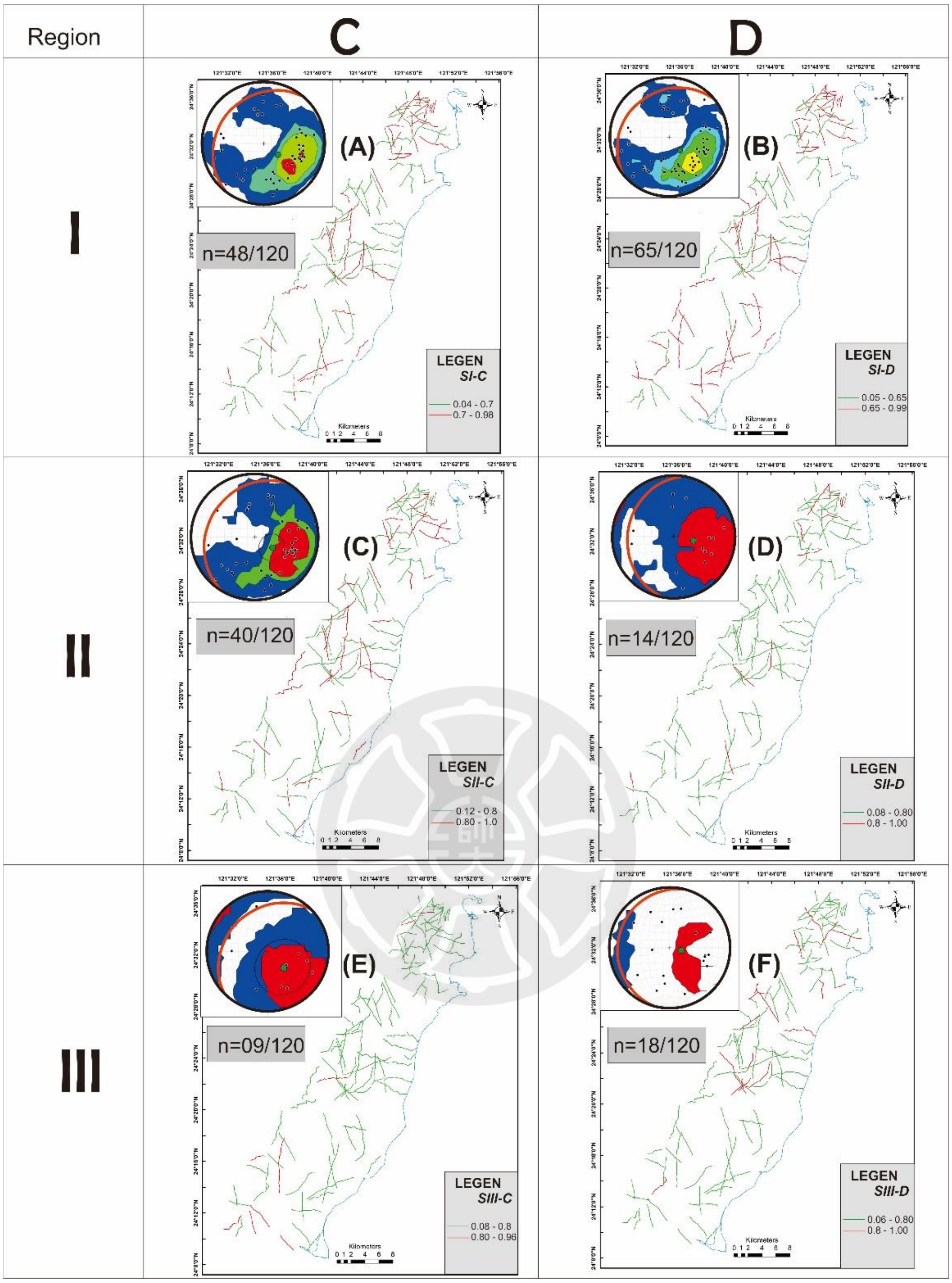

Figure 5.10: Reactivation of surface fractures in the scenario of tectonic evolution in NE Taiwan. Red and green lines described the reactivated and inactivated fracture plane, respectively. n is the number of the reactivated fracture planes in given stress state andmean reactivated fractures (red great circle) are showing in the lower hemisphere projection.

As a result, it supported that a new stage of normal faulting is influenced on NE Taiwan, which was provided by Huang et al. (2012). The scenery declared that the opening of the Okinawa Trough became a dominant driving force in the regional stress regime. In our study, the result presented that earthquake events near southern Ilan Plain (Domain I) is specified as strike-slip faulting, and the focal mechanism cluster located in Domain II also is characterized by strike-slip faulting. These seismic events of tectonic motion between the PSP-EP subduction system and back-arc opening of Okinawa Trough along the Ryukyu trench delivered high motivation in reactivation of pre-existing surface fractures in NE Taiwan.

CHAPTER 6: CONCLUSIONS

This study aims to evaluate whether fracture development can correspond to the stress evolution from compression to extension along NE Taiwan. To accomplish this study, the work contains three parts: (1) To measure and calculate attitudes of surface fracture plane and foliation based 5-meter DEM data. (2) To investigate the regional stress state by analyzing focal mechanism data in period 1991-2015, from the southern part (Domain III) to central (Domain II) and northern NE Taiwan (Domain I) and (3) To correlate the surface fracture pattern with the evolution of stress state based on fracture instability calculation. In summary, the following points can be concluded:

1、 After examining the DEM data, the fracture system at NE Taiwan can be recognized and constructed in 3D view based on the interpretation of the cross-cutting relationship between foliation and fracture. 187 fracture planes have recognized and calculated their attitudes.

2、 The stress state of the cross-section constructed by this study can reveal the overview of the structural evolution in the coastline area of NE Taiwan. The combination of the evolution of stress state and exhumation along the coastline from south to north can provide the evolution path of nucleated and reactivated fracture patterns in this area.

3、 Threshold values of fracture instability and slip tendency from focal mechanism data can be used to define the tendency of nucleation or reactivation of surface fractures.

4、 The evolution of regional stress state from reverse faulting to strike-slip faulting confirmed to play a crucial role of manipulating surface fractures pattern from N-S strike in the south to ENE-WSW strike in the north along the NE coastal area of Taiwan.

5、 The number of nucleated surface fracture planes of Domain I is highest (64%), and the surface fractures from DEM-derivation of NE Taiwan can be correlated with the evolution of the stress state.

6、 54% fracture planes in Domain I can reactivate under the activity of the back-arc opening of Okinawa Trough in the north of NE Taiwan.

REFERENCES

Angelier, J., Bergerat, F., Chu, H.T., & Lee, T.Q. (1990). Tectonic analysis and the evolution of a curved collision belt: the Hsüehshan Range, northern Taiwan. Tectonophysics, 183(1-4), 77-96.

Arrowsmith, J. R., & Zielke, O. (2009). Tectonic geomorphology of the San Andreas Fault zone from high resolution topography: An example from the Cholame segment. Geomorphology, 113(1-2), 70-81.

Beeler, N. M., Simpson, R. W., Hickman, S. H., & Lockner, D. A. (2000). Pore fluid pressure, apparent friction, and Coulomb failure. Journal of Geophysical Research: Solid Earth, 105(B11), 25533-25542.

Bott, M. H. P. (1959). The mechanics of oblique slip faulting. Geological Magazine, 96(2), 109-117.

Campagna, D., & Levandowski, D. (1991). The recognition of strike-slip fault systems using imagery, gravity, and topographic data sets. Photogrammetric Engineering and Remote Sensing, 57(9), 1195-1201.

Chen, K. H., Toda, S., & Rau, R. J. (2008). A leaping, triggered sequence along a segmented fault: The 1951 ML 7.3 Hualien-Taitung earthquake sequence in eastern Taiwan. Journal of Geophysical Research: Solid Earth, 113(B2).

Chen, W. S., Huang, Y. C., Liu, C. H., Feng, H. T., Chung, S. L., & Lee, Y. H. (2016). UPb zircon geochronology constraints on the ages of the Tananao Schist Belt and timing of orogenic events in Taiwan: Implications for a new tectonic evolution of the South China Block during the Mesozoic. Tectonophysics, 686, 68-81.

Chen, X., & Wang, J. (2014). A comparison of two-fluid model, dense discrete particle model and CFD-DEM method for modeling impinging gas-solid flows. Powder Technology, 254, 94-102.

Chen, Y. F., Hu, S. H., Hu, R., & Zhou, C. B. (2015). Estimating hydraulic conductivity of fractured rocks from high-pressure packer tests with an Izbash's law-based empirical model. Water Resources Research, 51(4), 2096-2118.

Chi, W. R., Namson, J., & Suppe, J. (1981). Stratigraphic record of plate interactions in the Coastal Range of eastern Taiwan. Memoir of the Geological Society of China, 4, 155-194.

Chiang, S.C. (1976), Seismic study in the Ilan Plain [in Chinese], Mining Technology, 14(6), 215-221.

Chiba, T., Kaneta, S. I., & Suzuki, Y. (2008). Red relief image map: new visualization method for three-dimensional data. The International Archives of the Photogrammetry, Remote Sensing and Spatial Information Sciences, 37(B2), 1071-1076.

Chiba, T., & Hasi, B. (2016). Ground surface visualization using red relief image map for a variety of map scales. The International Archives of the Photogrammetry, Remote Sensing and Spatial Information Sciences, XLI-B2, 393-397.

Chou, C. C., & Chen, Y. C. (2012). Development and seismic performance of steel dual-core self-centering braces. In 15th world conference on Earthquake Engineering, 24-28.

Clift, P.D., Lin, A.T., Carter, A., Wu, F., Draut, A.E., Lai, T.-H., Fei, L.-Y., Schouten, H., & Teng, L., (2008). Post-collisional collapse in the wake of migrating arc-continent collision in the Ilan Basin, Taiwan. Special Papers Geological Society Of America, 436, 257-278.

Cracknell, M. J., Reading, A. M., & McNeill, A. W. (2014). Mapping geology and volcanic-hosted massive sulfide alteration in the Hellyer–Mt Charter region, Tasmania, using Random Forests™ and Self-Organising Maps. Australian Journal of Earth Sciences, 61(2), 287-304.

Delaney, P. T., Pollard, D. D., Ziony, J. I., & McKee, E. H. (1986). Field relations between dikes and joints: emplacement processes and paleostress analysis. Journal of Geophysical Research: Solid Earth, 91(B5), 4920-4938.

Ernst, W. G. (1983). Mineral parageneses in metamorphic rocks exposed along Tailuko Gorge, central mountain range, Taiwan. Journal of Metamorphic Geology, 1(4), 305-329.

Ferrill, D. A., Winterle, J., Wittmeyer, G., Sims, D., Colton, S., Armstrong, A., & Morris, A. P. (1999). Stressed rock strains groundwater at Yucca Mountain, Nevada. GSA Today, 9(5), 1-8.

Florinsky, I. (2016). Digital terrain analysis in soil science and geology. Academic Press.

Fossen, H. (2016). Structural geology. Cambridge University Press.

Fuh, T. M. (1962). Metamorphic rocks of the Nanao district, Taiwan, with special reference to the origin of orthogneiss. Memoir of the Geological Society of China, 1, 113-132.

Ho, C. S. (1986). A synthesis of the geologic evolution of Taiwan. Tectonophysics, 125(1-3), 1-16.

Ho, C. S. (1988). An introduction to the geology of Taiwan, explanatory text of the geologic map of Taiwan. Central Geological Survey.

Hobbs, W. H. (1904). Lineaments of the Atlantic border region. Bulletin of the Geological Society of America, 15(1), 483-506.

Hsu, W. H., Byrne, T. B., Ouimet, W., Lee, Y. H., Chen, Y. G., Soest, M. V., & Hodges, K. (2016). Pleistocene onset of rapid, punctuated exhumation in the eastern Central Range of the Taiwan orogenic belt. Geology, 44(9), 719-722.

Hsu, Y. J., Yu, S. B., Simons, M., Kuo, L. C., & Chen, H. Y. (2009). Interseismic crustal deformation in the Taiwan plate boundary zone revealed by GPS observations, seismicity, and earthquake focal mechanisms. Tectonophysics, 479(1-2), 4-18.

Huang, H. H., Shyu, J. B. H., Wu, Y. M., Chang, C. H., & Chen, Y. G. (2012). Seismotectonics of northeastern Taiwan: kinematics of the transition from waning collision to subduction and postcollisional extension. Journal of Geophysical Research: Solid Earth, 117(B01313).

Kang, C.C., Chang, C.P., Siame, L., Lee, J.C. (2015). Present-day surface deformation and tectonic insights of the extensional Ilan Plain, NE Taiwan. Journal of Asian Earth Science,105, 408-417.

Ku, C.Y., Hsu, S.K., Sibuet, J. C., & Tsai, C.H. (2009). The neo-tectonic structure of the south western tip of the Okinawa Trough. Terrestrial Atmospheric and Oceanic Sciences, 20(5), 7.

Kukowski, N., Schillhorn, T., Huhn, K., von Rad, U., Husen, S., & Flueh, E. R. (2001). Morphotectonics and mechanics of the central Makran accretionary wedge off Pakistan. Marine Geology, 173(1-4), 1-19.

Kukowski, N., Hampel, A., Hoth, S., & Bialas, J. (2008). Morphotectonic and morphometric analysis of the Nazca plate and the adjacent offshore Peruvian continental slope-Implications for submarine landscape evolution. Marine Geology, 254(1-2), 107-120.

Lai, K. Y., Chen, Y. G., Wu, Y. M., Avouac, J. P., Kuo, Y. T., Wang, Y., Lin, K. C. (2009). The 2005 Ilan earthquake doublet and seismic crisis in northeastern Taiwan: evidence for dyke intrusion associated with on-land propagation of the Okinawa Trough. Geophysical Journal International, 179(2), 678-686.

Lallemand, S., & Liu, C. S. (1998). Geodynamic implications of present-day kinematics in the southern Ryukyus. Journal of the Geological Society of China, 41, 551-564.

Lattman, L. H. (1958). Technique of mapping geologic fracture traces and lineaments on aerial photographs. Photogrammetric Engineering, 24(4), 568-576.

Lee, C. S., Shor, G. G. Jr., Bibee, L. D., Lu, R. S., and Hilde, T. W. C. (1980). Okinawa Trough: Origin of a back-arc basin. Marine Geology, 35, 219-241.

Lee, C. T., & Wang, Y., (1988). Quaternary stress changes in northern Taiwan and their tectonic significance, Geological Society of China Proceedings, 31, 154-168.

Lin, C. W., Shieh, C. L., Yuan, B. D., Shieh, Y. C., Liu, S. H., & Lee, S. Y. (2004). Impact of Chi-Chi earthquake on the occurrence of landslides and debris flows: example from the Chenyulan River watershed, Nantou, Taiwan. Engineering geology, 71(1-2), 49-61.

Lisle, R. J., & Srivastava, D. C. (2004). Test of the frictional reactivation theory for faults and validity of fault-slip analysis. Geology, 32(7), 569-572.

Liu, T. K. (1982). Tectonic implication of fission track ages from the Central Range, Taiwan: Proceeding of the Geological Society of China, 25, 23-37.

Liu, T. K., Hsieh, S., Chen, Y. G., & Chen, W. S. (2001). Thermo-kinematic evolution of the Taiwan oblique-collision mountain belt as revealed by zircon fission track dating. Earth and Planetary Science Letters, 186(1), 45-56.

Malavieille, J., Dominguez, S., Lu, C. Y., Chen, C. T., & Konstantinovskaya, E. (2019). Deformation partitioning in mountain belts: insights from analogue modelling experiments and the Taiwan collisional orogen. Geological Magazine, 1-20.

Masoud, A. A., & Koike, K. (2011a). Auto-detection and integration of tectonically significant lineaments from SRTM DEM and remotely-sensed geophysical data. ISPRS Journal of Photogrammetry and Remote Sensing, 66(6), 818-832.

Masoud, A. A., & Koike, K. (2011b). Morphotectonics inferred from the analysis of topographic lineaments auto-detected from DEMs: Application and validation for the Sinai Peninsula, Egypt. Tectonophysics, 510(3-4), 291-308.

Morelli, M., & Piana, F. (2006). Comparison between remote sensed lineaments and geological structures in intensively cultivated hills (Monferrato and Langhe domains, NW Italy). International Journal of Remote Sensing, 27(20), 4471-4493.

Morris, A., Ferrill, D. A., & Henderson, D. B. (1996). Slip-tendency analysis and fault reactivation. Geology, 24(3), 275-278.

Morris, A., & Ferrill, D. A. (2009). The importance of the effective intermediate principal stress (σ2) to fault slip patterns. Journal of Structural Geology, 31(9), 950-959.

Nakamura, M. (2004). Crustal deformation in the central and southern Ryukyu Arc estimated from GPS data. Earth and Planetary Science Letters, 217(3-4), 389-398.

Nishimura, S., Hashimoto, M., & Ando, M. (2004). A rigid block rotation model for the GPS derived velocity field along the Ryukyu arc. Physics of the Earth and Planetary Interiors, 142(3-4), 185-203.

Peacock, D. C. P., Nixon, C. W., Rotevatn, A., Sanderson, D. J., & Zuluaga, L. F. (2016). Glossary of fault and other fracture networks. Journal of Structural Geology, 92, 12-29.

Pollard, D. D., & Aydin, A. (1988). Progress in understanding jointing over the past century. Geological Society of America Bulletin, 100

Rateb, A., Ching, K. E., Kuo, C. Y., Rau, R. J., & Chen, C. L. (2017). Kinematics of the tectonic blocks and active faults at the post-orogenic stage: Northern Taiwan. Journal of Asian Earth Sciences, 149, 29-40.

Sauber, J. M., & Molnia, B. F. (2004). Glacier ice mass fluctuations and fault instability in tectonically active Southern Alaska. Global and Planetary Change, 42(1-4), 279-293.

Scholz, C. H. (2002). The mechanics of Earthquakes and faulting, Cambridge University Press.

Schultz, R. A., & Fossen, H. (2008). Terminology for structural discontinuities. AAPG bulletin, 92(7), 853-867.

Shyu, J. B. H., Sieh, K., Chen, Y. G., & Liu, C. S. (2005). Neotectonic architecture of Taiwan and its implications for future large earthquakes. Journal of Geophysical Research: Solid Earth, 110(B8).

Sibuet, J. C., Letouzey, J., Barbier, F., Charvet, J., Foucher, J. P., Hilde, T. W., Kimura, M., Chiao, L.V., Marsset, B., Muller, C., & Stéphan, J. F. (1987). Back arc extension in the Okinawa Trough. Journal of Geophysical Research: Solid Earth, 92(B13), 14041-14063.

Sibuet, J. C., & Hsu, S. K. (1997). Geodynamics of the Taiwan arc-arc collision. Tectonophysics, 274(1-3), 221-251.

Stanley, R. S., Hill, L. B., Chang, H. C., & Hu, H. N. (1981). A transect through the metamorphic core of the Central Mountains, southern Taiwan. Memoir of the Geological Society of China, 4, 443-473.

Suppe, J. (1981). Mechanics of mountain building and metamorphism in Taiwan. Memoir of the Geological Society of China, 4, 67-89.

Suppe, J. (1984). Kinematics of arc-continent collision, flipping of subduction and back-arc spreading near Taiwan. Memoir of the Geological Society of China, 6, 21-33.

Sutinen, R., Piekkari, M., & Middleton, M. (2009). Glacial geomorphology in Utsjoki, Finnish Lapland proposes Younger Dryas fault-instability. Global and Planetary Change, 69(1-2), 16-28.

Tarolli, P., & Fontana, G. (2009). Hillslope-to-valley transition morphology: New opportunities from high resolution DTMs. Geomorphology, 113(1-2), 47-56.

Teng, L. S. (1990). Geotectonic evolution of late Cenozoic arc-continent collision in Taiwan. Tectonophysics, 183(1-4), 57-76.

Teng, L. S. (1996). Extensional collapse of the northern Taiwan mountain belt. Geology, 24(10), 949-952.

Teng, L. S., Lee, C. T., Tsai, Y. B., & Hsiao, L. Y. (2000). Slab breakoff as a mechanism for flipping of subduction polarity in Taiwan. Geology, 28(2), 155-158.

Twidale, C. R., Bourne, J. A., Spooner, N. A., & Rhodes, E. J. (2007). The age of the palaeodunefield of the northern Murray Basin in South Australia: Preliminary results. Quaternary International, 166(1), 42-48.

Vavryčuk, V., Beer, M., Kougioumtzoglou, I., Patelli, E., & Au, I. K. (2015). Earthquake mechanisms and stress field. Encyclopedia of earthquake engineering, 728-746.

Vinogradova, A. I., & Eremin, V. K. (Eds.). (1971). Aerial methods for geological investigations Leningrad: Nedra (in Russian).

Wallace, R. E. (1951). Geometry of shearing stress and relation to faulting. The Journal of geology, 59(2), 118-130.

Wang, Y. U. A. N. (1966). Some geologic observations in the Coastal Range, eastern Taiwan. Proceeding of the Geological Society of China, 9, 86-93.

Wells, D. L., & Coppersmith, K. J. (1994). New empirical relationships among magnitude, rupture length, rupture width, rupture area, and surface displacement. Bulletin of the seismological Society of America, 84(4), 974-1002.

Wilson, J. T. (1941). Structural features in the Northwest Territories. American Journal of Science, 239(7), 493-502.

Wise, D.U., Grady, L.T., & Salvini, F. (1985). Topographic lineament domains of the Appalachians- Some new methods and techniques for paleostress analysis. In 1985 International Geoscience and Remote Sensing Symposium (IGARSS'85), Amherst, MA, 125-130.

Wladis, D. (1999). Automatic lineament detection using digital elevation models with second derivative filters. Photogrammetric engineering and remote sensing, 65, 453-458.

Wu, F. T. (1978). Recent tectonics of Taiwan. Journal of Physics of the Earth, 26 (Supplement), S265-S299.

Wu, F. T., Liang, W. T., Lee, J. C., Benz, H., & Villasenor, A. (2009). A model for the termination of the Ryukyu subduction zone against Taiwan: A junction of collision, subduction/separation, and subduction boundaries. Journal of Geophysical Research: Solid Earth, 114(B7).

Wu, W. N., Kao, H., Hsu, S. K., Lo, C. L., & Chen, H. W. (2010). Spatial variation of the crustal stress field along the Ryukyu-Taiwan-Luzon convergent boundary. Journal of Geophysical Research: Solid Earth, 115(B11).

Wu, Y. M., Chang, C. H., Zhao, L., Shyu, J. B. H., Chen, Y. G., Sieh, K., & Avouac, J. P. (2007). Seismic tomography of Taiwan: Improved constraints from a dense network of strong motion stations. Journal of Geophysical Research: Solid Earth, 112(B8).

Wu, Y.M., Zhao, L., Chang, C.H., & Hsu, Y.J. (2008). Focal-mechanism determination in Taiwan by genetic algorithm. Bulletin of the Seismological Society of America, 98(2), 651-661.

Yeh, C. H., Chen, Y.C., Chang, K.J., Lin, M.L., & Hsieh, Y.C. (2014). Derivation of strike and dip in sedimentary terrain using 3D image interpretation based on airborne LiDAR data. Terrestrial, Atmospheric and Oceanic Sciences, 25(6), 775.

Yen, T. P. (1954). The gneisses of Taiwan. Bulletin Geological Survey, 5, 1-100.

Yokoyama, R., Shirasawa, M., & Pike, R.J. (2002). Visualizing topography by openness: a new application of image processing to digital elevation models. Photogrammetric engineering and remote sensing, 68(3), 257-266.

Yu, S.B., Kuo, L.C., Punongbayan, R.S., & Ramos, E.G. (1999). GPS observation of crustal deformation in the Taiwan-Luzon region. Geophysical Research Letters, 26(7), 923-926.

Appendix A Surface fractures orientation of domain I

Plane No.		Strike		Dip		Long	Lat	R^2
1	N	8	W	59	E	331806	2716050	0.94
2	N	19	W	60	W	328088	2715050	0.42
3	N	40	E	55	W	331056	2720230	0.99
4	N	30	W	41	W	336673	2715542	0.99
5	N	74	W	57	W	335135	2716368	0.91
6	N	73	W	59	W	337166	2716136	0.98
7	N	80	E	44	E	329720	2718187	0.97
8	N	89	E	58	E	328906	2717243	0.96
9	N	84	E	51	E	328786	2716454	0.99
10	N	10	W	59	E	331274	2715394	0.89
11	N	86	E	42	E	332747	2717747	0.98
12	N	35	E	62	E	332366	271448	0.94
13	N	40	W	59	E	330180	2718700	0.97
14	N	31	E	30	W	335764	2715968	0.35
16	N	18	E	59	W	328620	2715488	0.98
17	N	75	E	49	E	328836	2715045	0.95
18	N	74	E	67	W	329862	2712516	0.87
19	N	16	E	51	W	329351	2712378	0.97
20	N	21	W	45	W	331508	2708631	1
21	N	87	E	40	E	329767	2714008	1
22	N	55	E	68	W	329604	2719862	0.9
23	N	12	E	52	E	333754	2719792	0.87
24	N	8	E	56	E	334911	2720104	0.9
25	N	52	E	58	E	332962	2719822	0.9
26	N	72	W	55	W	334958	2714637	0.97
27	N	2	W	48	W	332664	2721255	0.93
28	N	73	W	55	E	333168	2721143	0.97
29	N	74	E	42	E	330078	271971	0.57
30	N	9	W	67	W	330651	2721978	0.77

31	N	13	E	61	E	334554	2719913	0.97
32	N	1	E	50	E	334281	2719746	0.98
33	N	85	E	64	W	331488	2720229	0.51
34	N	72	E	66	W	330245	2720721	0.72
35	N	34	E	82	E	329155	2715189	0.5
36	N	89	E	41	E	330136	2713077	0.02
37	N	72	E	69	W	329097	2718817	0.91
38	N	1	E	51	W	331312	2719635	0.94
39	N	50	W	76	W	337225	2718249	0.63
40	N	40	E	54	W	332274	27201219	0.74
41	N	70	E	71	W	334145	2709009	0.86
42	N	77	W	65	E	331221	2711400	0.98
43	N	67	E	65	W	329830	2719446	0.94
44	N	16	W	73	E	330154	2718567	0.91
45	N	10	W	72	W	333205	2710149	0.95
46	N	26	E	58	W	330830	2709870	0.96
47	N	76	E	56	W	3320812	2718851	0.94
48	N	80	E	54	W	332940	2721276	0.67
49	N	87	E	81	W	333112	2720737	0.33
50	N	60	W	58	E	333229	27188073	0.92

Appendix B Surface fractures orientation of domain II

Plane No.		Strike		Dip		Long	Lat	R^2
1	N	52	E	67	W	326661	2693631	0.41
2	N	52	E	55	E	325024	2694552	0.58
3	N	89	E	69	E	324184	2694089	0.91
4	N	66	W	45	E	320913	2696725	0.04
5	N	16	W	54	W	325434	2697160	0.95
7	N	10	E	72	W	352538	2704665	0.47
8	N	27	E	62	W	324571	2704081	0.89
9	N	23	E	42	W	323276	2701834	0.99
10	N	12	E	50	W	317198	2696184	0.99
11	N	9	E	49	W	320272	2669906	0.99

12	N	18	E	56	W	325106	2708466	0.99
13	N	52	E	67	W	321089	2703752	0.65
14	N	34	E	47	W	322455	2704502	1
15	N	22	W	53	W	323423	2708399	0.96
16	N	78	W	8	W	324660	2706086	0.63
17	N	77	E	43	E	326917	2696426	0.93
18	N	75	W	31	E	329339	2699547	0.99
19	N	26	E	53	W	319776	2701025	0.91
20	N	66	W	59	W	319839	2695509	0.88
21	N	87	E	63	E	318224	2696478	0.82
22	N	37	W	26	W	318841	2698073	0.43
23	N	36	E	31	W	317753	2699975	0.97
24	N	35	W	48	W	318831	2696612	0.72
25	N	9	W	22	W	320425	2694730	0.5
26	N	62	E	57	E	319892	2694518	0.97
27	N	86	E	49	W	323241	2700618	0.94
28	N	6	W	24	E	323671	2706271	0.9
29	N	56	W	73	E	325732	2703467	0.68
30	N	85	E	54	W	327351	2702654	0.94
31	N	28	W	71	W	326585	2706842	0.53
32	N	25	W	82	E	326387	2709161	0.32
33	N	21	W	61	W	324094	2711039	0.98
34	N	13	E	51	W	323629	2707990	0.96
35	N	71	W	35	E	327703	2701160	0.86
36	N	81	W	51	E	320535	2702975	0.44
37	N	40	W	50	W	320636	2704732	0.99
38	N	42	W	44	W	321731	2706702	0.98
39	N	78	E	48	E	322405	2707820	0.99
40	N	53	E	49	W	317655	2700900	0.98
41	N	71	E	43	W	318988	2701190	1
42	N	73	e	37	e	323428	2707533	0.92
43	N	61	e	52	w	319199	2698476	0.98
44	N	42	E	43	W	322748	2695964	0.98
45	N	24	E	24	W	322094	2700274	0.78
46	N	70	E	66	W	323296	2698281	0.7
47	N	10	E	55	W	324285	2697891	0.93
48	N	78	E	40	E	322640	2706660	1
49	N	13	E	65	W	320996	2698510	0.93
50	N	3	E	54	W	319942	2694792	0.99
51	N	9	W	69	W	319340	2699477	0.39
52	N	13	W	76	W	319560	2700021	0.83
53	N	80	E	45	W	322667	2694701	0.99
54	N	21	E	50	W	321285	2698136	0.98

55	N	57	W	57	E	326751	2695032	0.95
56	N	73	W	50	E	325557	2699198	0.93
57	N	64	E	30	W	326859	2698169	0.97
58	N	14	E	50	W	322066	2708730	0.93
59	N	54	W	43	E	329735	2702449	0.92
60	N	2	W	43	E	326579	2705307	0.9
61	N	74	W	54	E	325316	2699673	0.83
62	N	77	W	39	E	327368	2701749	0.94
63	N	73	W	63	E	325263	2706089	0.95
64	N	11	E	54	W	325032	2706034	0.98
65	N	21	W	59	W	327969	2701224	0.88

Appendix C Surface fractures orientation of domain III

Plane No.		Strike		Dip		Long	Lat	R^2
1	N	77	W	79	E	310226	2673179	0.78
2	N	40	W	34	W	311666	2672977	0.13
3	N	71	W	63	E	310512	2673670	0.33
4	N	1	W	19	E	313955	2678225	0.03
5	N	15	E	20	E	313450	2678665	0.36
6	N	6	E	48	E	310722	2684101	0.73
7	N	26	E	68	E	312087	2676986	0.97
8	N	71	E	70	E	311838	2678026	0.99
9	N	79	E	49	W	314034	2684235	0.99
10	N	86	W	22	E	304253	2673838	0.3
11	N	37	E	34	W	303973	2676813	0.98
12	N	3	E	43	W	304270	2677595	0.96
13	N	4	W	66	W	310255	2679302	0.78
14	N	37	W	64	E	305167	2674627	0.44
15	N	13	E	56	W	304992	2675417	0.96
16	N	37	W	39	E	313836	2674367	0.12
17	N	63	E	76	E	317803	2680985	0.92
18	N	46	W	75	E	318123	2680829	0.99
19	N	51	E	64	E	313766	2681403	0.99
20	N	45	W	59	W	309952	2568924	0.5
21	N	64	E	50	E	313947	2674955	0.17
22	N	62	E	46	E	307463	2685194	0.76
23	N	37	W	49	E	307535	2683719	0.69
24	N	7	E	58	E	308870	2682568	0.29
25	N	86	W	68	W	314462	2677612	0.73

26	N	79	W	66	W	305041	2678551	0.73
27	N	81	W	34	W	304939	2679404	0.93
28	N	62	W	52	W	310511	2674534	0.84
29	N	84	E	43	W	313892	2681873	0.87
30	N	72	E	40	W	316518	2682444	0.99
31	N	66	E	58	W	309588	2688319	0.91
32	N	3	W	45	W	321353	2687961	0.05
33	N	44	E	19	W	310407	2689324	0.73
34	N	26	E	47	W	301918	2689529	0.86
35	N	17	W	68	W	317863	2688349	0.83
36	N	45	E	48	W	304031	2675589	0.99
37	N	67	E	55	W	314256	2691843	0.99
38	N	22	E	52	W	311701	2690406	0.93
39	N	72	E	44	W	314102	2692876	0.76
40	N	56	E	67	W	309050	2681478	0.95
41	N	23	W	66	W	311753	2686813	0.78
42	N	14	E	74	E	317966	2683027	0.5
43	N	15	W	81	E	318208	2683197	0.83
44	N	3	W	77	E	313073	2681498	0.92
45	N	53	W	59	E	313943	2691852	0.88
46	N	63	E	68	E	319239	2686751	0.97
47	N	47	W	76	W	307809	2676895	0.98
48	N	25	E	57	W	315008	2695917	0.92
49	N	66	W	68	W	307441	2683632	0.62
50	N	40	E	31	W	308195	2680204	0.52
51	N	76	E	66	E	316664	2679762	0.97
52	N	64	W	49	W	315941	2679548	0.93
53	N	38	E	71	E	315943	2673060	0.51
54	N	34	E	67	E	324046	2684227	0.97
55	N	23	W	72	E	320718	2687988	0.89
56	N	22	E	74	E	319322	2868907	0.55
57	N	82	W	50	E	321329	2689460	0.93
58	N	49	W	57	E	314506	2685974	0.98
59	N	31	W	52	W	306777	2675943	0.63
60	N	10	W	64	E	304374	2679758	0.85
61	N	47	W	80	E	310098	2684663	0.92
62	N	1	E	40	W	322381	2687782	0.98
63	N	86	W	73	W	315979	2679126	0.68
64	N	55	E	58	W	315798	2677536	0.99
65	N	31	W	61	W	305224	2679885	0.84
66	N	25	E	70	W	322788	2687524	0.92
67	N	69	E	52	W	315506	2688298	0.99
68	N	80	E	74	W	314947	2674865	0.91

69	N	23	E	54	W	309318	2688305	0.98
70	N	47	E	54	W	308289	2683437	0.87
71	N	22	E	43	W	312253	2684120	0.82
72	N	27	E	68	E	307758	2680591	0.84

Appendix D Related parameters of surface fractures at domain I

Plane No.	Traces (m)	Distances (m)	Area (m^2)	Points	Relief (m)
1	5705	5549.17	1898553.0	26	762.37
2	4325	4251.44	994568.9	20	745.64
3	5793	5664.13	979038.9	35	800.42
4	4263	3856.97	1584079.4	26	677.45
5	4406	4268.50	937481.5	26	377.44
6	2917	2776.77	953743.5	24	578.83
7	3326	2843.80	762093.0	24	700.30
8	2827	2696.90	682691.0	32	593.13
9	2489	2182.26	692159.3	25	501.04
10	4486	4115.61	836518.7	33	727.12
11	2492	2299.36	515201.4	20	511.65
12	4953	4538.30	1277854.2	26	664.81
13	4109	3931.21	235290.9	27	603.17
14	3727	3312.73	16982.0	25	433.46
16	3280	3071.75	250048.7	24	587.15
17	6050	5144.88	2551331.7	41	1120.96
18	3742	3476.85	1461948.7	25	877.61
19	4474	4022.37	1407889.5	29	1005.88
20	3014	2712.12	493325.4	19	866.80
21	2380	2606.75	568191.3	13	1818.00
22	3717	3669.27	257628.3	29	478.91
23	2975	2767.42	64681.9	23	286.58
24	2006	1948.93	160728.4	17	187.81
25	2634	2619.37	353743.1	22	388.39
26	5229	4841.99	511253.7	22	705.91
27	2262	2142.52	2064.0	23	290.35
28	2113	1961.37	378838.9	20	317.16
29	2175	2157.15	224212.4	17	422.90
30	1522	1495.26	154035.7	17	263.57

31	1556	1518.00	167391.5	19	246.69
32	1362	1292.52	157106.4	11	231.11
33	2455	2440.35	166885.4	21	168.36
34	2079	2054.14	63051.7	21	254.41
35	2754	2742.74	700141.5	17	725.91
36	2888	2809.17	662665.2	18	675.22
37	2311	2218.95	243856.3	18	488.73
38	2600	2505.41	29523.5	24	231.49
39	2451	2437.14	204305.9	17	201.54
40	3202	3078.14	216121.4	26	201.51
41	1542	1517.25	216905.7	11	374.64
42	3444	3394.53	498930.5	18	984.95
43	2007	2001.97	12506.1	18	447.61
44	2707	2679.66	227488.7	15	421.95
45	3065	3013.37	715690.6	16	672.86
46	4161	3994.70	1310778.7	14	850.43
47	2748	2591.20	144904.6	26	340.22
48	2346	2246.00	44927.5	15	273.68
49	1896	1889.95	267210.5	16	386.45
50	4928	4639.53	1515131.4	24	634.91

Appendix E Related parameters of surface fractures at domain II

Plane No.	Trace (m)	RLD (m)	Area (m^2)	Points	Relief (m)
1	7026	6963.43	3015407.07	30	977.4
2	7628	7561.43	1664247.45	28	1121.1
3	5207	5050.33	3383301.26	25	1339.6
4	6838	6772.53	1711510.49	37	1089.7
5	5572	5386.62	1256770.53	30	724.7
7	4832	4799.74	1338316.01	30	695.3
8	4804	4683.86	949877.26	26	606.1
9	3875	3446.61	875122.75	36	782.5
10	5173	4658.48	476093.82	35	1256.6
11	7073	6559.25	4340874.30	18	1266.7
12	3294	3109.65	1437071.14	16	780.4

13	3581	3554.79	230076.65	28	511.9
14	4087	3795.41	650501.62	17	813.5
15	4149	4111.76	684294.80	25	881.9
16	4198	4184.02	280210.99	29	855.5
17	5500	5422.76	2087636.36	22	1425.8
18	2100	1611.42	606144.14	16	540.0
19	5204	5230.60	723619.95	24	1454.0
20	5532	5288.73	1205036.57	35	950.6
21	4938	4761.83	854779.63	34	1035.1
22	7832	7298.42	193698.24	43	949.7
23	5672	4767.07	4206746.86	24	1043.6
24	7474	7089.05	685741.85	38	929.5
25	4169	3993.96	278597.32	37	628.6
26	3808	3840.18	28966.87	19	1258.7
27	5081	4648.26	896929.09	23	850.1
28	6062	5951.90	236973.34	36	1341.1
29	4100	4088.49	479556.93	27	770.6
30	2812	2615.66	71510.42	18	378.4
31	5770	5723.76	1508974.37	24	1172.0
32	3949	3910.15	2265471.67	18	995.7
33	1704	1681.37	201146.08	16	571.5
34	2694	2516.42	110887.65	27	619.5
35	5610	4935.88	2186797.08	25	603.1
36	3638	3561.69	184395.35	33	395.5
37	2192	2014.69	372294.00	23	567.9
38	2168	1802.30	573060.51	18	527.4
39	3087	2832.38	1016942.22	19	650.5
40	3086	2678.17	1496453.82	18	922.7
41	2978	2577.57	5449.92	18	962.5
42	4634	4037.58	1431880.39	19	727.5
43	2976	2826.66	592138.80	14	623.0
44	5594	4988.44	3612249.10	20	945.8
45	9830	9288.33	577241.39	40	1388.2
46	7275	7148.56	2001387.70	31	733.1
47	4676	4735.47	887484.10	23	857.0
48	3655	3367.84	890685.97	12	537.9
49	2436	2342.58	759962.84	18	676.9
50	2199	2000.82	438369.90	24	745.8
51	4936	4857.48	2619434.03	21	985.0
52	4754	4695.89	2080660.36	28	1162.3
53	2510	2285.84	885517.37	16	615.4
54	3078	2880.50	941711.74	17	612.1
55	4904	4604.87	614200.80	28	1194.9

56	8913	8015.37	3852001.36	45	1023.3
57	5740	5571.62	21882.29	28	1006.0
58	1747	1477.51	236698.86	21	310.9
59	2581	2166.37	341657.23	20	316.6
60	3134	2656.56	803705.94	22	700.2
61	4597	4276.11	1296203.46	24	563.3
62	3760	3226.57	458086.08	18	433.3
63	2150	2073.46	274379.54	26	506.9
64	1205	1153.25	174470.81	10	303.0
65	2831	2792.83	176844.65	12	272.7

Appendix F Related parameters of surface fractures at domain III

Plane No.	Traces (m)	RLD (m)	Area (m^2)	Points	Relief (m)
1	4349	4284.209172	1105059.18	29	919.13
2	2995	2948.340357	145026.6943	32	323.3437
3	4142	4079.276865	548306.905	30	532.3837
4	3986	3951.350793	362959.1167	29	376.32
5	5104	4825.524397	1473913.82	30	669.73
6	8001	7857.035531	3007574.958	22	784.23
7	3627	3200.372913	1418781.653	20	1258.293
8	3624	2488.380235	3708223.327	24	1959.46
9	4438	3707.206873	2746241.38	27	1410.37
10	4581	4430.099604	1130438.922	32	753.073
11	6061	5765.491319	535424.5352	25	1289.653
12	3754	3512.619845	1464641.082	24	1189.687

13	6934	6439.221255	3303106.34	42	1297.813
14	3813	3750.740959	745269.769	32	1048.03
15	3569	3156.609028	1052443.597	31	900.19
16	4163	4129.544006	802297.6651	36	1124.55
17	7695	7422.896113	5949429.657	48	1886.07
18	5032	5261.482111	1021158.769	23	2254.427
19	5612	5219.772613	1893244.458	32	1652.612
20	5673	5609.350726	2194282.803	24	1374.323
21	8093	7812.914319	4420.075352	36	1100.981
22	2399	2235.623211	351083.0363	23	520.59
23	3610	3455.095774	7029.710855	33	464.65
24	3689	3623.465753	496700.9178	25	619.62
25	4484	4213.591884	68437.87915	22	1183.467
26	3463	1082.123115	141175.3686	36	570.88
27	4601	4389.91149	1079600.618	33	980.25
28	3978	3900.401369	178186.9183	22	429.2197
29	3063	2632.017405	511474.2714	16	545.823
30	5085	4060.314818	2384743.956	22	1487.79
31	2851	2642.760796	273974.0819	19	448.03
32	3706	3692.091014	547159.0832	17	686.637
33	5405	5122.828372	1394106.862	31	1020.517
34	7541	7045.185034	412702.0921	42	1286.417
35	6712	6595.617622	1442523.36	31	1311.493
36	3577	2960.309191	1134847.215	20	968.617
37	4216	3810.974338	152516.5847	26	1001.987
38	5536	5227.515593	573307.0965	23	829.327
39	5414	3950.21952	237523.3157	33	647.353
40	2455	2383.443937	476220.0443	15	794.32
41	4751	4782.443642	2011686.959	19	1686.837
42	9119	8991.619481	3139505.589	31	1711.7
43	4895	4874.975732	2786025.625	24	1487.933
44	4367	4414.94312	1202657.117	22	1188.597

45	3583	3559.729531	193123.0107	22	672.027
46	4626	4544.017402	246434.1585	22	1047.023
47	4259	4374.951019	1216370.812	17	1706.519
48	6077	5303.307669	1352653.004	32	803.927
49	3267	3058.148479	1038605.544	29	694.84
50	3640	3130.35928	543385.0005	27	454.8
51	4167	3803.421706	1722137.514	25	900.403
52	4532	3817.040289	2912110.722	21	1474.223
53	3084	2953.540617	684291	16	557.957
54	3266	3056.739815	1184177.643	20	979.5267
55	3790	3723.241115	1315474.618	20	642.31
56	5293	5265.464212	2309736.385	21	1403.367
57	3683	3379.534871	226300.9121	29	380.84
58	4415	4015.064749	2247732.435	18	1672.703
59	3325	3422.411574	895454.6748	18	1610.99
60	2966	2904.485156	273392.8998	21	356.43
61	3159	3123.435448	993242.0273	24	717.88
62	7439	6542.912324	7628180.045	29	1156.59
63	4244	4038.823272	2505234.821	28	1247.727
64	2625	2412.341134	862288.4407	19	693.27
65	3083	2996.129034	92497.02947	23	315.02
66	4307	4181.336367	1764944.058	26	894.477
67	5161	4778.647086	3243031.227	25	1270.663
68	3559	3465.693963	1734188.645	16	1115.253
69	3022	2828.002462	811714.7465	20	569.193
70	3081	2838.275008	418059.6679	22	549.56
71	6441	5712.407686	1677897.422	35	1427.73
72	5045	4980.444383	1483227.091	25	1040.86

Traces:

Summary of questions/answers and suggestions

Prof. Chang, Kuo-Jen

1. How do you identify the foliation in the 5m DTM data?

Ans: In the 3D environment, the small parallel, planar, triangle facets are presented for foliation planes (Figure 6.1A).

2. How to define the foliation in your thesis (planar structure defined metamorphic rock)?

Ans: updated the text in Section 3.1.1, p.22.

3. How to trace foliation on 5m DTM? Is the resolution of DTM enough to identify the geological structure?

Ans: updated the text in Section 4.1.1, p.42.

Suggestion: change the foliation term to the planar structure.

Ans: We already discussed the definitions and characteristics of foliation in 3D environment of DEM data (text in Section 3.1.1, p.22 and Section 4.1.1, p.42). We supposed that those characteristics are presented the foliation planes in schist rock area. Beside that, to verify our methodology, we want to compare the foliation attitude from DEM-derivation with the foliation attitute in geological map (Central Geological Survey, 1995). Therefore, we still keep the foliation term in our study.

4. Are they fractures or faults?

Suggestion: faults, because the length of planes is a few kilometers.

Ans: Because, no further information of fault characteristics are recognizable in 3D enviroments of 5 meter DEM data. Therefore, our traces results in Fig 4.17 could be represented for faults or joins. And, we assumed that the fractures term in our study composed of faults (shearing-models fractures) and joins (extension-models fractures) (text in Section 3.1.2, p.22). The fracture definitions are resonable for our study hypothesis.

5. Are fractures generated by single or multi of earthquake events?

Ans: In our research, we assumed that the fractures are only generated by single earthquake events.

Prof. Wang, Tai-Tien

1. Did you compare your fracture results with the other research?

Ans: Yes, we did compare fracture results with Liu et al. (1982) results in figure 2.4, p.17, section 2.2.

2. Did you compare your foliation system with the other research?

Ans: We did compare the results of the foliation attitude with the public database from the Geological map (Central Geological Survey, 1995).

Suggestion*:* Compare with the public reported, because of the fracture plane located in the lithology boundary of different rock types.

3. What is the component of the fracture plane on the map view?

Ans: In the map view (Fig 4.7), we displayed the fracture traces.

4. How can you make sure that trace is right?

Ans: To verify the accuracy of fracture planes, we guaranteed three main factors:

- Fracture traces were mapped along the lineaments.
- To distinguish the fractures and foliation, we used the cross-cutting relationship.
- Traces are cut across the ridges or rivers, and traces are confirmed as a certain plane in a certain view direction.

5. What do we have with the fracture locate in the same rock type?

Ans: We suppose that it could be fracture or shear zones.

6. Why do you want to correlate the earthquake events in the 10km depth with the surface fractures?

Ans: Due to the exhumation (updated the text in Section 4.2.2, p.68) and tectonic setting (Section 2.1, p.9) of the NE Taiwan region, our assumptions supposed that the events of the earthquake can manipulate fractures at 10 km in maximum and these fractures can be identified on the landscape at present.

7. Why we have the average values of friction angle and cohesion from rock mechanics?

Ans: From the geological map, we calculated the area of 3 representative rocks of NE Taiwan in Arc Map software, and we obtain the area ratio. We also summarized the average values of rock mechanics data for three rocks. Then we have calculated the average rock mechanics with the weighting of area ratio. Finally, we had the average cohesion and friction angle (updated the text in Section 3.2.5.3, p.39 and the table 3.1)

8. What are the unknown parameters to calculate fault instability?

Ans: The stress inversion result only presents the principal stress axes and relative size od principal stress values in Mohr’s circle diagram. Therefore the values of principal stresses are unknown.

9. How can you estimate the normal and shear traction of the fracture plane?

Ans: From focal mechanism data, we measured the Mohr’s circle by calculated the principal stress orientation and relative distance (stress ratio). We also calculated the Mohr-Coulomb failure criterion from the rock mechanism (cohesion, friction angle). We solve the equation of the tangent Mohr’s circle-failure criterion system to get the normal and shear traction (updated text in Section 3.2.5.3, p.39)

10. At 10 km, are frictional angles possible from brittle to ductile material?

Ans: No, they are only possible in the brittle material. Because the earthquake events are brittle deformation.

11. How can you determine the faulting types such as NF, SS, RF in the Mohr's circle?

Ans: From the focal mechanism data, we are able to categorize the seismic fault types by the rake angle. We used the program from Vavryčuk et al. (2015) to calculated the fault instability and displayed the different faulting types in the Mohr's circle.

12. In conclusion, the nucleated fractures can correlate with the evolution of the stress regime along the NE Taiwan coastline. What is the possibility of nucleated fracture?

Ans: The nucleated fractures pattern can correlated with the evolution of stress state from reverse faulting in the south via strike-slip faulting in the central to normal faulting in the north of the NE Taiwan region.

13. What is the meaning of 69.2% of reactivated fracture due to the opening of Okinawa Trough?

Ans: According that the kinematics of Okinawa Trough opening at NE Taiwan become dominant driving force, and we supposed that this tectonic motion could promote the reactivation of nucleated fracture. The results of 69.2% of nucleated fractures are reactivated in NE Taiwan verified and confirmed the crucial roles of this tectonic motion.

Suggestion: The fracture length too long. Reduce the length of fracture in the map view.

Ans: We did use the red dash lines to present the fractures traces (updated the figures 4.7 in Section 4.1.2.2, p.57)

Prof. Yeh, En-Chao

1. How you categorized the foliation and fracture plane in DTM data? Can you input more figures?

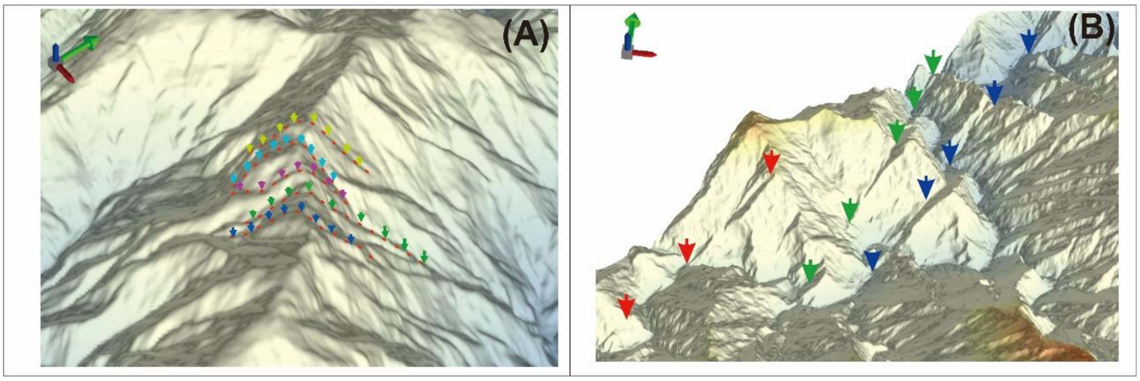

Figure 6.1: Characteristics of foliation and fracture in the 3D environment. A. Foliation; B. Fractures.

Ans: Foliations are characterized by the small, parallel, planar & triangle facets (Fig 6.1A). Each foliation plane as illustrated by different arrows color, and they are usually cut-across in the ridge. About fractures, they are identified on a large scale (Fig 6.1B). In general, the fracture planes usually cut-across the ridge, and the valley, and also we can found the cutting relationship between two different fracture systems.

2. Why is one fracture parallel with the lithology boundary? What is the meaning of those fractures?

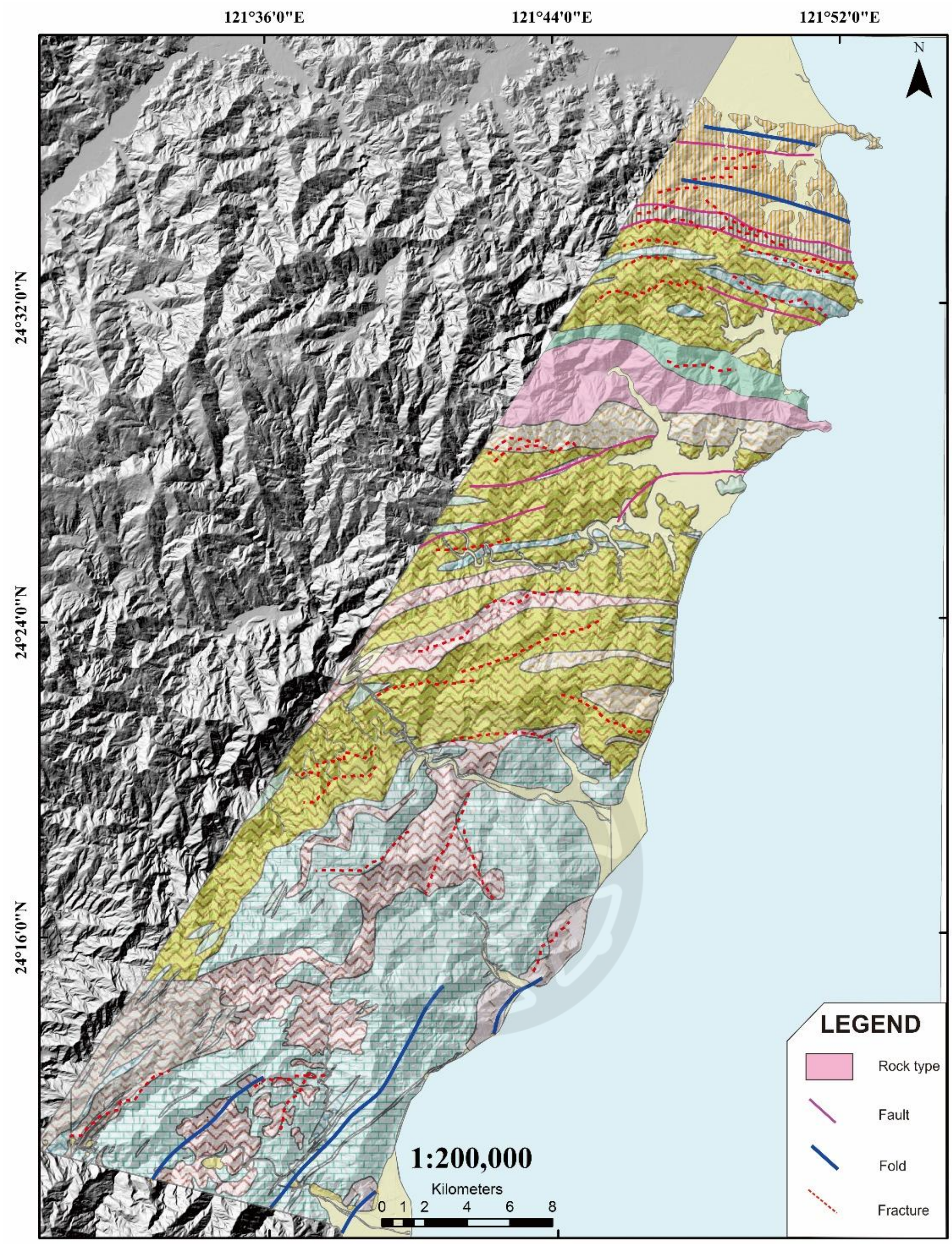

Figure 6.2: One surface fracture are parallel with the lithology boundary in the study area.

The fracture planes parallel with the lithology boundary are presented by red dash lines in Fig 6.2. In comparison, these surface fractures also parallel with the pre-existing fault and fold (purple and orange lines) from a geological map (Central Geological Survey, 1995). It means the striking of fracture evolves from N-S orientation in the south via NE-SW orientation in the central part to ENE-WSW orientation in the north. We are supposed that these fractures are related to the fault zones or shear zones. For detailed information, future investigations of fieldwork is needed to implement.

3. What is the difference between fracture sequences and earthquake sequences?

Ans: The cross-cutting relationship between individual fractures in location 4 was presented in Figure 4.6. In this figure, the fracture with the W-E strike cut three N-S striking fractures. Before fault instability evaluation, two of three N-S striking fractures are removed because the R^2 is quite low. After fault instability calculation, the W-E striking fractures became unstable under the II-C stress regime while the N-S striking fractures are stable (Fig 4.22C). It means the W-E striking fracture-related with earthquake events in domain I cut across the N-S striking fractures derived from the reversed faulting regime in domain III. Therefore, the fracture sequences are different from the earthquake sequences.

Suggestion**:** Please write down the details of DEM mapping and instability analysis for SOP learning.

Ans: Updated the text in Section 4.1, p.42-55, and Section 4.3, p.73-77. However, the thesis is not SOP yet.